Patient-Specific Finite Element Modeling of the Mitral Valve

by

Christopher David Andison

A thesis submitted to the

Faculty of Graduate and Postdoctoral Studies

in partial fulfillment of the requirements for the degree of

Master of Applied Science in Mechanical Engineering

Ottawa-Carleton Institute for Mechanical and Aerospace Engineering

University of Ottawa

Ottawa, Canada

August, 2015

Abstract

As the most commonly diseased heart valve, the mitral valve (MV) has been the subject of extensive research for many years. Unfortunately, the only treatment options currently available are surgical repair and replacement. Although repair is almost always preferable to replacement, it is often underperformed due to the complexity of MV repair surgeries. Consequently, there is significant interest in generating patient-specific finite element models of the MV for the purpose of simulating mitral repairs. For practical purposes transesophageal echocardiographic (TEE) images are most commonly used to reconstruct the mitral apparatus. However, limitations in ultrasound technology have prevented the detection of leaflet thicknesses. In the current study, a method was developed to accurately model variations in leaflet thicknesses using TEE datasets. Nine healthy datasets were modeled and the leaflet thicknesses were found to closely match previously reported results. As anticipated, normal valve function was also observed over the entire cardiac cycle.

Acknowledgements

I would like to express my sincere gratitude to my supervisor, Dr. Michel Labrosse, for his guidance, expertise, and the enthusiasm with which he shared his knowledge. I would also like to thank Dr. Vincent Chan and Dr. Benjamin Sohmer at the University of Ottawa Heart institute for their collaboration in obtaining the ultrasound datasets that were essential to this research.

I am forever grateful to my parents, David and Andrea Andison, for their unwavering support and encouragement. Finally, I would also like to thank my friends and colleagues who helped to keep me (relatively) sane throughout the process.

Table of Contents

List of Figures

List of Tables

Abbreviations

3D – Three-dimensional

4D – Four-dimensional (3D plus time)

Echo - Echocardiography

CMR – Cardiovascular magnetic resonance imaging

CT – Computed tomography

TEE – Transesophageal echocardiography

TTE – Transthoracic echocardiography

SNR – Signal-to-noise ratio

PTFE – Polytetrafluoroethylene

AL-MVP – Anterior leaflet prolapse

PL-MVP – Posterior leaflet prolapse

FEA – Finite element analysis

FEM – Finite element method

FE – Finite element

HOCM – Hypertrophic obstructive cardiomyopathy

FSI – Fluid-structure interaction

MVQ – Mitral valve quantification

MVSim – Mitral valve simulation

Chapter 1

1. Introduction

According to the World Health Organization, cardiovascular disease is the leading cause of death globally, accounting for 31 % of all global deaths in 2012 [1]. Since the majority of these deaths are the result of coronary heart disease and strokes, most of these deaths can be prevented by implementing population-wide strategies that aim to educate on behavioural risk factors such as alcohol use, poor diet, and physical inactivity. In the mid-twentieth century, developed countries began implementing educational strategies which, along with improved early detection and treatments, have resulted in a significant decline in cardiovascular disease related deaths in these countries over the past several decades.

Despite the steady decline in cardiovascular diseases in developed countries over the past 50 years, health care demands are only expected to increase in the future, powered by a rapidly aging population and an increased life expectancy [2]. Consequently, the occurrence of age-linked diseases is also expected to increase significantly. Valvular heart disease is one example of a disease that is closely linked to age. Currently, the prevalence of valvular heart disease in the United States of America is 2.5 %, affecting 0.7 % of the population aged 18-44 years, and 13.3 % of those over the age of 75 [3] for all heart valves combined. With adults aged 60 and over expected to represent approximately one third of the population in developed countries by 2050 [2], valvular heart disease has the potential to place a significant burden on the health care systems of developed countries in the near future. Further exacerbating the problem is the fact that current research into valvular diseases is limited, and treatments are expensive. Of the four main heart valves, the mitral valve may merit the most immediate attention since mitral disease is by far the most prevalent valvular disease, affecting over 9.3 % of the American population aged 75 years and older [4].

Currently, the only treatment options available for mitral diseases are surgical repair and replacement. Mitral valve repair is almost always preferable to valve replacement, since it is associated with better short-term and long-term survival, improved preservation of heart function, a reduced risk of complications, and does not require the long-term use of anticoagulants. However, due to the complexity of mitral valve repair, repair rates vary significantly between institutions and individual surgeons. In the United Kingdom, it has been proposed that institutions should perform a minimum of 50 mitral valve surgeries per year, with individual surgeons performing at least 25 repairs per year, to ensure that appropriate levels of expertise are developed and maintained [3]. Despite the fact that the advantages of mitral valve repair over replacement are well known, it would appear that many surgeons are not performing enough surgeries to develop the required level of expertise, and as a result mitral repairs are being underperformed. When analyzing over 28,000 isolated mitral valve operations between 2005 and 2007 (data gathered from the Society of Thoracic Surgeons), one study found that the median number of isolated mitral valve surgeries (per surgeon per year) and the mean rate of surgical repair were five and 41 %, respectively [5]. Furthermore, it was determined that the most significant predictive factor for increased surgical repair rates was increased surgeon mitral volume [5]. Consequently, mitral valve replacements are likely being over performed since the most experienced surgeons (≥ 60 mitral valve surgeries per year) opted to perform mitral repair procedures more than 70 % of the time [5].

Since mitral repair only gained widespread acceptance in the late 1980s, there is limited information on the long-term success rate of mitral repair. However, recent studies have found that long-term recurrence rates of mitral regurgitation are not satisfactory [6]–[9]. In order to improve success rates (by reducing the recurrence rate of moderate to severe mitral regurgitation), it has been suggested that surgery-induced tissue stresses must also be considered when determining the most appropriate repair technique(s) [10], [11]. Therefore, surgical techniques must restore normal valvular function, while also aiming to match normal stress ranges as closely as possible to ensure improved repair durability.

To minimize the burden of mitral disease on health care systems, mitral repair rates, especially among less experienced thoracic surgeons, must be improved. Since most surgeons are not able to perform enough mitral repair surgeries on an annual basis to develop the required level of expertise, a new tool is required to help identify mitral repair candidates, by providing the outcomes of what-if scenarios. For example, based on patient-specific defects in the mitral valve function, one is after information about the quality of the valve function after, say, an annuloplasty ring is implanted, or some type of leaflet resection is performed. Furthermore, this tool should have the ability to predict, and therefore minimize, surgery-induced tissue stresses to help maximize mitral repair durability. Such a tool could also prove very useful for the most experienced surgeons as it has the potential to help them to further improve their repair rates, while further minimizing reoperation rates.

However, before such a tool can be developed, a framework that is capable of generating accurate, patient-specific mitral valve models must first be developed. Therefore, it is necessary to create a program that is capable of accurately modeling the complex geometry of the mitral valve. Furthermore, this program must be able to accurately model the *in vivo* dynamics of the mitral valve. Validation of such a model will require the analysis of healthy datasets to ensure that the model can accurately model healthy mitral valve function. Once a method to accurately model the behaviour of healthy mitral valves has been developed, diseased valves can be analysed, and surgeries can be simulated to help predict and improve surgical outcomes.

1.1. Anatomy and Physiology of the Heart

In order to develop a proper understanding of the mitral valve, it is important to first develop a basic understanding of the anatomy and physiology of the (healthy) heart. The heart is a muscular organ that is composed of four chambers—the right and left atria, and the left and right ventricles (Figure 1.1). Tracing the path of blood flow through the heart (points 1-6 in Figure 1.1), deoxygenated blood returning from the body first enters the right atrium, before it flows through the tricuspid valve and into the right ventricle. When the right ventricle is full of blood, the ventricular walls begin to contract, causing the tricuspid valve to close and the pulmonary valve to open as blood is pumped towards the lungs. After passing through the lungs, oxygen-rich blood flows into the left atrium from the pulmonary veins, through the mitral valve, and into the left ventricle. Again, as the ventricular walls begin to contract, the mitral valve closes, and the oxygen-rich blood flows through the aortic valve to the rest of the body.

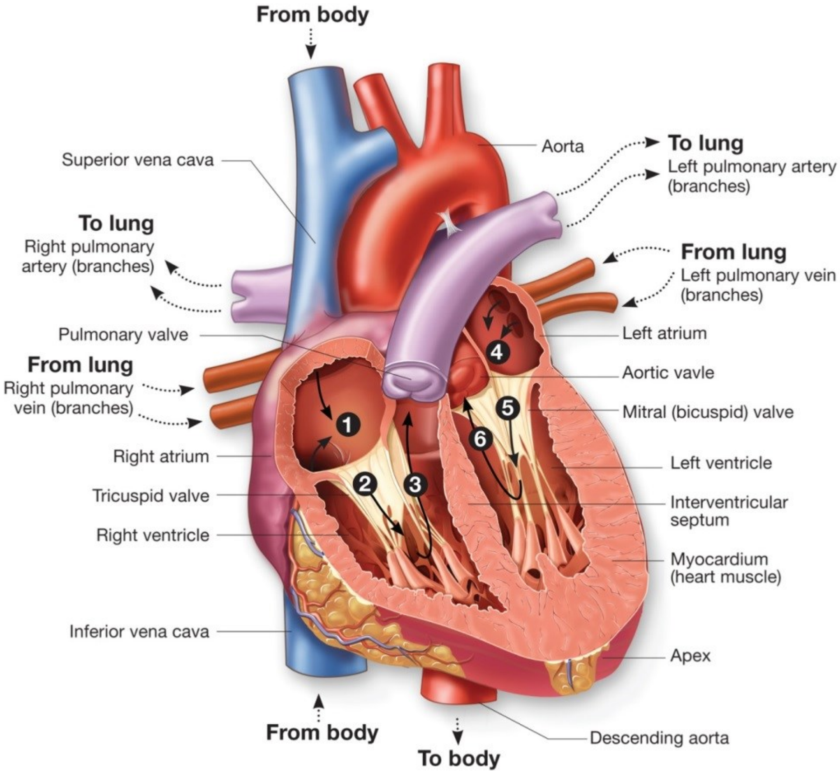

Figure 1.1: Blood flow through the heart [12].

When examining the flow of blood through the heart, it is often helpful to separate the cardiac cycle into two separate phases—diastole and systole. At the beginning of diastole, both the atrial and ventricular walls are relaxed, and initial filling is driven by a drop in ventricular pressures. As the ventricles approach their natural, relaxed volumes, the venous pressures begin to drive the rate of filling. Finally, as the ventricular pressure approaches the venous pressure, the atria contract to pump extra blood into the ventricles, thus ending the diastolic phase. Throughout diastole, the mitral and tricuspid valves remain open as blood flows from the atria into the ventricles (Figure 1.2).

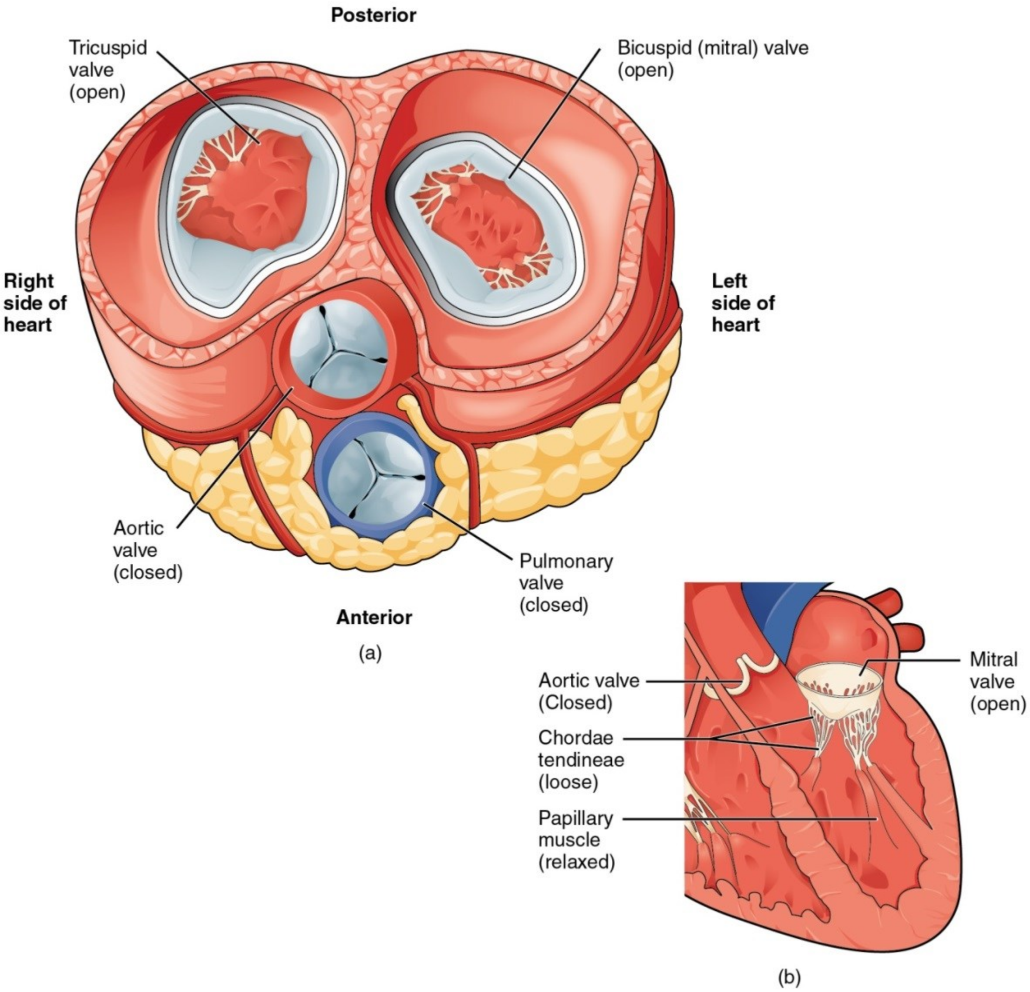

Figure 1.2: A transverse (a) and frontal (b) section through the heart showing the four heart valves during diastole [13].

The systolic phase begins with a brief period of isovolumetric contraction, resulting in a very sudden increase in ventricular pressure. The resulting pressure gradient across the mitral and tricuspid valves causes them to close, with minimal back-flow into the atria due to the formation of vortices around the valves. As the ventricles continue to contract, the aortic and pulmonary valves are forced open as the ventricular pressures surpass the arterial pressures, and blood is pumped out of the heart (Figure 1.3). Finally, once the ventricular contraction is complete, the ventricles begin to relax and expand resulting in the rapid decrease in ventricular pressure that marks the start of diastole.

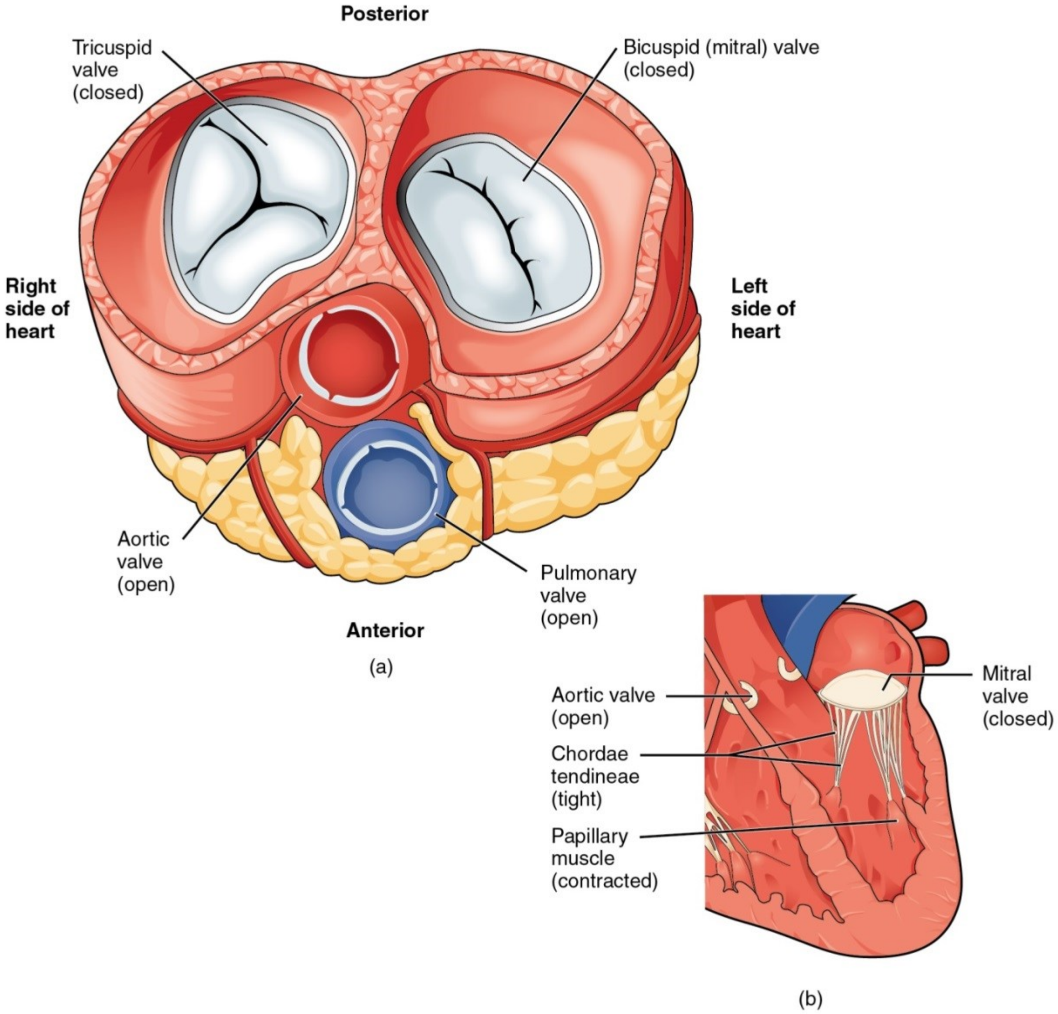

Figure 1.3: A transverse (a) and frontal (b) section through the heart showing the four heart valves during systole [13].

It is worthwhile noting that there is little, if any, active contribution from muscle cells to the closing or opening of any of the four heart valves. Instead, the valves' functions are dominantly the result of blood pressure differentials and adequate support, geometry and material properties, as detailed below for the mitral valve.

1.2. Anatomy and Physiology of the Mitral Valve

The mitral valve is composed of five main structures: the anterior and posterior leaflets, the annulus, the chordae tendineae, and the papillary muscles (Figure 1.4). Together, these structures form the functional unit of the mitral valve. When healthy, the mitral valve provides minimal resistance to the blood flow into the left ventricle during ventricular diastole, and prevents back-flow into the left atrium during ventricular systole.

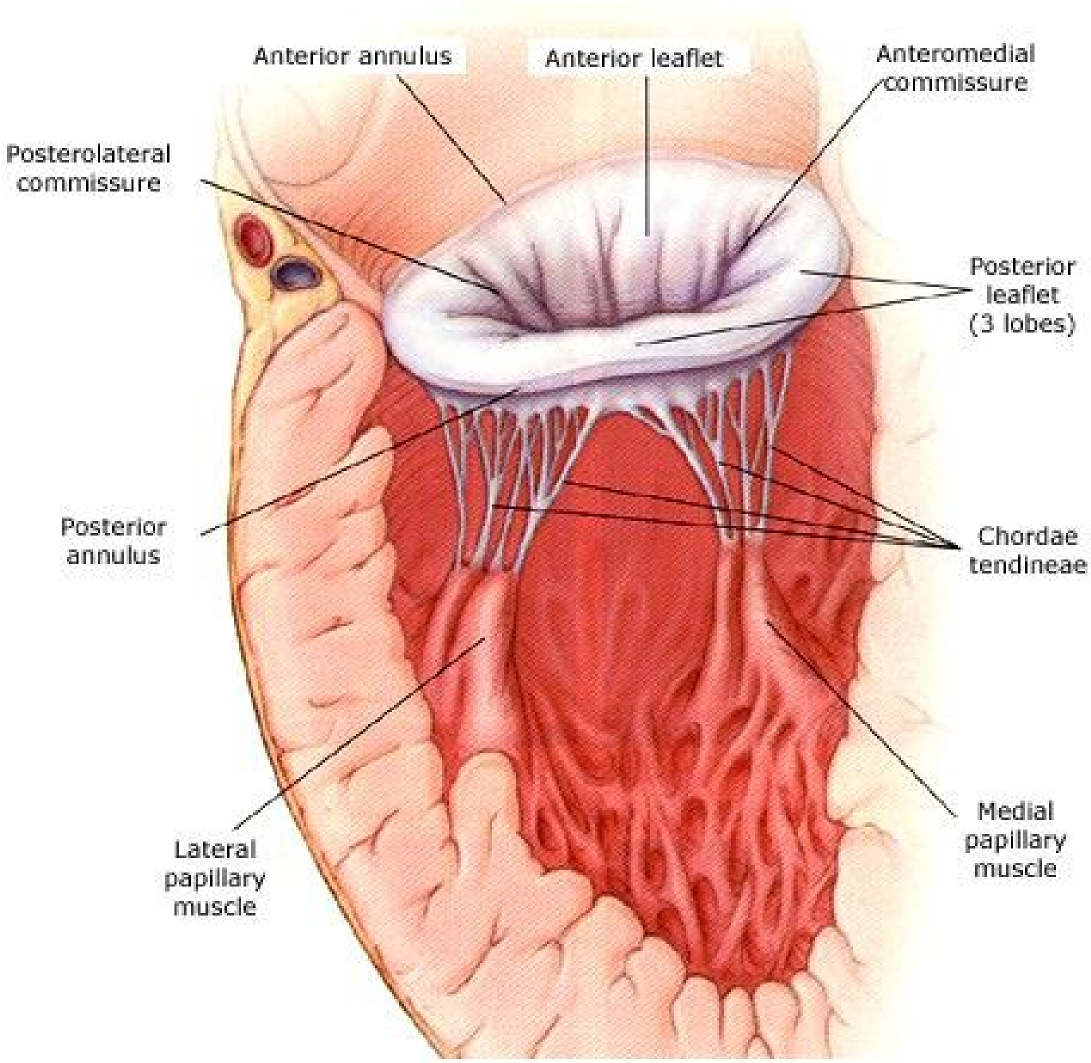

Figure 1.4: Substructures of the mitral valve [14].

1.2.1. The Mitral Annulus

The mitral leaflets are surrounded by a ring of fibrous tissue known as the mitral annulus. When viewed from above, the annulus appears to form a two-dimensional asymmetrical, elliptical ring that resembles a kidney bean, with an intervalley to interpeak span (or lateral to anteroposterior diameter) ratio of approximately 4:3 [15]. However, a three-dimensional (3D) view clearly shows the hyperbolic paraboloid (saddle) shape of the annulus, with anterior and posterior peaks, and medial and lateral valleys located at the commissures (Figure 1.5) [16]. Although the anterior portion of the annulus is consistently composed of dense, fibrous tissue, the composition of the posterior portion of the annulus varies significantly [15]. In some cases the posterior annulus is composed almost entirely of areolar tissue, and ventricular and atrial myocardium [15]. Consequently, annular dilation is much more prevalent along the posterior region of the annulus.

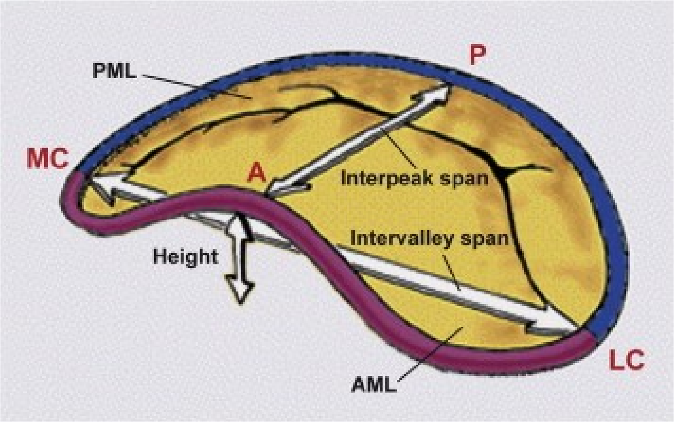

Figure 1.5: Three-dimensional schematic of the mitral annulus with the anterior and posterior annulus shown in red and blue, respectively. A, anterior; P, posterior; LC, lateral commissure; MC, medial commissure; AML, anterior mitral leaflet [16].

1.2.2. The Mitral Valve Leaflets

The mitral valve leaflets attach to the annulus and form a continuous curtain of tissue that closes to block the atrioventricular orifice during ventricular systole. Although anatomical differences have been noted [17], the mitral valve is generally defined as a bicuspid valve with an anterior and posterior leaflet. The anterior leaflet is typically larger than the posterior leaflet, but only occupies approximately one-third of the annular circumference, while the posterior leaflet is attached to the remaining two-thirds of the annular circumference. The two leaflets join at the anterolateral and posteromedial commissures, which are located below the left and right fibrous trigones, respectively [15]. Using Carpentier's method of classification, each leaflet is further divided by subcommissures into three scallops, with the subcomissures of the posterior leaflet being far more pronounced (Figure 1.6a). Another classification method has been proposed by Duran, which splits the mitral valve into lateral and medial sections based on the chordae tendineae origin points (Figure 1.6b). Using Duran's classification the anterior leaflet is divided into two sections (A1 and A2), and the posterior leaflet is divided into four sections (P1, PM1, PM2, and P2).

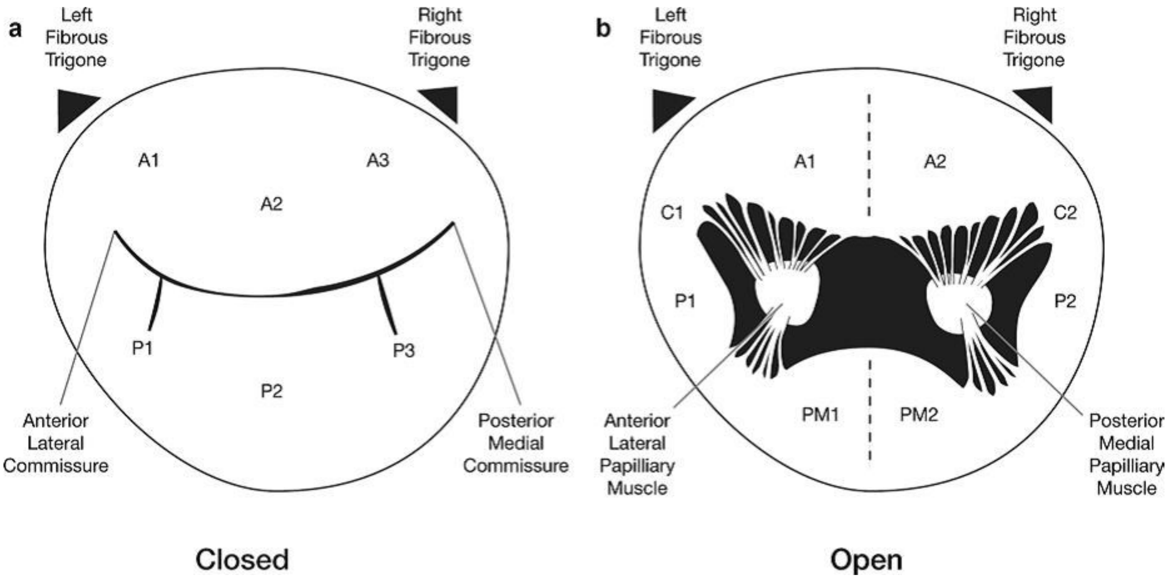

Figure 1.6: Classification of the mitral leaflet anatomy using (a) Carpentier's method and (b) Duran's method [15].

1.2.3. The Subvalvular Apparatus

Together, the chordae tendineae and papillary muscles form the subvalvular apparatus, which supports the leaflets during ventricular systole, thus preventing the regurgitation of blood into the left atrium. The chordae originate from the apex of the papillary muscles, with most chordae branching out before inserting into the valve leaflets. Based on their insertion locations, the chordae tendineae are classified as primary, secondary, or tertiary chordae. Primary chordae insert into the free edge of the mitral leaflets, while secondary (or strut) chordae insert into the body of the leaflets. Tertiary chordae, which originate from the ventricular muscle, are only present on the posterior leaflet and insert near the annulus, at the base of the leaflet [15].

There are two major papillary muscles—the anterolateral, and posteromedial papillary muscles—which support and stabilize the chordae tendineae during ventricular systole. The anterolateral papillary muscle is located superiorly on the anterior wall of the left ventricle, while the posteromedial papillary muscle is situated inferiorly on the posterior wall of the left ventricle [15]. Although the anterolateral papillary muscle is normally comprised of only one head, the posteromedial papillary muscle has two to three heads in 60% of hearts [15].

During diastole, the papillary muscles are relaxed and the chordae are slack as blood flows through the mitral valve, around the chordae, and into the left ventricle. However during ventricular systole, the papillary muscles begin to contract, and an increase in ventricular pressure pushes the mitral leaflets up toward the left atrium. This causes the chordae to stretch, and the leaflets and chordae form a parachute-like structure which prevents blood from flowing backwards into the left atrium (Figure 1.7).

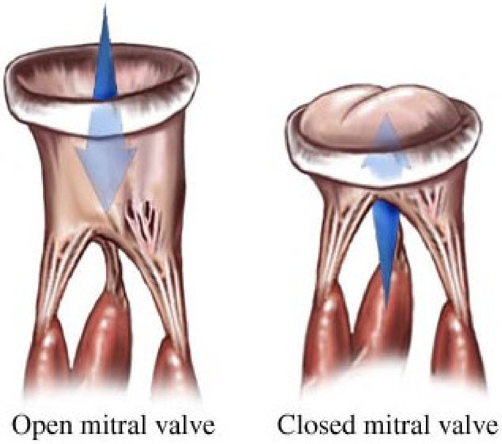

Figure 1.7: Healthy mitral valve during ventricular diastole (left) and ventricular systole (right) [18].

1.3. Pathology and Classification of Mitral Valve Disease

Although a variety of conditions can result in the impaired function of the mitral valve, any cardiac dysfunction that results from structural or functional abnormalities of the mitral valve can be classified as either mitral stenosis, or mitral regurgitation [15].

1.3.1. Mitral Stenosis

Any mitral disease that results in the narrowing or obstruction of the mitral valve orifice is defined as mitral stenosis (Figure 1.8). Although rare in developed countries, rheumatic fever remains the leading cause of mitral stenosis [15], [19]. Rheumatic fever, an inflammatory disease that can develop if strep throat or scarlet fever are not treated properly, can result in permanent damage to the heart and the heart valves [19]. Although far less common, congenital defects, calcium deposits on and around the valve, radiation treatments to the chest, and certain medications can also lead to mitral stenosis [19].

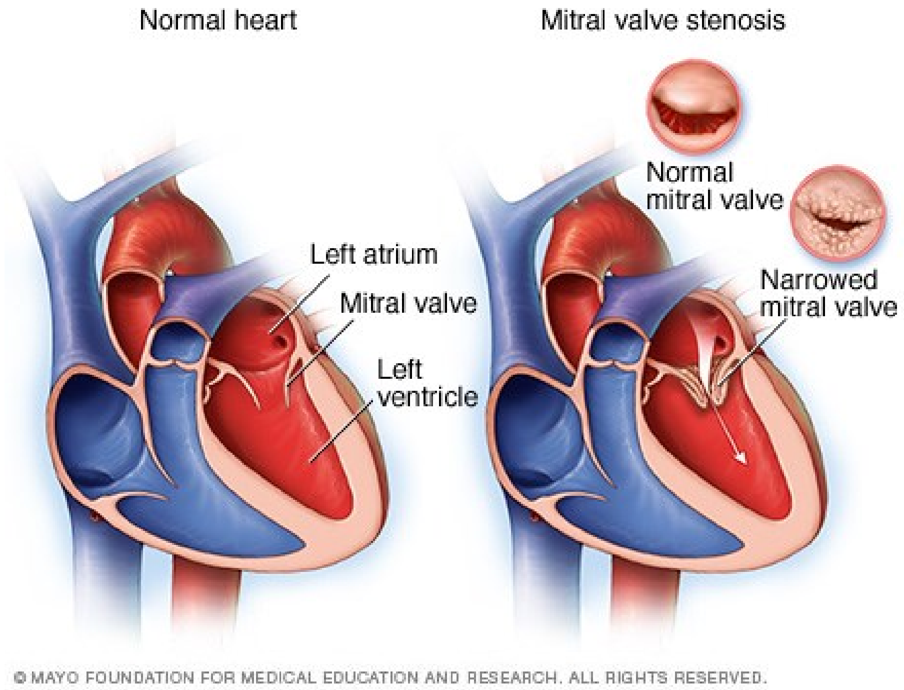

Figure 1.8: Healthy heart (left) and a diseased heart with mitral stenosis (right) [20].

Regardless of the cause, mitral stenosis can cause a variety of complications. A reduction in the mitral orifice area results in an increased resistance to blood flow into the left ventricle. Consequently, the atrial pressure increases which results in a pressure gradient between the left atrium and ventricle. An elevation in atrial pressure can result in left atrial hypertrophy or dilation (often both), as well as pulmonary edema due to the increase in pressure in the pulmonary vein and capillary bed [15]. Finally, chronic pulmonary hypertension leads to diseases of the right side of the heart including ventricular hypertrophy, right ventricular dilation, tricuspid insufficiency, and right side heart failure [15].

1.3.2. Mitral Regurgitation

To ensure complete closure of the mitral valve during ventricular systole, every component of the mitral valve must be free of any anatomic abnormalities or dysfunctions.

Mitral regurgitation, or mitral insufficiency, occurs when any abnormalities are present that result in the failure of the valve to close completely during ventricular systole, therefore allowing the back-flow of blood into the left atrium. A large variety of diseases and defects can result in mitral insufficiency, although the most common causes are coronary artery disease, dilated cardiomyopathy, mitral valve prolapse, and myxomatous degeneration (weakening of connective tissues) [15]. Since the motion of the mitral leaflets, and therefore the disease pathology, vary greatly depending on the underlying disease or defect, mitral regurgitation is subdivided into three main types based on Carpentier's classification method (Figure 1.9).

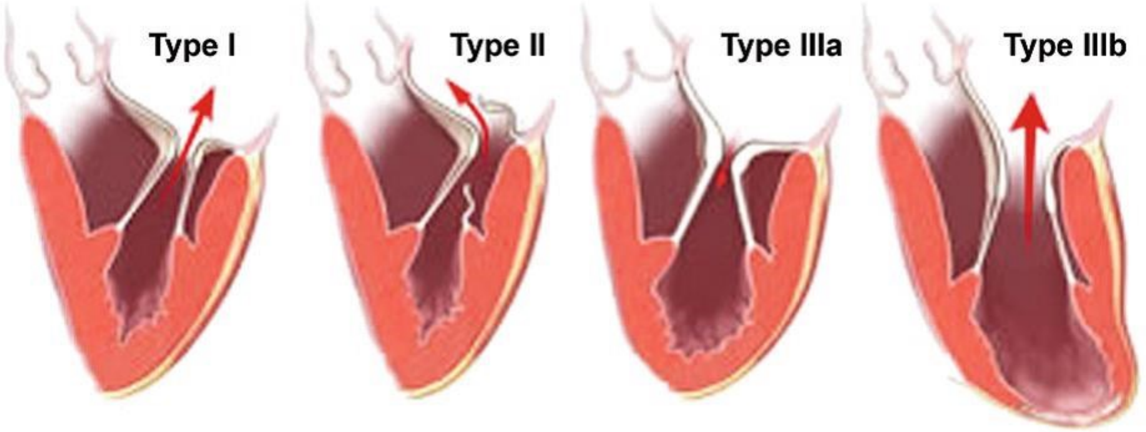

Figure 1.9: The Carpentier classification of mitral regurgitation [15].

Type I mitral regurgitation is characterized by normal leaflet motion and may be caused by annular dilation (secondary to left ventricular dilation), or leaflet perforations (secondary to endocarditis) [15]. Mitral regurgitation with excessive leaflet motion (Type II) is caused by the elongation or rupture of either the chordae or papillary muscles. Finally, Type III mitral regurgitation, which results from restricted leaflet motion, is subdivided into two subgroups. Type IIIa regurgitation exhibits leaflet restriction during diastole (often resulting from rheumatic disease), whereas Type IIIb exhibits leaflet restriction during systole, and is a common complication resulting from chronic coronary artery disease [15], [21].

Due to the incomplete coaptation of the mitral leaflets during ventricular systole an orifice is created, thus allowing the passage of blood from the left ventricle back into the left atrium during ventricular systole. This back-flow is responsible for volume overload in the left ventricle, which induces a variety of secondary morphological changes to both the left and right ventricles, as well as the left atrium [15]. Changes to the left ventricle include dilation and shape changes, increased left ventricular mass, and hypertrophy of the left ventricle resulting in dysfunction [15]. Finally, chronic mitral regurgitation also results in elevated pulmonary pressure. Therefore the morphological changes and pathologies associated with mitral stenosis are also common in patients suffering from chronic mitral regurgitation [15].

1.4. Mitral Imaging Techniques

Without accurate, easily reproducible imaging techniques that are capable of acquiring 3D plus time—or four-dimensional (4D)—images of the mitral valve, generating accurate, patient-specific models of the mitral valve would be impossible. Each 3D image provides the coordinates that are essential to building an accurate model of the valve, while the ability to observe the valve's behaviour over time is necessary when selecting an appropriate state to use to generate the model, and also for validating the accuracy of the model. Without the ability to observe the valve's behaviour over a full heartbeat, it would be impossible to determine the accuracy of the proposed computer model. Currently there are three commonly used imaging techniques that meet these requirements: 3D echocardiography (echo), cardiovascular magnetic resonance imaging (CMR), and cardiac computed tomography (cardiac CT).

Echocardiography, an imaging technique that uses high-frequency sound waves to produce images of the heart, is currently the primary method used to diagnose and monitor mitral disease. During echo, a transducer generates and directs the high-frequency sound waves towards the heart. These sound waves bounce off the structures in the heart and are detected by the ultrasound probe. A computer uses these reflected sound waves to generate either 2D or 3D images of the heart. Echocardiography is relatively inexpensive to use, and since it relies on sound waves to image biological tissues, it is safe for both children and adults. However, compared to CMR and cardiac CT, echo has a much lower resolution and signal-to-noise ratio (SNR). Consequently, ultrasound images cannot match the detail of these techniques. Echocardiography can be further divided into two subcategories based on the location of the ultrasound probe. Transthoracic echocardiography (TTE) uses an ultrasound probe that is placed on the chest, while transesophageal echocardiography (TEE) requires the probe to be guided down the patient's throat and into the esophagus. Since the esophagus is located directly behind the heart, TEE allows for more detailed images to be gathered since there is less tissue between the heart and probe, thus reducing signal attenuation.

Cardiac magnetic resonance imaging relies on a strong magnetic field and radio waves to alter the alignment of hydrogen atoms within the body. A computer is able to generate 2D images based on the activity of the hydrogen atoms, which are then combined to form a 3D image. Since CMR does not rely on ionizing radiation, there are no known biological risks associated with this imaging technique.

Cardiac CT uses x-rays to produce multiple images of the heart which are then stitched together to form a 3D model. Although CT scans often take less than 30 seconds [22], the patient is exposed to very large doses of ionizing radiation (100-1,100 times the radiation of a conventional x-ray) [22], [23]. Consequently, there are concerns that CT scans may significantly increase the risk of developing cancer.

Despite the superior image quality offered by CT and CMR, echo is still the most commonly used tool for the diagnosis and monitoring of diseased mitral valves. It is far less expensive than the other two imaging techniques, and does not have any associated health risks. However, while CT and CMR can image all of the mitral valve's components, the chordae tendineae cannot be detected using echo. Despite this limitation, echo—or more specifically TEE—was determined to be the most appropriate imaging technique to use for generating computer models of the mitral vale. Since TEE is commonly used in the diagnosis of mitral disease, and since it produces superior images of the mitral valve when compared to TTE, the computer program was designed using TEE images instead of TTE. Although echo images are more difficult to work with than CT or CMR images (due to the limited resolution and a lower SNR), most patients with a mitral disease will not receive a CT or CMR scan. Therefore a program that requires these types of imaging techniques to predict surgical outcomes would be of limited value.

1.5. Mitral Repair vs. Replacement

While the benefits of mitral repair have already been alluded to, more attention must be paid to both treatment options to fully understand why current trends are towards increased mitral repair rates. In general, when treatment of a diseased mitral valve is deemed necessary, there are three options: replacement with a mechanical prosthetic valve, replacement with a bioprosthetic valve, or surgical repair of the diseased valve.

1.5.1. Mechanical Valves

Mechanical heart valves are made entirely of biocompatible materials and do not contain any biological tissues. The most commonly used mechanical valves have a bileaflet design that consists of two carbon leaflets inside a ring that is covered with a polyester knit fabric (Figure 1.10) [24]. During surgery, the native mitral valve is usually removed (although in some instances it is simply displaced to make room for the replacement valve), and the mechanical valve is stitched to the native annulus.

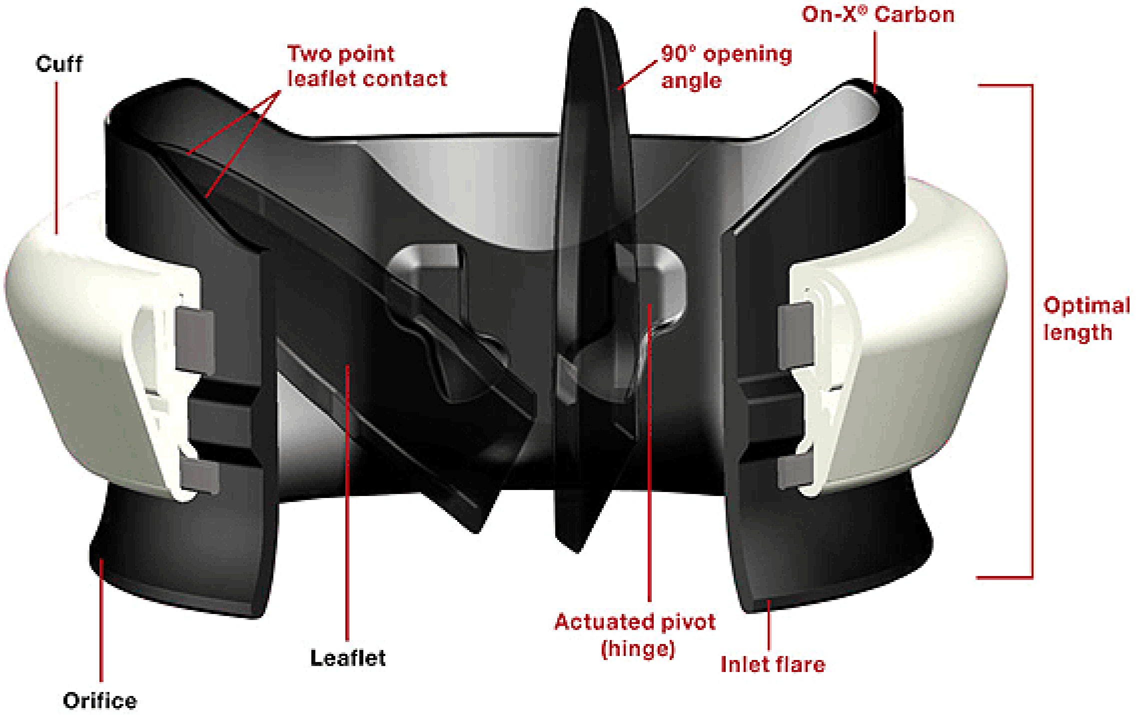

Figure 1.10: On-X Prosthetic Heart Valve and its components [25].

Since mechanical valves are made of materials such as carbon, titanium, polyester, and Teflon they are extremely durable and designed to last a lifetime [24], [26]. However, since these valves are not composed of biological tissues, patients require lifelong anti-coagulant treatment to prevent the formation of clots which can lead to a heart attack or stroke. Furthermore, these valves can be noisy, producing an audible "clicking" noise as they open and close.

1.5.2. Bioprosthetic Valves

Bioprosthetic valves are composed primarily of animal tissue, with an artificial frame (stent) that supports the biological tissue, and are sewn to the native annulus. Porcine stented valves are made from porcine aortic valves that are mounted on flexible stents, which are covered with polytetrafluoroethylene (PTFE) cloth to facilitate the ingrowth of tissue (Figure 1.11a) [24]. Pericardial bioprosthetic valves, on the other hand, are made from bovine pericardium that is mounted on a flexible silicone rubber frame, which is also covered in a PTFE cloth (Figure 1.11b) [24].

Figure 1.11: (a) Porcine bioprosthetic valve [27] and (b) PERIMOUNT mitral bioprosthesis [28].

Most patients with bioprosthetic mitral valves do not require life-long treatment with anticoagulants, and since these valves do not have any mechanical parts, they do not produce a “clicking” noise. However, these valves are not as durable as mechanical valves, with porcine valves usually lasting 10-15 years, while some bovine valves may last over 20 years [24], [26]. Consequently, younger patients may require reoperation to replace a bioprosthetic valve.

1.5.3. Surgical Outcomes—Mitral Repair vs. Replacement

Although it is not always feasible, mitral repair is now accepted as the best option for nearly all patients with a regurgitant mitral valve, and for many with a stenotic mitral valve [29]. A long list of benefits of mitral repair over replacement—including lower operative mortality [30]–[32], improved ventricular function [30], lower risk of stroke and infection [7], improved freedom from reoperation [9] and complications of anticoagulation therapy [29], and superior long term-survival [30], [33], [34]—is responsible for the growing popularity of mitral repair. Furthermore, reoperation rates after mitral repair (due to mitral prolapse) are slightly lower than reoperation rates after replacement (Figure 1.12) [9]. However, correction of anterior leaflet prolapse (although less common) is more challenging than correction of posterior leaflet prolapse [15]. Consequently, reoperation rates for mitral valve replacement are slightly lower than for repair when only anterior leaflet prolapse is considered (Figure 1.13). Repair techniques also appear to be improving, as can be seen by a significant decrease in reoperation rates between surgeries performed in the 1980s and 1990s (Figure 1.14).

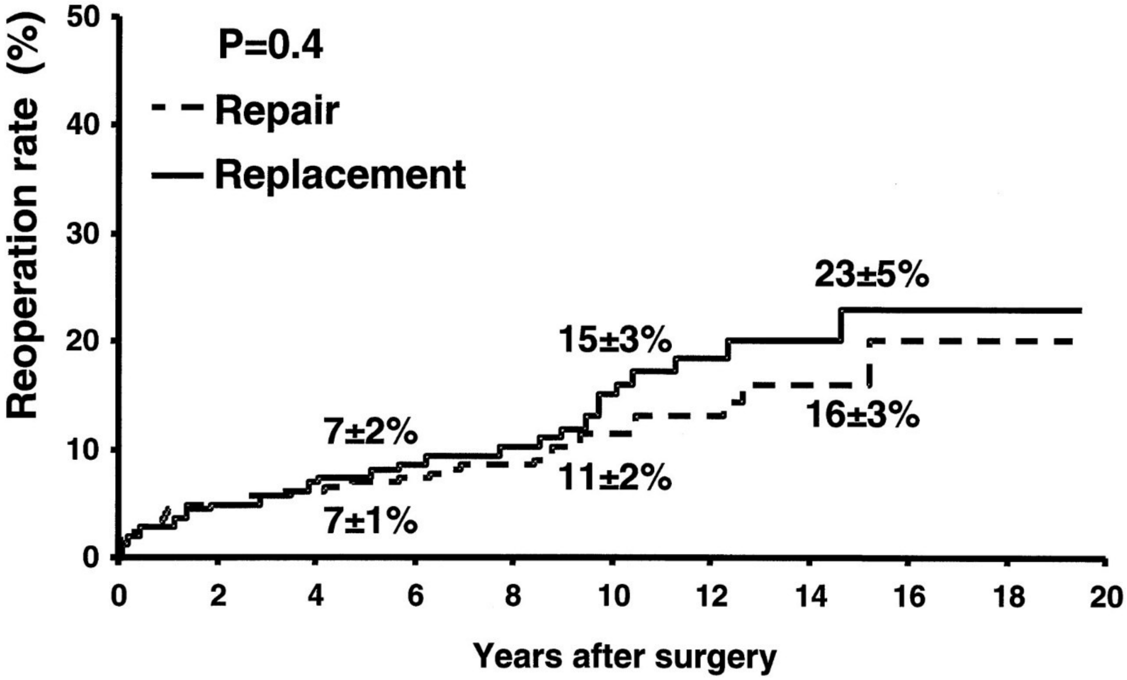

Figure 1.12: Long-term mitral prolapse reoperation rates after mitral repair (dashed line) and replacement (solid line). Reoperation rate estimates (mean±SE) are indicated at 5, 10, and 15 years [9].

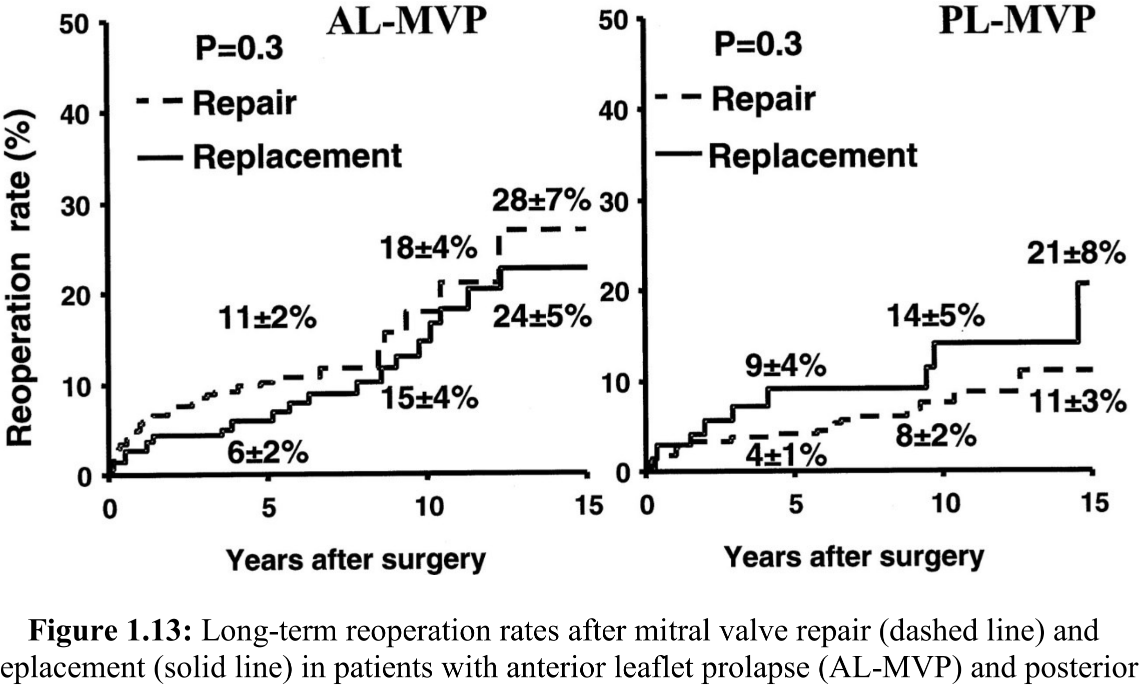

Figure 1.13: Long-term reoperation rates after mitral valve repair (dashed line) and replacement (solid line) in patients with anterior leaflet prolapse (AL-MVP) and posterior leaflet prolapse (PL-MVP). Reoperation rate estimates (mean±SE) are indicated at 5, 10, and 15 years [9].

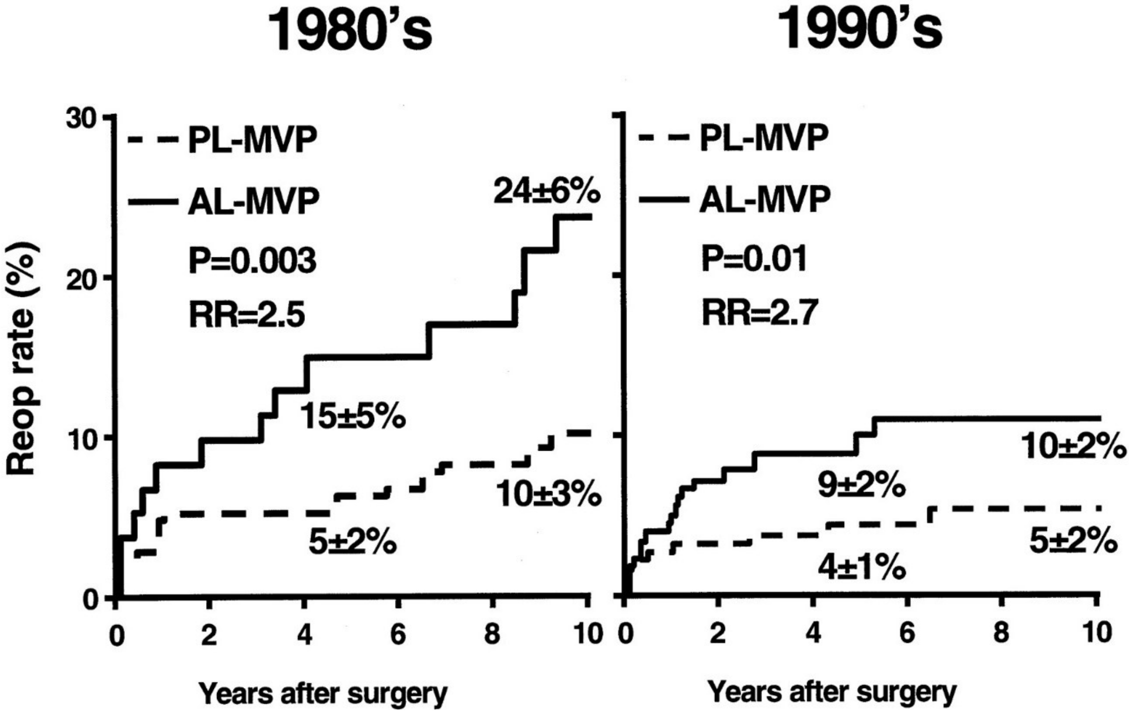

Figure 1.14: Reoperation (Reop) rates of repair in the 1980s (left) and 1990s (right) in patients with AL-MVP (solid line) and PL-MVP (dashed line). Reoperation rate estimates (mean±SE) are indicated at 5 and 9.94 (1990s) or 10 (1980s) years [9].

1.6. Objectives of the Study

As the most commonly diseased heart valve, the mitral valve has been researched extensively, with a large portion of this research focusing on the development and improvement of repair techniques. However, since mitral valve repair only gained widespread acceptance towards the end of the 20th century, long-term studies into the efficacy of mitral repair have only recently become possible. While these studies have confirmed that mitral repair is almost always preferable to replacement, they have also highlighted issues with current repair strategies. Since mitral repair, especially in the case of anterior leaflet prolapse, requires a very high level of expertise, current success rates are highly dependant on individual surgeon experience. Furthermore, early intervention to repair the valves of asymptomatic patients has proven beneficial but this only holds true if the surgery is of the highest quality [15], [35], [36]. Given the correlation between mitral repair (and success) rates based on surgeon experience, it is desirable to develop a tool for studying the mitral valve and predicting the outcomes of a variety of common surgeries. However, before mitral surgeries can be simulated, a tool must first be created to accurately model the dynamics of healthy mitral valves. The modeling of healthy mitral valves is essential to the validation of the model, and must be performed before mitral repair surgeries can be simulated. Specifically, this thesis seeks to develop a robust framework that is capable of generating accurate, patient-specific 3D models of healthy mitral valves so that we can analyze their dynamics using finite element analysis. Having received approval from the Ottawa Health Science Network Research Ethics Board, 16 healthy mitral valve datasets were provided by the University of Ottawa Heart Institute, of which seven were eliminated due to poor image quality, and the remaining nine datasets were then processed and modeled.

1.7. Contributions

The following contributions are presented in this thesis:

A novel method for determining the value of the Lagrange multiplier, *p*

The Lagrange multiplier, p, is a penalty term that is used to enforce the incompressibility constraint in the strain energy functions, which are used to define the mechanical behaviour of soft tissues. However, to the best of my knowledge, no method has been developed to calculate the value of this Lagrange multiplier, and as a result the common practice is to assume a large value for p [37]. In Section 3.1.5 a novel method for optimizing the value of the Lagrange multiplier, p, is proposed. Initial results from several mitral valve simulations that utilized optimized p values are promising, with the benefits of reduced simulation runtimes and improved accuracy of the simulated mitral valve dynamics.

Accurate modeling of local variations in leaflet thickness using TEE datasets

Currently, most research into the modeling of the mitral valve from ultrasound datasets has neglected to account for variations in leaflet thickness, and instead assumed leaflet thicknesses based on previously reported results [38]–[41]. In fact, to the best of my knowledge, only one study, by Pouch *et al.* [42], has attempted to model local variations in leaflet thicknesses using TEE datasets. Furthermore, the leaflet thicknesses that were obtained in this study were significantly larger than is typically expected from healthy mitral leaflets. In Chapter 4 a novel method for accurately modeling both the atrial and ventricular surfaces of the mitral leaflets is presented. Using this method, nine healthy mitral valves were reconstructed from ultrasound datasets that were provided by the University of Ottawa Heart Institute. The resulting finite element models were all found to closely approximate the real mitral valve geometries, and the leaflet thicknesses were all within the expected range for healthy mitral leaflets.

1.8. Thesis Organization

The remainder of this thesis is organized as follows:

Chapter 2 provides a literature review of current research in patient-specific modeling of the mitral valve, and gaps in the current modeling techniques are identified.

Chapter 3 discusses the mechanical properties of the mitral leaflets and chordae tendineae, and how these properties were modeled in the finite element simulations.

Chapter 4 describes the generation of the finite element models of the mitral apparatus. This includes the procedures implemented for the collection of the geometric data from patient-specific TEE datasets, the generation of the finite element models, and the simulations run in the FEA software LS-DYNA.

Chapter 5 details the results of the simulations, and compares these results to previously reported results.

Chapter 6 presents the conclusions of the research and provides recommendations for future work.

Appendix A details the derivation of the principal Cauchy stresses from three different strain energy models.

Appendix B provides the MATLAB code for certain programs that were required for the generation of the finite element models and the simulations.

Appendix C presents the relevant results from all of the mitral valve simulations.

Appendix D contains a copy of the ethics approval that was obtained to download the TEE images for analysis.

Chapter 2

2. Literature Review

An extensive amount of research has been dedicated to improving our understanding of the native mitral valve. Specifically, the generation of accurate models of the mitral valve has garnered significant interest. However, due to the complex nature of the mitral geometry, material properties, and boundary and loading conditions many simplifications have been employed for modeling purposes. Despite these simplifications, significant progress has been made in the modeling of the mitral valve, including the simulation of mitral repair techniques. This section highlights previous attempts at generating accurate mitral valve models, predicting surgical results, and the simplifications and assumptions that were employed.

2.1. Finite Element Modeling of the Mitral Valve

Finite element analysis (FEA) is a computational tool that employs the finite element method (FEM) to analyse complex problems. The FEM is a numerical technique that can be used to find approximate solutions to complex problems by dividing the whole problem into smaller parts, termed elements. These elements are defined by points, which are called nodes, and a set of governing equations. These equations, which are usually partial differential equations, are then solved by minimizing an associated error function, resulting in an approximate solution for each element. Therefore, combining the solution of all of the elements provides an approximate solution to the whole problem. The following three aspects are essential to the FEM, and therefore FEA: the problem geometry, the material properties, and the boundary and loading conditions. The quality of any finite element (FE) model of the mitral valve can therefore be assessed based on the accuracy of these three aspects when compared to the native mitral valve.

2.1.1. Mitral Valve Geometry

Any abnormalities in the mitral morphology can have a significant impact on its function. Therefore, the two main challenges faced when modeling the mitral valve are (1) accurately imaging and modeling the anatomical structure of the mitral apparatus, and (2) obtaining accurate measurements on the mitral valve in its natural setting. Consequently, early attempts to model the mitral valve utilized simplified FE models to simulate mitral valve function, and were often generated using data obtained from excised porcine valves. However, several research groups have recently started implementing strategies to develop 3D mitral valve models from patient-specific data sets.

The first attempt to utilize *in vivo* data to generate an accurate, patient-specific model of the mitral valve employed 4D TEE and was undertaken by Votta *et al.* in 2008 [40]. Since the transvalvular pressure-gradient is negligible at end-diastole, this state was selected for geometric reconstruction. A semi-automatic reconstruction procedure was developed consisting of three consecutive steps to reconstruct (1) the annulus and papillary muscle tips, (2) the leaflets, and (3) the chordae tendineae [40]. Thirty-six points on the annulus were manually selected, as well as a point at the tip of each of the (two) papillary muscles. Sixth-order Fourier functions were then used to generate a continuous annular profile. Instead of generating the leaflet geometries from the TEE data, Votta *et al.* opted to use previously reported anatomical measurements (reported by Kunzelman *et al.* in 1994). These measurements were used to generate a sinusoidal function to describe the annulus-to-free margin extent of the leaflets, which were then discretized using 48 480 three-node shell elements with thicknesses of 1.32 mm and 1.26 mm for the anterior and posterior leaflets, respectively [40]. Finally, 58 marginal and two strut chordae with cross-sectional areas of 0.4 mm^2 and 2.05 mm^2 respectively, were modelled as straight strings (without any branches) originating from the two papillary muscles [40].

In 2011, with patient-specific modeling of the mitral valve gaining interest, Jassar *et al.* published the results of a study that demonstrated a high level of reproducibility of 3D mitral valve modeling using 3D TEE [43]. For this study, all analyses were performed at mid-systole, and a geometric centre of the mitral orifice was defined by the point of intersection of the long-axis planes corresponding to the intercommissural septolateral axes of the mitral orifice [43]. Eighteen cross-sectional images were taken in 10° increments rotated about the long-axis, with two annular points being identified in each cross-section. The commissures were also manually identified, defined as the annular points at the middle of the commissural region [43]. The leaflets were then traced manually and the coaptation zone was independently identified in parallel, long-axis cross-sections 1 mm apart [43]. Since this study did not aim to analyse mitral dynamics, the papillary muscle tips and chordae tendineae were not modeled.

Then, in 2012, this group introduced another method that utilizes 3D TEE to reconstruct the mitral valve at mid-systole. This technique was a two-step process requiring extraction of a user-initialized region of interest, followed by 3D active contour segmentation [42]. By utilizing a continuous 3D medial representation to model the shape of the leaflets, local variations in leaflet thickness could be included in their model. Furthermore, the two leaflets were modeled as two separate entities. To generate the FE model, the atrial surfaces of the two leaflets were imported into HyperMesh 10.0 (Altair

Inc.) as triangular elements, where the mesh was refined, and the leaflets were modeled as thin shells (using the thickness measurements from the medial representation) [42]. The two papillary muscle tips were modeled as fixed single points, with only rotational freedom, and 32 chordae tendineae originating from each [42]. These chordae were inserted symmetrically into both leaflets along the free edges (marginal chordae), and more peripherally (secondary chordae), and were modeled as tension-only truss elements [42].

In 2011 and 2012 Mansi *et al.* published two papers that introduced an automated mitral modeling technique that employed machine-learning algorithms to automatically detect and track the mitral valve in 4D TEE images [38], [44]. To generate their model, nine anatomical landmarks (two trigones, one posterior annulus mid-point, two commissures, two leaflet tips, and two papillary muscle tips) were automatically detected and tracked over one heartbeat [38], [44]. These landmarks were then used to generate the atrial surface of the anterior and posterior leaflets. Since TEE was used to estimate the mitral anatomy, the chordae could not be automatically detected, and as a result the marginal and basal chordae insertion points were identical for all subjects. While four basal chordae were used in both studies, the number of marginal chordae (which were distributed evenly along the free edge of the leaflets) was reduced from 30 in the earlier study to 28 in the second study. Furthermore, due to the inconsistency of ultrasound images, their program was unable to accurately predict leaflet thicknesses. Consequently, they were required to assume a leaflet thickness of 2 mm for both leaflets in their earlier study. However, for their second study Mansi *et al.* reduced the leaflet thicknesses to 1.32 mm and 1.26 mm for the anterior and posterior leaflets, respectively.

In 2013, another mitral modeling technique that focused on accurately modeling patient-specific annular motion using 4D TEE was released by Rim *et al.* [39]. The leaflets were manually traced at end-diastole in 18 evenly spaced, cut-plane images rotated (10° increments) about the long-axis. To account for patient-specific annular motion, the annular geometry was segmented and traced manually at peak-systole as well [39]. To generate the 3D model of the mitral leaflets and annulus, non-uniform rational B-splines were used to model a continuous leaflet surface from the 18 slices [45]. Furthermore, since only one line was traced through the centre of the leaflets, thicknesses of 0.69 mm and 0.51 mm were assumed for the anterior and posterior leaflets, respectively [39], [45]. Instead of marking the anatomical location of the papillary muscle tips, Rim *et al.* opted to model them as two points that maintained a constant distance of 38 mm from the top of the annulus, with a distance of 18 mm between the two tips during annular motion [39]. Ten marginal chordae and one strut chordae originated from each papillary muscle tip, with each of the chordae branching out into six separate chordae branches before attaching to the leaflets [39], [45]. The cross-sectional areas of the anterior marginal chordae, posterior marginal chordae, and strut chordae were assumed to be 0.29 mm^2, 0.27 mm^2, and 0.61 mm^2, respectively [39], [45].

Although the majority of research into developing patient-specific 3D mitral valve models has focused on employing 4D TEE to acquire the required anatomical information, some groups have utilized other imaging methods to develop more accurate mitral models. In 2011, Stevanella *et al.* employed CMR images to generate patient specific mitral models. Despite the superior image quality offered by CMR, Stevanella *et al.* were still unable to accurately determine the leaflets thicknesses, or the distribution of the chordae, and as a result were forced to make many of the same assumptions that were required when TEE images were used [46]. Then, in 2012, Wang and Sun used multi-slice CT scans to acquire a 3D image at mid-diastole with distinguishable leaflet thickness, chordal origins, chordal insertion points, and papillary muscle locations [47]. Furthermore, they were also able to acquire the motion of the annulus and papillary muscle tips. While other studies have succeeded in using TEE to track annular motion, the use of CT images enabled the creation of a much more accurate mitral model (Figure 1.1). Despite the advantages offered by these imaging techniques, most efforts to create patient-specific mitral valve models continue to focus on TEE imaging techniques.

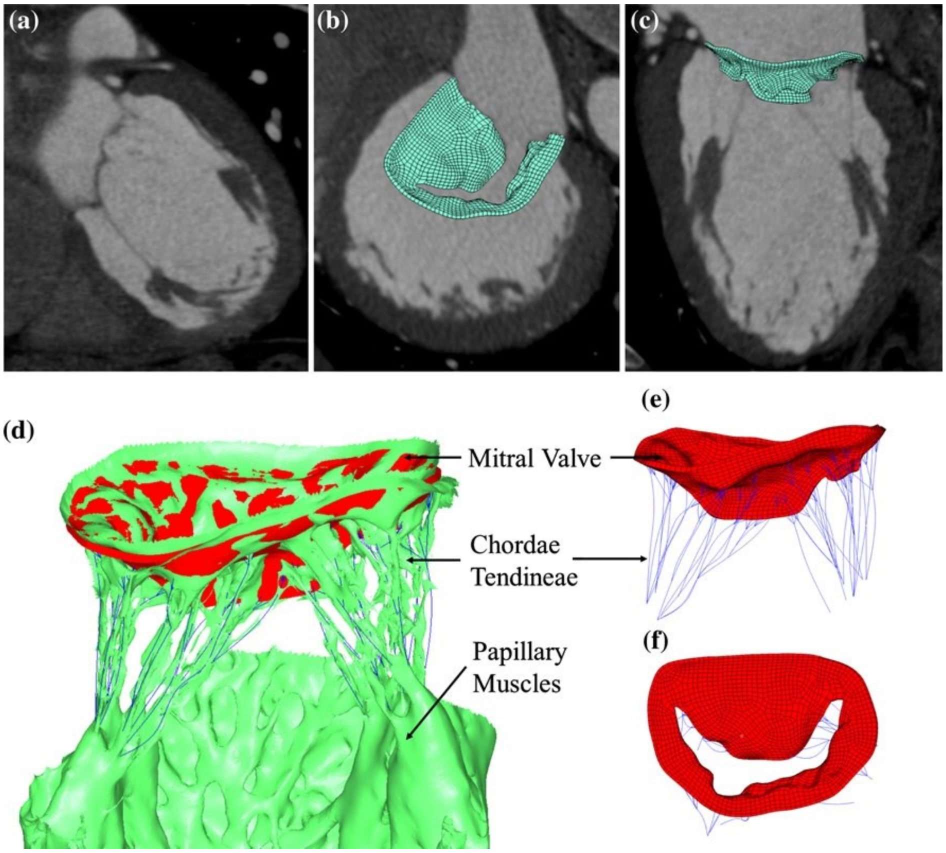

Figure 2.1: (a) Coronal view of the mitral valve and (b) top and (c) side views of the reconstructed FE mitral valve model overlapped with the multi-slice CT images. (d) Side view of the 3D mitral geometry (green) reconstructed from multi-slice CT images with the chordae tendineae, and papillary muscle tips. (e) Side view and (f) top view of the FE mitral model (red) [47].

2.1.2. Material Properties

When generating a FE model of the mitral valve, accurately modeling the mechanical properties of the individual structures presents its own challenges. The soft tissues that form the mitral leaflets and chordae are composed of cells and fibrous tissues, resulting in highly nonlinear, anisotropic elastic behaviour. Generally, these tissues are considered to be transversely isotropic, meaning that the material has a preferred direction (the mean of a distribution of fibre directions), but is otherwise isotropic [48]. Due to the crimping of the fibres, these tissues display an initial region of low stiffness, allowing large deformations at low loads. However, as the fibres straighten, the tissue becomes much stiffer. A variety of models have been employed in an attempt to accurately model this behaviour, but the nonlinear stress-strain behaviour of biological tissues is not the only challenge faced when modeling the biological material properties. Mechanical tests must first be performed on the biological tissues to determine the materials' mechanical properties before a mathematical model that approximates these properties can be generated. Unfortunately, very little material data is available for the mitral leaflets and chordae. Furthermore, many of the studies that were performed to help characterize the material properties of the mitral tissues were not performed on human samples.

Kunzelman and Cochran first analyzed the mechanical behaviour of mitral tissues in 1992. For their experiment, rectangular strips were excised from fresh, whole, porcine mitral valve leaflets, with the long axis either parallel or perpendicular to the annulus [49]. Having previously determined that the collagen fibres are roughly parallel with the annulus, these orientations were selected to determine the stress-strain behaviour of the leaflets when loaded parallel and perpendicular to the collagen fibres. Using uniaxial tensile tests, they were able to measure and model the stress-strain behaviour of the leaflets in the radial and circumferential directions. As expected, they determined that the leaflets were much stiffer in the circumferential direction (representing the preferred orientation of the collagen fibres).

Then, in 1995, May-Newman and Yin used biaxial tests to develop a more accurate model of the leaflets' stress-strain behaviour. By stretching samples of porcine mitral leaflets in both the radial and circumferential directions simultaneously [50], May-Newman and Yin determined that the stress-strain behaviour in both directions was not entirely independent, as had been assumed by Kunzelman and Cochran [49]. Using these data, the authors were able to develop a constitutive law that utilized strain energy theory (relating to hyperelastic materials) to describe the stress-strain behaviour of healthy, porcine mitral leaflets [51]. By assuming that the leaflets behave as transversely isotropic materials in which the strain energy function, W, depends only on two coordinate invariant measures of finite deformation (I_1 and I_4) the following exponential strain energy model was selected [51]:

$$W = c_0(e^Q - 1) \qquad \textbf{(2.1)}$$

where,

$$Q = c_1(I_1 - 3)^2 + c_2\left(\sqrt{I_4} - 1\right)^4 \qquad \textbf{(2.2)}$$

Here, c_0, c_1, and c_2 are material constants, while I_1 is the first invariant of the right Cauchy-Green strain tensor ($\boldsymbol{C}$), and I_4 is an invariant of the same tensor that is formed from the unit vector, $\boldsymbol{M}$, that defines the preferred fibre orientation in the reference configuration.

$$I_4 = \boldsymbol{M} \cdot \boldsymbol{C} \cdot \boldsymbol{M} \tag{2.3}$$

Unfortunately, there is very little data available on the material properties of human mitral valves. In 2010, Prot *et al.* used cyclical uniaxial tensile tests to model the mechanical properties of the anterior and posterior leaflets, and chordae tendineae from an elderly heart showing no disease, and a hypertrophic obstructive cardiomyopathic heart (HOCM) [52]. For their study, three different strain energy equations were selected; one equation (2.4) to model the anterior and posterior leaflets of the HOCM mitral valve, the second equation (2.5) to model the healthy leaflets, and the final equation (2.6) to model the stress-strain behaviour of the chordae tendineae.

$$W = \mu(I_1 - 3) + c_0\left(e^{c_1(I_1-3)^2 + c_2(I_4-1)^2} - 1\right) + \kappa(J-1)^2 \tag{2.4}$$

$$W = \mu(I_1 - 3) + c_0\left(e^{c_1(I_1-3)^2 + c_2(I_4-1)^4} - 1\right) + \kappa(J-1)^2 \tag{2.5}$$

$$W = a_0(I_1 - 3) + a_1\left(e^{a_2(I_4-1)^4} - 1\right) + p(J-1), I_4 \geq 1 \tag{2.6}$$

Here, μ, c_0, c_1, c_2, a_0, a_1, and a_2 are all material constants, κ (= 10^6 MPa) and p are positive, user-defined penalty terms, and J is the determinant of the deformation gradient tensor, $\boldsymbol{F}$. Despite their efforts, the results of their tests on the leaflet properties are of limited use for modeling purposes since the May-Newman study already highlighted the importance of biaxial testing for the characterization of material properties. Furthermore, Prot *et al.* were only able to excise a part of the HOCM valve, and as a result they were unable to determine the mechanical properties of the posterior leaflet in the radial direction. Consequently, they were forced to assume that the uniaxial mechanical behaviour of the HOCM posterior leaflet in the circumferential and radial directions have the same shift as was seen in the healthy posterior leaflet [52]. However, their work to model the chordae tendineae is far more valuable since the chordae are only subjected to uniaxial strains *in vivo*.

Then, in 2013, Pham and Sun first published the results of their own study that examined the mechanical properties of human mitral leaflets. For this study, 21 samples of aged human mitral valve leaflets (mean age 82.62 ± 8.77-years-old) were subjected to stress-controlled biaxial tests [53]. To characterize the nonlinear, hyperelastic behaviour of the leaflets Pham and Sun opted to use the following (Fung-type) strain energy model:

$$W = \frac{c}{2}\left(e^{Q} - 1\right) \tag{2.7}$$

$$Q = A_1 E_{11}^2 + A_2 E_{22}^2 + 2A_3 E_{11} E_{22} + A_4 E_{12}^2 + 2A_5 E_{11} E_{12} + 2A_6 E_{22} E_{12} \tag{2.8}$$

where c and $A_{1\text{-}6}$ are material constants, E_{11} and E_{22} are the Green-Lagrange strains in the circumferential and radial directions, respectively, and E_{12} is the Green-Lagrange shear strain [53]. From these results, they were able to confirm that the anterior leaflet in humans is stiffer than the posterior leaflet, and that the radial direction was far more compliant than the circumferential direction, as was the case with porcine valves. Furthermore, they found that leaflets from hypotensive hearts exhibited a higher stiffness than normotensive hearts, and that stiffness increased with calcification severity [53]. This data could prove critical in accurately modeling diseased human mitral valves since most models use porcine material data, which is far more compliant than diseased human valves.

While these strain energy equations have proven capable of accurately modeling the highly nonlinear, anisotropic behaviour of the mitral leaflets, implementing this type of material data in FE models presents its own challenges. Consequently, early FE models of the mitral valve assumed that the leaflets behaved as linear elastic materials. In fact, this assumption has re-emerged recently [38], [42], [44] since it was suggested by Krishnamurthy *et al.* that the mitral leaflets may behave as linear, transversely isotropic materials during systole [54]. Despite these results Mansi *et al.* found that while their linear elastic model was capable of accurately modeling anterior leaflet billowing, this assumption negatively impacted the closure of the mitral valve [38].

Accurately modeling the mitral valve is further complicated since some studies have suggested that the mitral valve's *in vivo* mechanical properties do not match those measured *in vitro*, which could result from the presence of contractile elements within the leaflets. In an attempt to model the nonlinear, hyperelastic behaviour of the anterior leaflet, Stevanella *et al.* employed a time-varying elastic modulus to model the *in vivo* mechanical properties of three ovine anterior leaflets [55]. Radiopaque markers were sewn to the mitral valve, and their 4D coordinates were obtained using biplane video fluoroscopy. Using the coordinates of these markers, the anterior leaflets' geometries were reconstructed at the end of isovolumetric relaxation. The anterior leaflet function was then simulated backwards through systole, using the known marker coordinates along the annulus and free edge of the leaflet for the boundary conditions, and by applying the measured trans-mitral pressure [55]. The systolic phase was divided into four time segments from the end of isovolumetric relaxation to early systole, and the radial and circumferential elastic moduli were increased from 9-15 MPa and 28-44 MPa, respectively over the four time segments [55]. While the reported results by Stevanella *et al.* were consistent with the known *in vivo* measurements, they were unable to include the posterior leaflet in their model, and therefore any leaflet contact forces were neglected. Furthermore, the constraints on the motion of the leaflets' free edge may have reduced the importance of accurately estimating the leaflets' mechanical properties.

Currently, the most common approach to modeling the anisotropic, hyperelastic behaviour of the mitral leaflets is to implement a strain energy equation that is designed to accurately model the results from *in vitro* tensile tests. Einstein *et al.* were the first to apply the mitral valve data and the strain energy function developed by May-Newman and Yin into a finite element model in 2003 [56], which led them to the first successful implementation of a hyperelastic material model in a finite element model of a mitral valve in 2004 [57]. Later, in 2007, Prot *et al.* implemented a new strain energy function for the mitral valve (Equation (2.9) and Equation (2.10)) [58] that was based off of the strain energy function developed by Holzapfel *et al.* for modeling arterial walls [59].

$$W = c_0(e^Q - 1) \quad \textbf{(2.9)}$$

$$Q = c_1(I_1 - 3)^2 + c_2(I_4 - 1)^2 \quad \textbf{(2.10)}$$

Prot *et al.* found that this model was not only more robust, but also provided faster computational results. In 2008 Votta *et al.* also implemented this strain energy equation to model the isotropic, hyperelastic behaviour of the anterior and posterior mitral leaflets in their finite element model [40]. Another mitral valve model, developed in 2011 by Stevanella *et al.*, implemented the hyperelastic model developed by May-Newman and Yin (Equation (3.15) and Equation (2.2)) in the finite element software ABAQUS to simulate mitral valve closure.

In 2012, Rausch *et al.* used ABAQUS to simulate the closure of a mitral valve for three different strain energy equations [60]. The first material model (Equation (2.11)), a

Neo-Hookean model, is the most simplistic since it does not account for the anisotropic microstructure of the leaflets. The second material model was the coupled, anisotropic model used by Prot *et al.* (Equation (2.9) and Equation (2.10)). Finally, a modified version of the original decoupled Holzapfel model, which includes the additional parameter γ to incorporate microstructural fibre dispersion, was implemented (Equation (2.12) and Equation (2.13)).

$$W = c_0(I_1 - 3) \tag{2.11}$$

$$W = c_0(I_1 - 3) + \frac{c_1}{2c_2}(e^Q - 1) \tag{2.12}$$

$$Q = c_2[\gamma I_1 + (1 - 3\gamma)I_4 - 1]^2 \tag{2.13}$$

Here the notations are identical to those previously defined, and γ is a constant ($0 \leq \gamma \leq 1/3$). When $\gamma = 0$ the material is completely decoupled with no fibre dispersion, and when $\gamma = 1/3$ the fibre distribution is completely random, and therefore the material is isotropic [60]. Using these three material models, Rausch *et al.* determined that both anisotropic models were able to provide excellent fits to the *in vivo* data, but were highly sensitive to prestrain. However, while the material constants varied significantly (up to four orders of magnitude) for varying levels of prestrain, only small changes in the leaflet displacement error were observed. Rausch *et al.* also found that while the coupled model was able to model experimental biaxial test results much more accurately, the decoupled model actually provided slightly more accurate *in vivo* results.

The Fung-type model that was employed by Pham and Sun to model the mechanical properties of aged human mitral leaflets (Equation (2.7) and Equation (2.8)) was also implemented by Rim *et al.* in the finite element analysis software ABAQUS to model the anterior and posterior mitral leaflets [39], [45]. For their simulations, they employed previously reported porcine material properties and leaflet thicknesses (from May-Newman and Yin) [51], and assumed negligible shear strains (i.e. $E_{12} = 0$). The latter assumption was necessary since biaxial tests typically induce low shear strains, and therefore the coefficients A_4, A_5, and A_6 cannot be reliably determined from the experimental data.

Unfortunately, there are concerns that these strain energy functions may not be sufficiently accurate to predict the *in vivo* behaviour of the leaflets. These models assume that the leaflets' mechanical characteristics are uniform across the entire leaflet. However, the collagen fibres within the leaflets, which are responsible for the leaflets' anisotropic behaviour, are not distributed uniformly throughout the leaflet. While the collagen fibres are roughly parallel to the annulus throughout the majority of the leaflet, the fibres begin to rotate near the commissures, where they are roughly perpendicular to the annulus [61]. Consequently, the leaflets should be stiffer in the radial direction than the circumferential direction near the commissures. In 2010, using the results from their uniaxial tensile tests on healthy and HOCM human mitral leaflets, as well as porcine data, Prot *et al.* employed the ORIENT subroutine in ABAQUS (along with the hyperelastic model described in Equation (2.4) and Equation (2.5)) to set the orientation of collagen fibres according to mean collagen fibre direction maps [52].

The same year, Skallerud *et al.* published the results of a study that included muscle fibres, and location-dependant collagen fibre orientations. Like Prot *et al.*, Skallerud *et al.* used previously obtained mean collagen fibre direction maps to set the orientation of the collagen fibres throughout the anterior and posterior leaflets. Since previous studies suggested that muscle fibres were only present in certain areas of the leaflets, the muscle fibres were only modeled in the central part of the anterior leaflet from the annulus to the middle of the leaflet, and in a 4 mm strip along the annulus of the posterior leaflet [41]. The addition of contractile elements required a new strain energy function to accurately model the leaflets' mechanical behaviour. Therefore, a new strain energy equation that consisted of three terms—a passive isochoric term, which is identical to the strain energy function used by Prot *et al.* in 2007 (Equation (2.9) and Equation (2.10)), an active isochoric part (Equation (2.15)), and a volumetric portion—was created.

$$W = c_0(e^Q - 1) + W_a(I_6) + W_a(I_4) + \kappa(J - 1)^2 \tag{2.14}$$

$$Q = c_1(I_1 - 3)^2 + c_2(I_4 - 1)^2 \tag{2.15}$$

$$W_a(I_i) = \frac{1}{2}\sigma_{max} f(t)[(I_i - 1)], \qquad i = 4, 6 \tag{2.16}$$

Here σ_{max} is the maximum activation stress of the muscle fibres, and $f(t)$ is a function that defines the change in the activation stress over a heartbeat. Since there was insufficient information available to accurately model the *in vivo* contractile behaviour of the muscle fibres within the leaflets, a very simplistic (linear) muscle activation model was employed [41]. Despite this limitation, Skallerud *et al.* found that this contractile model was far more accurate at predicting the deflection of the leaflets (into the left atrium) during systole than their previous passive material models [41].

In 2012 Wang and Sun also employed mean collagen fibre direction maps to include fibre orientations in their mitral valve model. While they did not include contractile elements like Skallerud *et al.*, they were able to create a more accurate mitral model by using multi-slice CT images. When modeling the mitral tissues, Wang and Sun developed their own hyperelastic material model (based on the model proposed by Holzapfel *et al.*) which assumed the mitral valve was composed of a matrix material with two families of embedded fibres, each with a preferred direction (Equation (2.17) and Equation (2.18)) [47].

$$W = c_0\left(e^{c_1(I_1-3)} - 1\right) + \frac{k_1}{2k_2}\sum_{i=1}^{2}(e^{Q} - 1) + \frac{1}{D}(J-1)^2 \quad \mathbf{(2.17)}$$

$$Q = k_2[\kappa I_1 + (1-3\gamma)I_{4i} - 1]^2 \quad \mathbf{(2.18)}$$

The naming conventions are the same here as were previously defined, with the strain invariant I_{4i} equal to the squares of the stretches in the i^{th} fibre direction. When the material properties of a human mitral valve were obtained from biaxial tests and characterized using this equation, Wang and Sun were able to accurately simulate the closed shape of the mitral valve geometry which was reconstructed from the multi-slice CT images. However, when material properties from a 69-year-old male human mitral valve and a porcine valve were used, they were unable to reproduce the systolic mitral valve deformation that was observed in the CT images [47]. These results highlight the importance of material property selection, which can be affected by both age and pathology.

2.1.3. Analysis Methods

The final major area of differentiation between finite element models of the mitral valve is the type of analysis employed, and the boundary and loading conditions. For the purpose of examining the dynamics of the mitral valve, there are two analysis methods that can be employed—structural analyses, and fluid-structure interaction (FSI) analyses. Structural analyses, which neglect the flow of blood through and around the valve, are by far the most commonly employed analysis method. Fluid-structure interaction analyses, on the other hand, model the dynamics of the mitral valve by including blood flow in the model. While the loading and boundary conditions vary depending on the source data as well as the analysis type, they are generally selected to match the source data (either from *in vivo* images or *in vitro* experiments), as closely as is feasible, for the implementation in the FE model.

In structural analyses, the effect of blood flow is replaced by a pressure load that is applied to the ventricular surface of the mitral leaflets. Since structural analyses cannot simulate blood flow through the mitral valve, these analyses are only concerned with the closure of the valve. Therefore, these analyses generally neglect the diastolic phase of the heartbeat, and often only a portion of the systolic phase is considered. The pressure loads are derived from the pressure difference between the left atrium and left ventricle, and are either based on *in vivo* transvalvular pressure measurements, or data obtained from previous studies. The initial mitral geometry is most commonly obtained from images at end-diastole (the last time frame before the valve closes) [38]–[41], [44]–[46], [52], [58] since the transvalvular pressure is negligible at this stage of the heartbeat. However, a few studies have reconstructed the valve using images at the end of the isovolumetric relaxation phase [55], [60], while Pouch *et al.* used peak systole to generate a mitral valve model in one study [42]. Since these studies are focused on identifying the valve behaviour at closure, the analyses only considered a portion of the systolic phase in order to reduce the time, in most cases. The simulations were generally run from end-diastole to peak-systole [38], [40], [41], [44], [46], [52], [58], however in both studies where the valve was reconstructed at the end of isovolumetric relaxation, the simulations were run backwards from the end of isovolumetric contraction to early systole [55], [60]. Although the diastolic behaviour of the mitral valve is of little interest in structural models, a few studies have modeled the dynamics of the mitral valve over the entire heartbeat [39], [45], [47]. The applied pressure loads are usually defined to approximate the shape of the curve, that approximates the pressure drop across the mitral valve (Figure 2.2), although one study by Lee *et al.* used static loads to compare their results with actual mitral geometries obtained at known static loads in a left heart simulator [10]. When a standard loading curve is employed, the main differences between these studies are the maximum transvalvular pressure drop (generally 80-120 mmHg), which is either assumed or obtained from *in vivo* measurements; the direction of loading (either the forward or reverse direction); and the user-defined start and end points of the simulation.

While structural models can be used to study the deformation and stresses in the mitral leaflets and chordae, they do not account for local variations in blood pressure and shear stresses that result from the flow of blood around the mitral apparatus. Furthermore, they are unable to predict changes in blood flow dynamics. These effects can only be examined using FSI analysis methods. However, generating a FSI model of the mitral valve presents a variety of challenges. Consequently, very few studies have employed FSI analyses to model the dynamics of the mitral valve. To accurately model the fluid dynamics through and around the mitral valve, an accurate model of the left heart is essential; otherwise the forces acting on the mitral valve may not be representative of the *in vivo* conditions. Recent efforts by Kunzelman *et al.* [62], [63] employed Neo-Hookean material models for the mitral leaflets, and reduced the bulk modulus of the blood by several orders of magnitude in order to improve the computational efficiency. While these FSI models marked significant advances in modeling valve dynamics, they were also limited to non-physiological valve dynamics [64]. Before this type of model can become useful in clinical settings, the numerical difficulties inherent to FSI analyses of complex valve dynamics must be overcome [64].

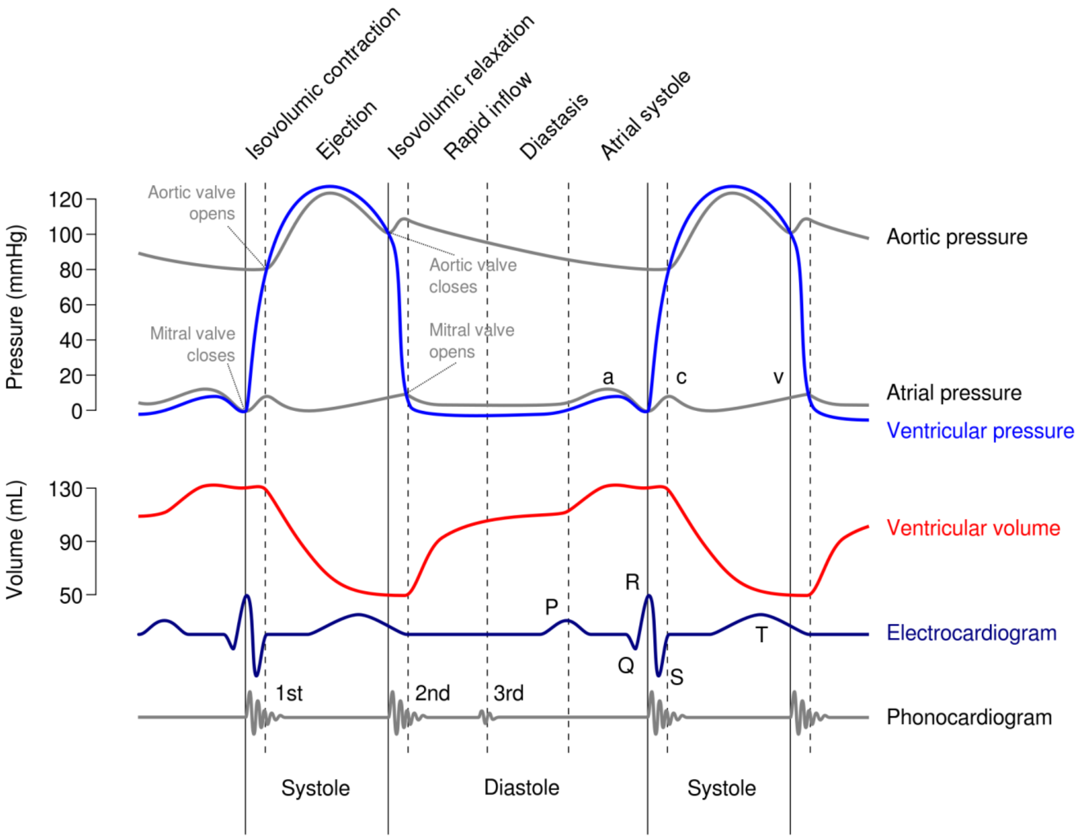

Figure 2.2: Wiggers diagram showing left atrial and ventricular pressures, along with various other events of the cardiac cycle [65].

The boundary conditions employed for both structural and FSI analysis methods aim to model the *in vivo* mitral dynamics as closely as possible, and are therefore essentially the same. Since the mitral annulus and papillary muscle tips are the only locations where the mitral apparatus is secured to the heart, this is where the boundary conditions are applied. The most simplistic boundary conditions assume that the annulus and papillary muscle tips are fixed with respect to translation, but are free to rotate [41],

[42], [52], [57], [58]. Recently, several studies have used the 4D images of the mitral valve to track the annulus throughout the cardiac cycle. Using this data, the annular displacements can be applied as boundary conditions to match the *in vivo* annular dynamics. With the tracking of annular displacements, the papillary muscle tip displacements are either set to maintain a constant distance from the annulus [39], [40], [45], or if the papillary muscle tips were also tracked throughout the cardiac cycle, their known temporal locations are applied as the boundary conditions [38], [44], [46], [47]. Contact between the mitral structures must also be considered when modeling the mitral valve. Finite element analysis software such as LS-DYNA and ABAQUS have settings built into the programs that can automatically detect and handle contact between surfaces. Unfortunately, since the diameter of the chordae is so small, these programs struggle to detect contact between the beams used to model the chordae and the other structures in the model.

2.2. Potential for Improvement

The current trend in mitral valve modeling is towards automation of the geometric reconstruction process, yet accurately modeling leaflet thicknesses has not garnered significant attention. Due to the limited resolution of the ultrasound images, most studies have assumed leaflet thicknesses based on previously reported results. However, variations in leaflet thicknesses will likely have a significant impact on the simulation accuracy of diseased valves. Therefore, to improve the accuracy of mitral valve simulations it is desirable to accurately model local changes in leaflet thicknesses. To the best of my knowledge, only one group has attempted to model local thicknesses of the mitral leaflets. Using a semi-automated approach, Pouch *et al.* were able to represent local variations in leaflet thicknesses [42]. While this study only examined two datasets, the mitral leaflets in their models had mean thicknesses ranging from 2.3-2.6 mm, which is over 1 mm thicker than is commonly assumed for healthy valves [38], [40]. Therefore, one major area that warrants further research is the accurate modeling of leaflet thicknesses. The other potential source for improvement is the modeling of the mechanical properties of the leaflet tissues. Unfortunately very little mechanical testing data is available for both healthy and diseased human mitral leaflets. Consequently, the leaflets are often modeled using porcine material data. In order to improve the accuracy of the leaflets' mechanical properties further biaxial tensile tests must be performed using human tissue samples.

Chapter 3

3. Material Properties

As was discussed in the previous chapter, accurately modeling and implementing the material properties of the mitral leaflets and the chordae tendineae is quite challenging. This chapter covers the microstructure of the biological tissues of the mitral valve to develop a greater understanding of the complex mechanical behaviour of the mitral tissues. The classic experimental procedures used to study the stress-strain behaviour of the tissues are also covered, as well as the assumptions required to convert these experimental data to theoretical material models. Finally, the original and specific procedures and assumptions employed in the present work to implement these mathematical models in the commercial FEA software LS-DYNA are justified.

3.1.Leaflet Properties

3.1.1. Microstructure and Mechanical Behaviour

The mitral leaflets are composed of a fibrous skeleton and an endocardial surface. While the atrial surface of both leaflets has a smooth, endocardial cell layer, only the anterior leaflet has an endocardial layer on the ventricular side [66]. The fibrous skeleton is composed of two distinct layers of tissue—the lamina spongiosa (atrial side), and the lamina fibrosa (ventricular side)—which are mainly composed of elastin fibres, collagen fibres, and glycosaminoglycans [51]. The network of collagen and elastin fibres in these layers determines the passive mechanical behaviour of the leaflets, with the preferred orientation of collagen fibres resulting in the observed anisotropy [51]. While elastin fibres exhibit linear stress-strain behaviour, relaxed collagen fibres are crimped, and therefore exhibit highly nonlinear stress-strain behaviour. These collagen fibres initially undergo large deformations at low stresses as they straighten; however, as the fibres straighten, the leaflets become much stiffer resulting in large increases in the stress over small deformations. The combination of the collagen and elastin fibres is responsible for the anisotropic, hyperelastic material properties that can be modeled using a strain energy function (W) as was previously discussed in Section 2.1.2. The leaflets also possess distinct patterns of innervation, and smooth muscle cells, suggesting that the contractile elements may play a role in mitral valve function [66]. However, since there is no data available on the *in vivo* behaviour of these contractile elements, only the leaflets' passive behaviour can be modeled accurately.

Although a variety of strain energy equations have been designed specifically to model the behaviour of the mitral leaflets (refer to Section 2.1.2), these material models are not available in the commercial FEA software LS-DYNA. However, LS-DYNA does implement another strain energy function that can be used to model the nonlinear, anisotropic behaviour of the mitral leaflets. This strain energy function was initially developed by Guccione *et al.* to model ventricular myocardium [67], but it has since proven successful in modeling other types of heart tissue as well [68], [69]. The Guccione model (implemented using MAT_HEART_TISSUE in LS-DYNA) is defined as

$$W = \frac{c}{2}(e^{Q} - 1) + \frac{p}{2}(III_{C} - 1)^{2} \tag{3.1}$$

where and III_C is the determinant of the right Cauchy-Green tensor, C, p is a Lagrange multiplier used to enforce the incompressibility constraint, and

$$Q = b_1E_{11}^2 + b_2(E_{22}^2 + E_{33}^2 + E_{23}^2 + E_{32}^2) + b_3(E_{12}^2 + E_{21}^2 + E_{13}^2 + E_{31}^2) \quad \textbf{(3.2)}$$

Here, c and b_i are material constants and E_{ij} is the Green strains in the circumferential (1), radial (2), and thickness (3) directions of the leaflets.

3.1.2. Experimental Material Properties

Regardless of the strain energy equation that is employed, the material constants must be determined from experimental data. Both uniaxial and biaxial tests have been employed by various groups to model the mechanical behaviour of mitral leaflets, however neither are capable of fully characterizing the 3D mechanical behaviour of the mitral leaflets [48]. Despite this fact, biaxial testing is currently the best available method for determining the mechanical properties of the mitral leaflets. For this thesis, the results of two separate studies that employed biaxial testing to determine mitral leaflet material constants were considered. The first study, by May-Newman and Yang, performed strain-controlled biaxial tensile tests on healthy porcine mitral leaflets [50], [51], while the second study, by Pham and Sun, performed stress-controlled biaxial tests on aged human mitral leaflets [53]. In both studies, sections of the mitral leaflets were mounted in a similar manner in the biaxial tensile testing apparatus (Figure 3.1a), and the Cauchy stresses and Green strains were calculated in the radial and circumferential directions (Figure 3.1b).

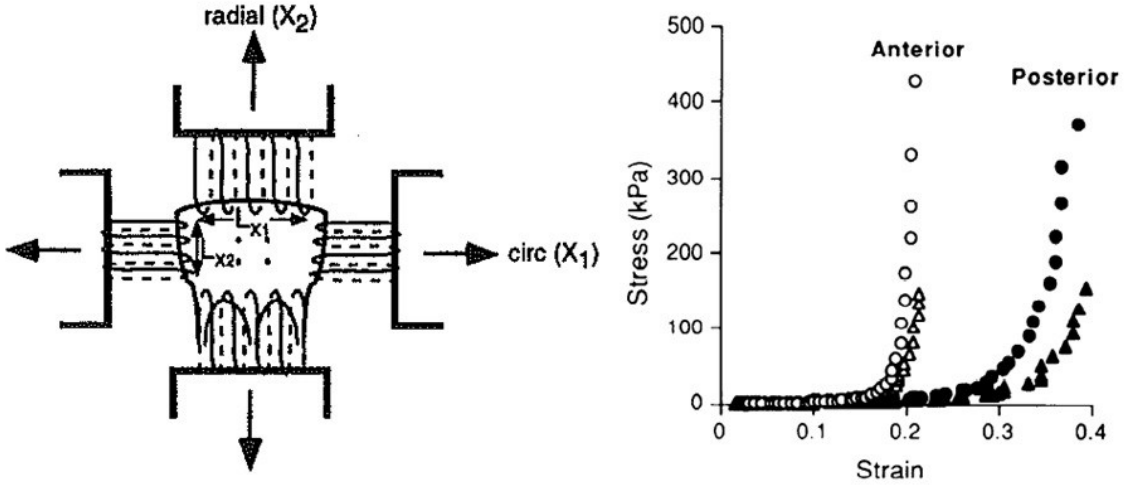

(a) (b)

Figure 3.1: (a) Biaxial testing apparatus for mitral leaflet samples [51]; (b) stress-strain relations for a mitral valve specimen. The circumferential and radial directions are depicted by circles and triangles, respectively [50].

3.1.3. Material Constant Evaluation

Unfortunately, since neither May-Newman and Yin, nor Pham and Sun chose the Guccione strain energy equation to model their experimental results, the optimized constants from these studies could not be directly implemented in LS-DYNA. Instead, it was necessary to calculate the Guccione material constants that best approximated their results. This was achieved by minimizing the error between the theoretical Cauchy stresses, which were determined using the reported strain energy equations and the associated material constants, and the Cauchy stresses calculated using the Guccione model. The Cauchy stress tensor,

$$\bar{\bar{t}} = \frac{1}{J}\left(\bar{\bar{F}} \cdot \bar{\bar{S}} \cdot \bar{\bar{F}}^T\right) = \frac{1}{J}\left(\bar{\bar{F}} \cdot \frac{\partial W}{\partial E_{ij}} \cdot \bar{\bar{F}}^T\right) \tag{3.3}$$

is a function of the deformation gradient $\bar{\bar{F}}$, and the 2nd Piola-Kirchoff stress tensor $\bar{\bar{S}}$. Here "·" represents the dot product between two tensors, and J is the determinant of $\bar{\bar{F}}$, which is the derivative of each deformed vector $\boldsymbol{x}$ with respect to the reference vector $\boldsymbol{X}$:

$$[\bar{\bar{F}}] = \begin{bmatrix} \frac{\partial x_1}{\partial X_1} & \frac{\partial x_1}{\partial X_2} & \frac{\partial x_1}{\partial X_3} \\ \frac{\partial x_2}{\partial X_1} & \frac{\partial x_2}{\partial X_2} & \frac{\partial x_2}{\partial X_3} \\ \frac{\partial x_3}{\partial X_1} & \frac{\partial x_3}{\partial X_2} & \frac{\partial x_3}{\partial X_3} \end{bmatrix} \tag{3.4}$$

However, since the tissue samples are taken from the belly area of the mitral leaflets, it is assumed that the collagen fibres are parallel to the annulus (aligned in the circumferential direction). Therefore, no shear stresses should exist during the biaxial tests and $[\bar{\bar{F}}]$ becomes a diagonal matrix.

$$[\bar{\bar{F}}] = \begin{bmatrix} \frac{\partial x_1}{\partial X_1} & 0 & 0 \\ 0 & \frac{\partial x_2}{\partial X_2} & 0 \\ 0 & 0 & \frac{\partial x_3}{\partial X_3} \end{bmatrix} = \begin{bmatrix} \lambda_1 & 0 & 0 \\ 0 & \lambda_2 & 0 \\ 0 & 0 & \lambda_3 \end{bmatrix} \tag{3.5}$$

Consequently, $\bar{\bar{F}}$ is a function of the stretch ratios $\lambda_i = l_i/L_i$ in the principal directions, where l_i is the stretched length and L_i is the initial side length. Furthermore, the mitral leaflets are assumed to be incompressible. Therefore $J = \lambda_1\lambda_2\lambda_3 = 1$ and the Cauchy stress tensor can be simplified to

$$\bar{\bar{t}} = \left(\bar{\bar{F}} \cdot \frac{\partial W}{\partial E_{ij}} \cdot \bar{\bar{F}}^T \right) \tag{3.6}$$

and the stretch ratios in the third principal direction can be defined in terms of the other two stretch ratios as follows:

$$\lambda_3 = \lambda_1^{-1}\lambda_2^{-1} \tag{3.7}$$

Therefore $\bar{\bar{t}}(\lambda_1, \lambda_2)$, and the Cauchy stresses are

$$t_{ij} = \begin{cases} 0 & if\ i \neq j \\ \lambda_i^2 \dfrac{\partial W}{\partial E_{ij}} & if\ i = j \end{cases} \quad \text{for } i, j = 1, 2, 3 \tag{3.8}$$

The Green strain tensor $\bar{\bar{E}}$ is defined by the right Cauchy stress tensor, $\bar{\bar{C}} = \bar{\bar{F}}^T \cdot \bar{\bar{F}}$, as

$$\bar{\bar{E}} = \frac{1}{2}\left(\bar{\bar{C}} - \bar{\bar{I}}\right) = \frac{1}{2}\left(\bar{\bar{F}}^T \cdot \bar{\bar{F}} - \bar{\bar{I}}\right) \tag{3.9}$$

where $\bar{\bar{I}}$ is the identity tensor. Therefore

$$E_{ij} = \begin{cases} 0 & if\ i \neq j \\ \frac{1}{2}(\lambda_i^2 - 1) & if\ i = j \end{cases} \quad \text{for } i, j = 1, 2, 3 \tag{3.10}$$

Furthermore, using the multivariable chain rule, Equation (3.8) can be expressed as follows:

$$t_{ij} = \begin{cases} 0 & if\ i \neq j \\ \lambda_i^2 \dfrac{\partial W}{\partial Q}\dfrac{\partial Q}{\partial \lambda_i}\dfrac{\partial \lambda_i}{\partial E_{ij}} & if\ i = j \end{cases} \quad \text{for } i, j = 1, 2, 3 \tag{3.11}$$

where

$$\frac{\partial W}{\partial Q} = \frac{c}{2} e^Q \tag{3.12}$$

and

$$\frac{\partial \lambda_i}{\partial E_{ii}} = \frac{1}{\sqrt{2E_{ii} + 1}} = \frac{1}{\lambda_i} \tag{3.13}$$

Finally, substituting Equation (3.12) and Equation (3.15) into Equation (3.11), the components of the Cauchy stress tensor become

$$t_{ij} = \begin{cases} 0 & if\ i \neq j \\ \dfrac{ce^{Q}\lambda_i}{2}\dfrac{\partial Q}{\partial \lambda_i} & if\ i = j \end{cases} \quad \text{for } i, j = 1, 2, 3 \tag{3.14}$$

Using the thin membrane approximation, the Cauchy stress across the thickness of the leaflet can be neglected. Therefore, only t_{11} and t_{22} are calculated since they are the only non-zero components of the Cauchy stress tensor. Using these results, the error is the difference between the theoretical Cauchy stresses and the Guccione model Cauchy stresses for the two principal directions (Equation (3.15)).

$$error_{t_{ii}} = t_{ii,theoretical} - t_{ii,Guccione} \quad \text{for } i = 1, 2 \tag{3.15}$$

The nonlinear least-squares curve fitting function lsqnonlin in MATLAB was then employed to optimize the Guccione material constants. Unfortunately, as was alluded to in Section 3.1.2, biaxial tensile tests cannot fully characterize the 3D mechanical behaviour of the mitral leaflets, and as a result the material constant b_3 in Equation (3.2) and the Lagrange multiplier, p, in Equation (3.1) could not be determined from the biaxial test data.

While the derivation of the Cauchy stresses was highlighted in this section, the full derivations for all three material models are available in Appendix A.

3.1.4. Simulated Biaxial Tensile Testing

Initially, the Guccione material constants (c, b_1, and b_2) were calculated directly in MATLAB by using the lsqnonlin function to optimize the Guccione material constants. The calculated material constants appeared to provide an excellent match (Figure 3.2). However, to confirm the accuracy of these results, a biaxial tensile test simulation was run in LS-DYNA using these constants in the material model MAT_HEART_TISSUE. Biaxial tensile testing was simulated by fixing two edges of a square leaflet specimen in LS-DYNA

(10 mm x 10 mm x 1 mm), while applying displacements to the other two edges. Unfortunately, when the material constants that were calculated in MATLAB were implemented in the LS-DYNA simulations, the results did not provide a close match to the experimental data (Figure 3.3). Therefore, it was necessary to create a new MATLAB program that could be used to calculate the Guccione material constants based on the results of the biaxial tensile test simulations in LS-DYNA. In essence here, LS-DYNA was used as a replacement of the ideal analytical solutions described by Equations 3.3 to 3.14. Again, lsqnonlin was employed to optimize the material constants, and for each iteration, the new material constants were used to run a biaxial tensile test simulation in LS-DYNA. The MATLAB program would then use the results of the simulation to calculate the Cauchy stresses, and the error. While this program took significantly longer to optimize the Guccione material constants (hours instead of seconds), the resulting model was a far superior match to the experimental data (Figure 3.4).

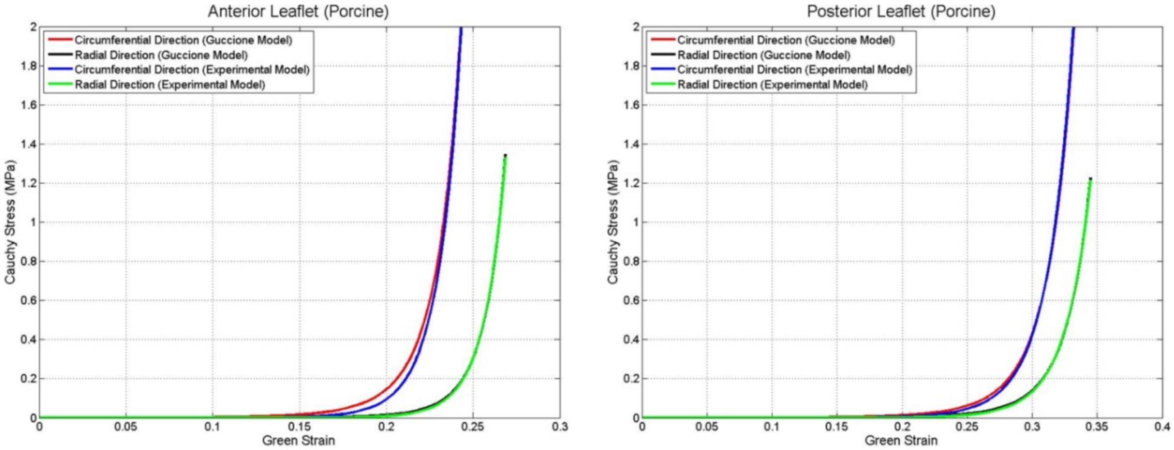

Figure 3.2: Mechanical behaviour of the anterior leaflet (left) and posterior leaflet (right) after optimization of the material constants in MATLAB to match May-Newman and Yin's experimental results.

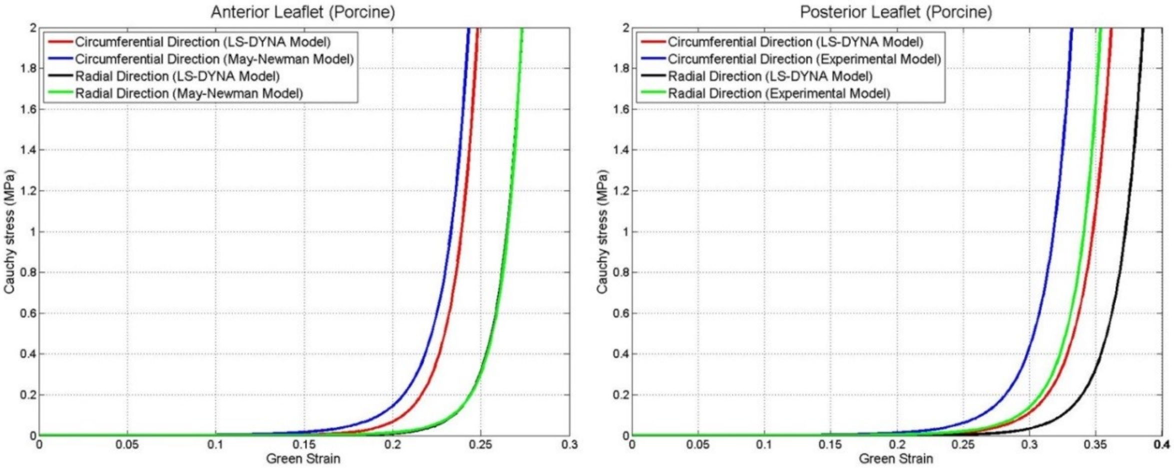

Figure 3.3: Results of simulated biaxial tensile tests run in LS-DYNA using the Guccione material constants calculated using MATLAB, and May-Newman and Yin's experimental results.

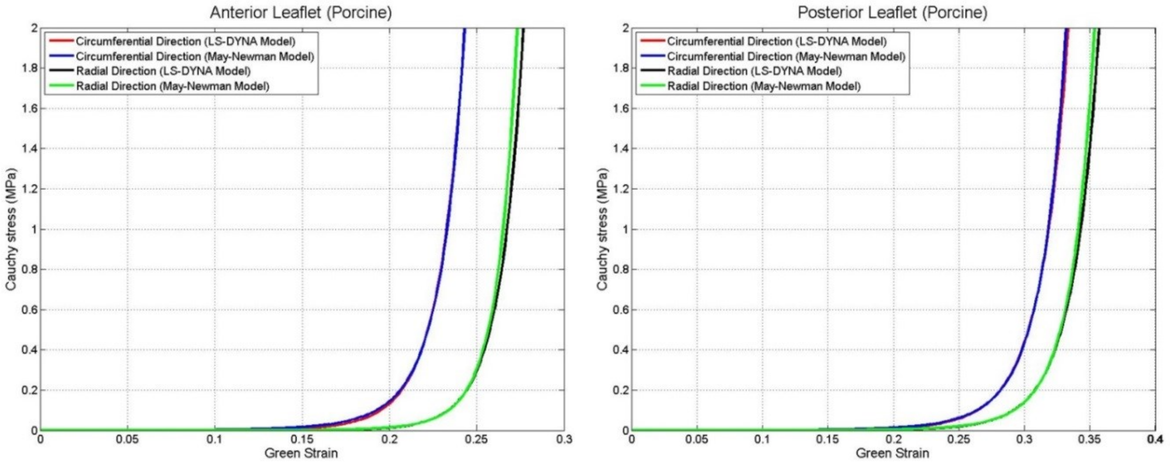

Figure 3.4: Mechanical behaviour of the anterior leaflet (left) and posterior leaflet (right) after optimization of the Guccione material constants to match the experimental results of May-Newman and Yin using simulated biaxial tensile testing in LS-DYNA.

Unfortunately, only three of the five material constants required for the material model that was implemented in LS-DYNA (MAT_HEART_TISSUE) could be calculated from the biaxial tensile test data. However, as long as the two remaining material constants—b_3, and the Lagrange multiplier p—were above certain threshold values (approximately 1 and 100, respectively), they did not affect the results of the simulated biaxial tests. To ensure accurate results, the values of the material constants b_3 and p were set to 10 and 200 respectively for all of the simulated biaxial tests. These values were selected since they were large enough to provide consistently accurate results, and also small enough to ensure that the simulations could be completed relatively quickly. The optimized material constants calculated to match May-Newman and Yin's experimental results on porcine mitral leaflet samples [51] are presented in Table 1.

Table 1: Optimized Guccione model material constants to match May-Newman and Yin's porcine material model [51].

Material Constant	Anterior Leaflet	Posterior Leaflet
c (MPa)	1.462726×10^{-5}	2.748355×10^{-5}
b_1	125.30375	54.599100
b_2	9.841921	15.378973

3.1.5. Simulated Pressure Test

Based on the results of the simulated biaxial tests, an initial simulation was run on the entire mitral valve apparatus using the material constants calculated from the biaxial test simulations, and the assumed values of 10 and 200 for b_3 and p, respectively. Unfortunately, it quickly became apparent that while these assumed values were acceptable for the biaxial simulations, they were not suitable for the full mitral valve simulations. Further simulations were then performed, and it was determined that changing the constant b_3 had a negligible effect on the results (suggesting that the shear stresses are negligible). However, the Lagrange multiplier p, which is related to the hydrostatic pressure of the tissue, needed to be several orders of magnitude larger to produce reasonable results. This result was somewhat unexpected, as Bonet and Wood suggested that a value of p in the range of $10^3 - 10^4$ times c generally yields acceptable results [37].

To the best of my knowledge, no effort has been made to determine the value of this Lagrange multiplier, and instead a large value was assumed for p (often in or near the range suggested by Bonet and Wood) [41], [52], [68], [69]. While this assumption has proven to be capable of producing acceptable results, it is not ideal. From my simulations on the mitral apparatus, it became apparent that changes in the value of p had a significant impact on the time required to complete the simulations, as well as the accuracy of the results. If the value selected for p was too small, the simulation would fail or produce unacceptable results. However, if an excessively large value of p was utilized, the simulation required significantly more time to run, and the tissues were far less compliant. Depending on the mesh density, these simulations required hours to days to complete. Therefore, for practical purposes, it was essential to minimize the value of the Lagrange multiplier, p, to help minimize the simulation's runtime. Since a very small value of p could be implemented for the biaxial tests, the Lagrange multiplier appeared to be necessary to support the pressure load acting on the ventricular surface of the leaflets. To test this hypothesis, a MATLAB program was designed to test the effect of applying a pressure load to one side of a square section of a mitral leaflet. The first iteration of this program was very similar to the program used to perform the simulated biaxial tests in LS-DYNA. However, instead of applying a displacement along two edges of the leaflet specimen, all of the perimeter nodes were constrained to prevent any displacement. The simulated ventricular pressure curve was applied to the bottom surface of the square specimen. For this simulation, the material constants c, b_1, b_2, and b_3 were set equal to the values found using the biaxial test simulations, and the Lagrange multiplier, p, was optimized. As with the biaxial simulation program, the mesh density and leaflet dimensions could be adjusted. Since the mitral leaflets are assumed to be nearly incompressible, and there was no available inflation test data, the error was defined at each state as the average elemental change in volume. Unfortunately, this test method did not converge on a value of p and MATLAB's lsqnonlin function could not be used. Instead, a minimum value of p was selected ($10^4 - 10^5$ depending on the type of tissue) which was then increased by small increments 20 – 30 times. For each value of p, the maximum and average percent volume changes were calculated and graphed. From these graphs, a general trend became quite obvious. When p was too small, the error was very large, and would decrease rapidly (roughly exponential decay). In some instances, the percent volume change would reach a minimum, before beginning to increase again (Figure 3.5). In such instances, the p value associated with this minimum was selected. However, depending on the tissue type (i.e. the material constants), in other instances the error would either stabilize and remain roughly constant for increasing p values beyond a certain point, or the error would continue to decrease (roughly linear) but at a very slow rate. In both of these cases, the p value that roughly corresponded with the end of the exponential decrease was selected. The thickness of the leaflet specimens was also found to affect the results, with thinner leaflets requiring a larger p value. However, once the specimens surpassed a thickness of 1 mm, the calculated p value tended to remain roughly constant. Several trials were also performed with different b_3 values, but any changes in the results were negligible.

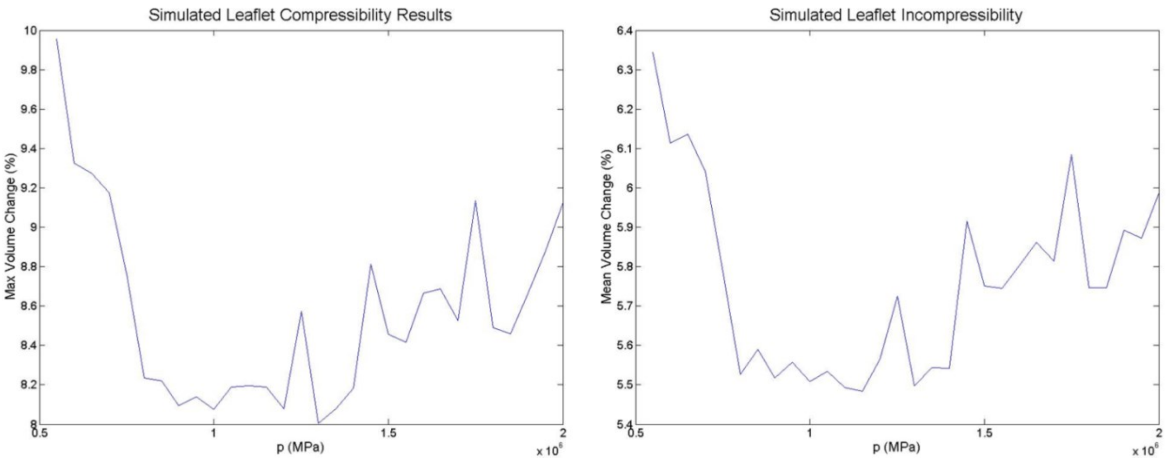

Figure 3.5: Maximum (left) and mean (right) volume change results from the simulated pressure test on a sample of anterior porcine leaflet with a thickness of 1 mm.

Based on the results of the simulated pressure tests it was determined that *p* values ranging from $3x10^5$ – $7x10^5$ MPa and $2x10^5$ – $1.8x10^6$ MPa were required for the porcine anterior and posterior leaflets, respectively. These simulations were also performed using diseased human leaflet material properties, which were found to require smaller *p* values (ranging from $4x10^4$ – $4.5x10^5$ MPa and $1.1x10^5$ – $3.6x10^5$ MPa for the anterior and posterior leaflets, respectively).

3.2. Chordae Tendineae Material Properties

The chordae tendineae are roughly circular in cross-section and comprised of the same basic materials as the mitral leaflets—collagen, elastin, and endothelial cells. Consequently, the chordae also exhibit highly non-linear stress-strain behaviour. The outermost layer of the chordae, the endothelium, is comprised of a thin layer of endothelial cells. The following two layers are also quite thin, and are composed of elastin fibres. The outer layer of elastin fibres are arranged in a mesh pattern, while the elastin fibres of the inner layer are aligned parallel to the longitudinal axis of the chordae tendineae [70].

Finally, the core of the chordae is mainly composed of collagen fibres, with some elastin fibres interspersed, both of which are aligned with the longitudinal axis (Figure 3.6) [70].

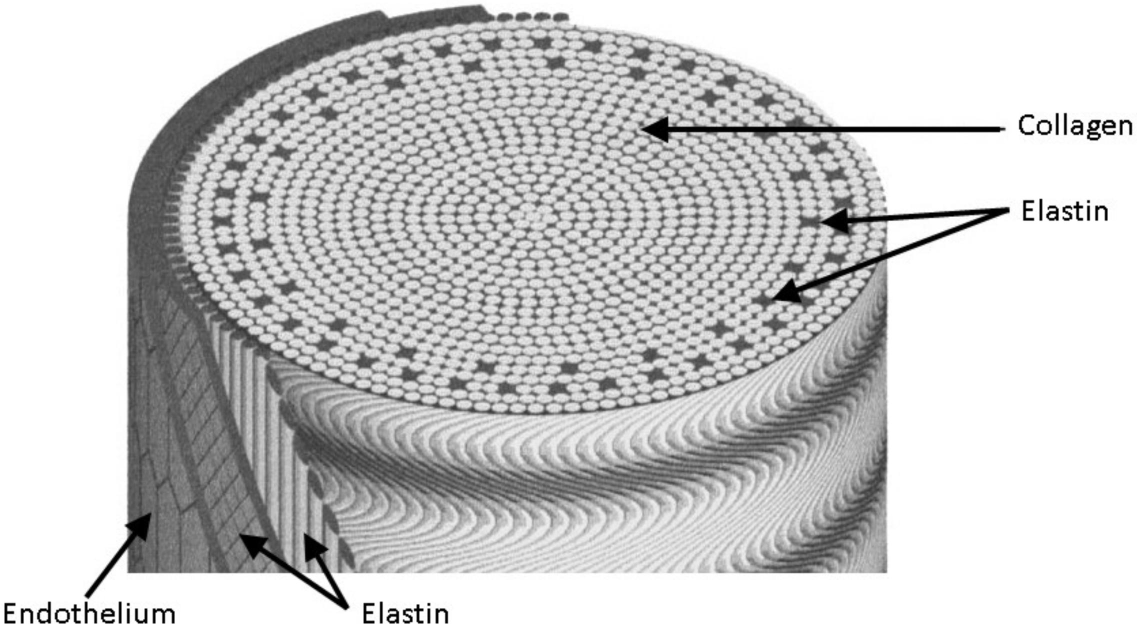

Figure 3.6: Schematic diagram showing the structure of the chordae tendineae (modified from [70])

As with the leaflet tissues, it is the undulating collagen fibres that are responsible for the non-linear mechanical behaviour of the chordae. When loaded, the collagen fibres begin to straighten, resulting in large deformations under small applied loads. However, as the collagen fibres begin to straighten out, the chordae become much stiffer and begin to exhibit roughly linear behaviour. As was previously mentioned, under normal physiological conditions, the chordae only experience loading in one direction—along the longitudinal axis. Therefore, unlike the leaflets' tissues, uniaxial tensile tests are suitable for determining the mechanical behaviour of the chordae tendineae. The stress-strain curve resulting from these uniaxial tests can be divided into three separate regions: the toe region, a linear region, and the failure region. The toe region is highly non-linear, and represents the alignment of the collagen fibres in the direction of the applied stress. As the collagen fibres straighten out, the chordae's stress-strain behaviour becomes roughly linear. Finally, under excessive loads the individual fibres begin to rupture. Unlike the majority of studies examining the mechanical behaviour of the mitral leaflets' tissues, studies that have focused on the mechanical behaviour of the chordae have not focused on trying to develop a strain energy equation to model the mechanical behaviour. Instead, these studies tend to focus on the modulus of the linear region, as well as the secant modulus of the toe region [71], [72].

In 2012, Casado *et al.* performed uniaxial tensile tests on 29 healthy marginal chordae and 9 moderately calcified marginal chordae from excised human mitral valves [72]. For each sample, an average diameter, secant modulus, and elastic modulus was calculated. The secant modulus was calculated using the origin of the stress-strain curve and the point at the end of the toe region (point A, Figure 3.7), while the elastic modulus was calculated using the point at the end of the toe region (point A, Figure 3.7), and the onset of the failure region (point B, Figure 3.7). In their study, Casado *et al.* found that the healthy marginal chordae had a mean diameter and secant modulus of 0.67 ± 0.23 mm and 2.03 ± 1.73 MPa, respectively. Relevant results from this study are presented in Table 2.

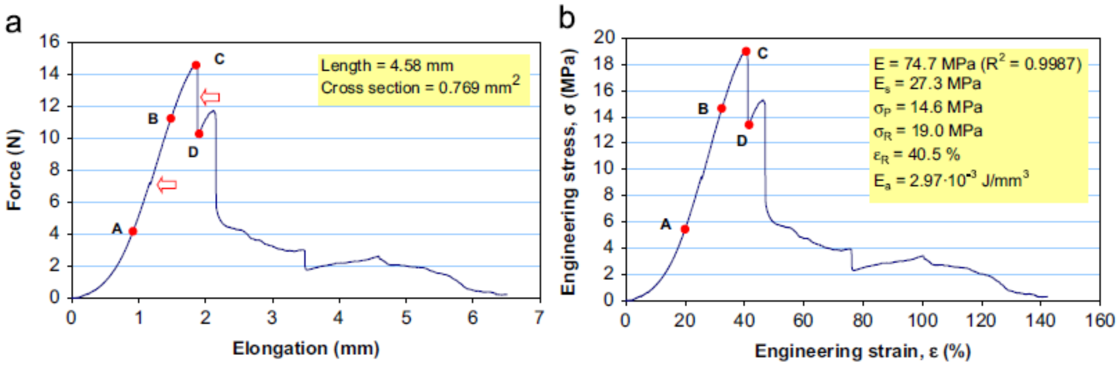

Figure 3.7: Typical mechanical behaviour of one marginal chordae tendineae showing the relevant features: (a) force vs. elongation; (b) stress vs. strain [72].

Table 2: Summary of relevant results from Casado *et al.*'s study on human marginal chordae tendineae [72].

	Healthy Marginal Chordae	Moderately Calcified Marginal Chordae
E (mean ± SD)	233 ± 189 MPa	43 ± 49 MPa
E_S (mean ± SD)	2.03 ± 1.73 MPa	0.23 ± 0.26 MPa
Diameter (mean ± SD)	0.67 ± 0.23 mm	3.6 ± 2.0 mm
Length (mean ± SD)	11 ± 4 mm	7.6 ± 2.5 mm

Another study by Ritchie *et al.* determined that under normal, physiological conditions the chordae function in a very narrow region (between A and B in Figure 3.8) [71]. Based on the information provided by Casado *et al.*, a simplified engineering stress-strain curve was generated using three separate linear regions (Figure 3.9a). However, based on the results from Ritchie *et al.*'s study, the stress-strain curve was shifted by 3.5% strain to the left to better match the normal physiological behaviour of the chordae tendineae (Figure 3.9b). This stress-strain curve was then included in the finite element model of the chordae, which employs a simple cable-like beam element in LS-DYNA (MAT_CABLE_DISCRETE_BEAM). This material model was selected since it does not support compressive loads.

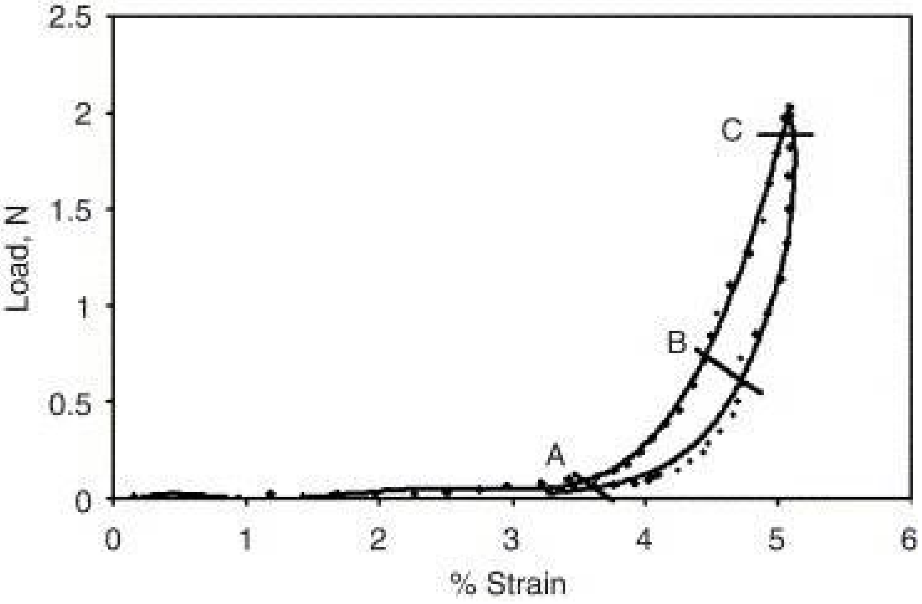

Figure 3.8: Uniaxial data for loading and unloading curves of the chordae tendineae. The physiological range in which the chordae normally function is between A and B [71].

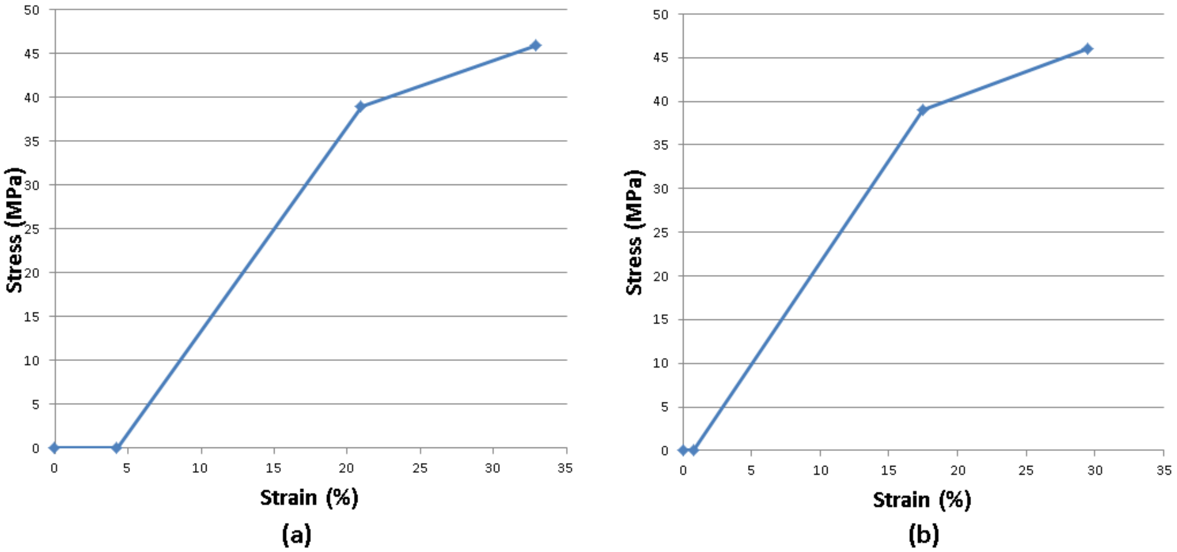

Figure 3.9: Simplified stress-strain curve created using data from Casado *et al.*'s study on healthy, human marginal chordae (a) and a stress-strain graph with a truncated toe region to better match normal physiological conditions.

Chapter 4

4. Finite Element Modeling of the Mitral Valve

There are three general modeling aspects that are essential to the generation of accurate, patient-specific models of the mitral valve: geometric reconstruction of the mitral apparatus, material modeling, and the simulation of physiological conditions. While the calculation and implementation of the material models employed for the mitral leaflets and chordae tendineae were previously covered in Chapter 3, this chapter focuses on the remaining two aspects of FE model generation—geometric reconstruction, and the simulation of physiological conditions.

4.1. Ultrasound Image Acquisition

As was previously discussed in Section 1.4, 4D TEE was used to obtain 3D images of healthy mitral valves. The data collection protocol was approved by the Ottawa Health Science Network Research Ethics Board (Appendix D). Furthermore, since this is a routine procedure in the diagnosis of mitral valve disease, and the data was completely de-identified, informed consent was waived. All of the datasets that were used in this study were collected by Dr. Sohmer, an anesthesiologist and echocardiographer at the University of Ottawa Heart Institute. In order to accurately model the entire mitral apparatus, it was essential that the entire annulus, both mitral leaflets, and the papillary muscles be visible in the dataset. To work with the raw mitral valve datasets provided by the University of Ottawa Heart Institute, a custom mitral valve quantification (MVQ) program was developed in MATLAB. This MVQ program was used to process the raw 4D ultrasound images, and recreate the geometry of the mitral apparatus as explained in the following sections. It should be noted that this MVQ program is different from the commercially available Mitral Valve Quantification (MVQ) software sold by Philips as an add-on to their QLab quantification software.

4.2. Ultrasound Image Processing

The raw ultrasound datasets obtained from the Heart Institute, which cover roughly one heartbeat, are first opened using the MVQ program and converted from a proprietary DICOM file to a MAT file. The 3D image is then displayed on the main screen as a montage of 2D short axis view images (Figure 4.1). If necessary, the time should be adjusted to ensure that the displayed images depict the valve at, or as close to, end-diastole as possible. Next, one image that depicts a slice of the left atrium, and one slice that depicts a slice of the left ventricle are selected (Figure 4.1). The centre of the mitral valve in each image is then defined by using a circle to approximate the atrial and ventricular walls (Figure 4.2). These two centre points are then used to define a local (Cartesian) coordinate system, with the vertical axis passing through the centre of the mitral orifice.

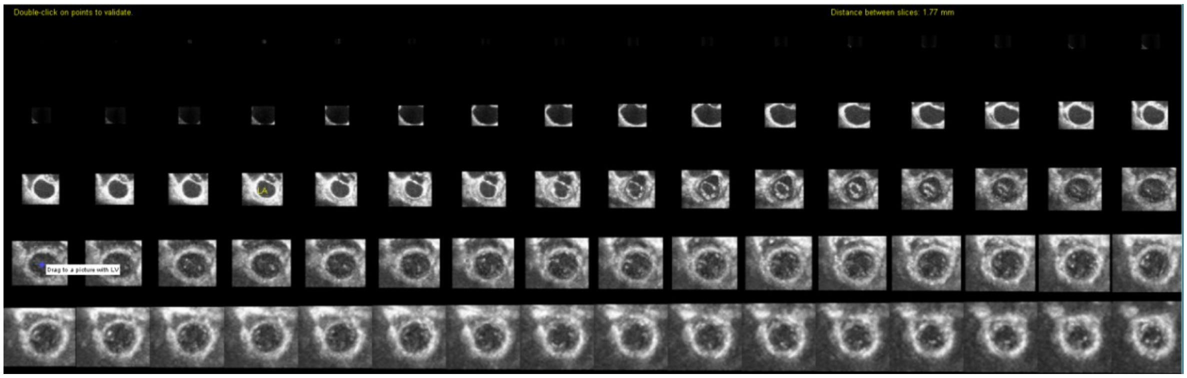
Double-click on points to validate.

Distance between slices: 1.77 mm

Drag to a picture with LV

Figure 4.1: Screen shot of the 2D short axis view montage of the mitral valve in MVQ. A slice with the left atrium has already been selected (marked by the yellow "LA" text on the image).

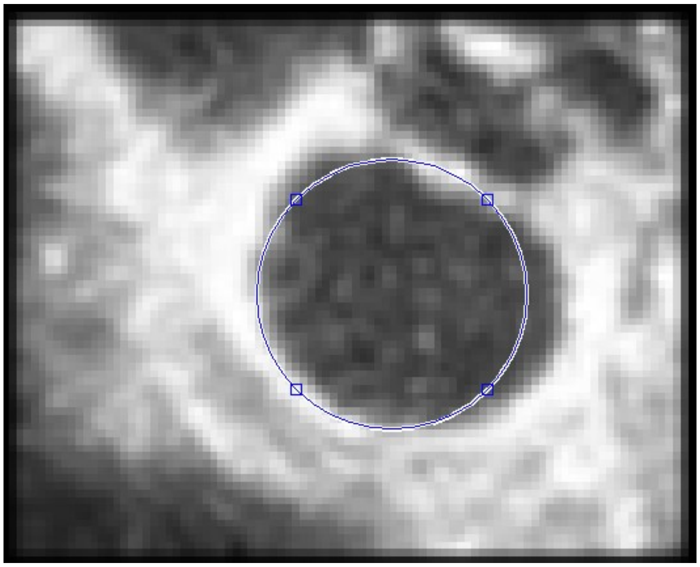

Figure 4.2: Centring of the left atrium in MVQ.

Once the new coordinate system has been generated, the montage of 2D, short axis view images is displayed again, but this time a circle is overlaid on each image, with the centre of each circle depicting the vertical axis of the new coordinate system (Figure 4.3). If an error was made when defining the local coordinate system, the user can restart the centring process. However, if the new coordinate system meets expectations they can continue on to the next step. It is important to note that beyond this point only the new, user-defined, local coordinate system will be used.

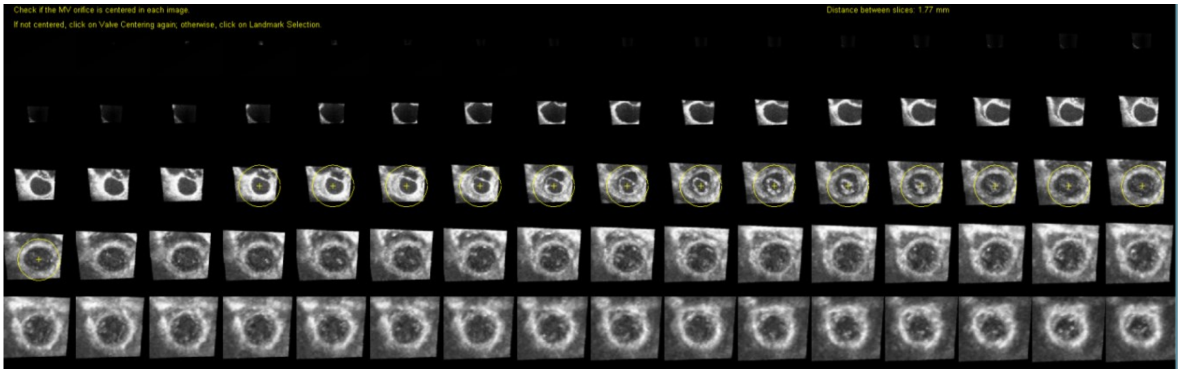

Check if the MV orifice is centered in each image.

If not centered, click on Valve Centering again; otherwise, click on Landmark Selection.

Distance between slices: 1.77 mm

Figure 4.3: 2D short axis view montage after centring the mitral valve. The cross at the centre of each yellow circle depicts the location of the new vertical axis.

On the next screen the user is presented with three perpendicular, cross-sectional slices—two long axis views, and one short axis view (Figure 4.4). The three coloured sliders can be used to further examine the mitral valve by adjusting the cross-sectional views. The time can also be adjusted using the black slider to examine the mitral valve's behaviour throughout the heartbeat. Here it is essential that the time slider is adjusted to coincide with end-diastole (the last frame where the MV is still fully open), as this time will be saved for the rest of the data acquisition process. It is also important to rotate the valve so that the red plane is parallel with the anteroposterior plane to ensure that the two commissures are properly detected during valve reconstruction. Once the valve has been positioned properly and the proper time frame has been selected, the user can click the "Proceed/Grab" button to proceed to the next screen.

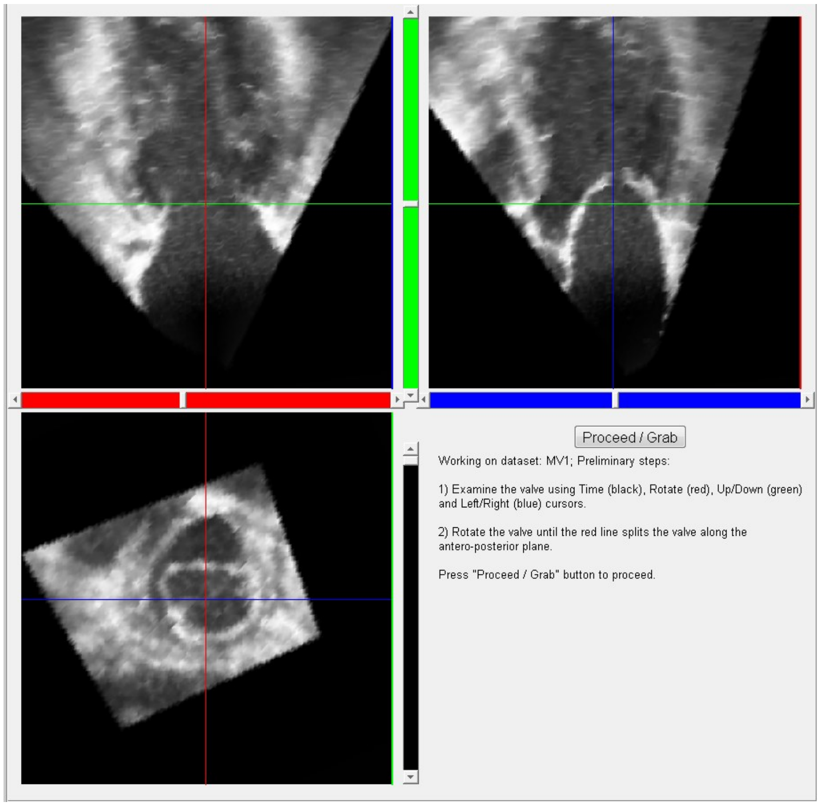

Working on dataset: MV1; Preliminary steps:

1) Examine the valve using Time (black), Rotate (red), Up/Down (green) and Left/Right (blue) cursors.

2) Rotate the valve until the red line splits the valve along the antero-posterior plane.

Press "Proceed / Grab" button to proceed.

Figure 4.4: Three cross-sectional views of the mitral valve. The sliders are used to select the correct timeframe and mitral positioning for data collection.

The final image processing step in MVQ involves filtering to help improve the ultrasound image quality, and facilitate the data acquisition process that follows. This screen shows three different images of a long axis view of the mitral valve (Figure 4.5). The first image, in the upper left corner, shows the original ultrasound image, while the second image (upper right) shows the ultrasound image after it has been filtered using a band-pass Butterworth filter. The final image (lower left) shows the filtered image after a mask has been applied to remove any pixels below the user-defined intensity threshold. Once again, the position of the mitral cross-sectional images can be rotated (using the red slider), but this is only intended to help with the selection of the amount of filtering required, and any changes to the position of the valve will not be saved. The three remaining sliders can be used to adjust the intensity threshold for the mask (green slider), and the low- and high-pass frequencies (blue and black sliders, respectively) of the Butterworth filter. Once the image filtering has been optimized, the user can press the “Proceed/Grab” button. This ends the image processing portion of the MVQ program, which is followed by the data selection portion of the program.

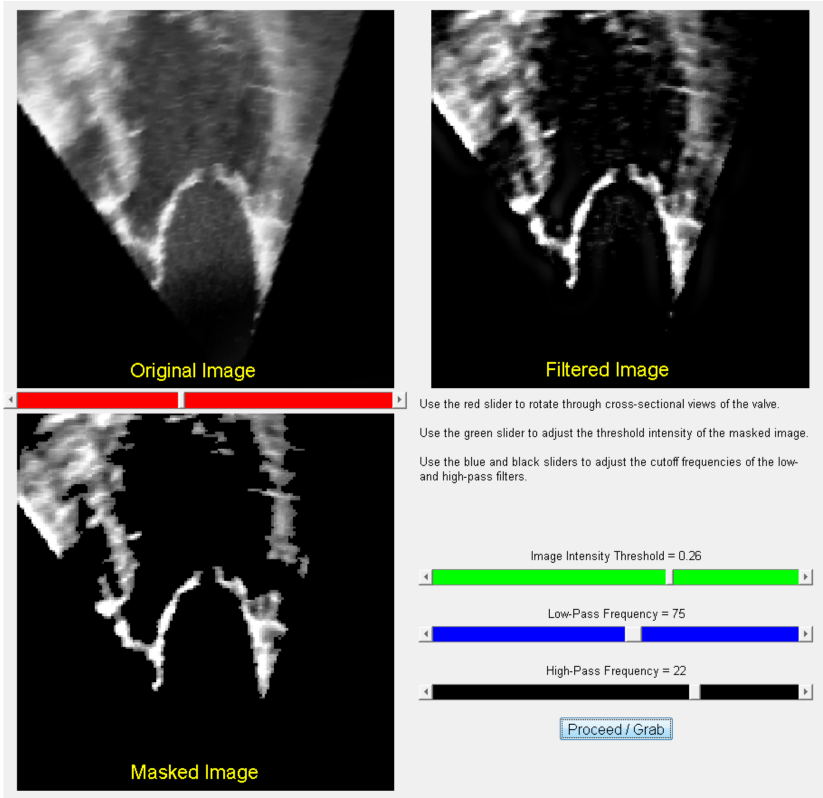

Use the red slider to rotate through cross-sectional views of the valve.

Use the green slider to adjust the threshold intensity of the masked image.

Use the blue and black sliders to adjust the cutoff frequencies of the low- and high-pass filters.

Image Intensity Threshold = 0.26

Low-Pass Frequency = 75

High-Pass Frequency = 22

Figure 4.5: Filtering of the ultrasound images in MVQ.

4.3. Geometric Data Selection

4.3.1. Leaflet Data Selection

To collect the necessary data to recreate the geometry of the mitral leaflets, the 3D ultrasound image is divided into 18 cross-sectional slices that are spaced at 10° intervals about the vertical axis. The following process is used to extract the geometry of the mitral leaflets manually from each image, which is then used to generate a 3D model of the valve.

Unfortunately, the limited resolution and relatively low SNR inherent to ultrasound images can be problematic when trying to identify the mitral leaflets. While the filtering performed in the previous step can be very helpful, the valve can be difficult to identify in certain cross-sectional images. Therefore, for each cross-sectional image, before identifying the leaflet geometry, the user is presented with a filtered and masked cross-sectional image (Figure 4.6). To help with the identification of the leaflets, a short axis cross-sectional view is inset in the lower left corner, which can be adjusted using the green slider along the left side of the window. A black slider is also present at the bottom of the window which can be used to adjust the timeframe. Through my experience, I found that adjusting the time and the location of the short axis view can be very helpful in identifying the annulus and free margin of the leaflets, especially when a significant amount of noise remains after filtering. Although the timeframe can be adjusted, it is important to note that this is only intended to help with the identification of the leaflets. Therefore, when the user moves on to the leaflet identification stage, the image will automatically revert to the timeframe associated with end-diastole.

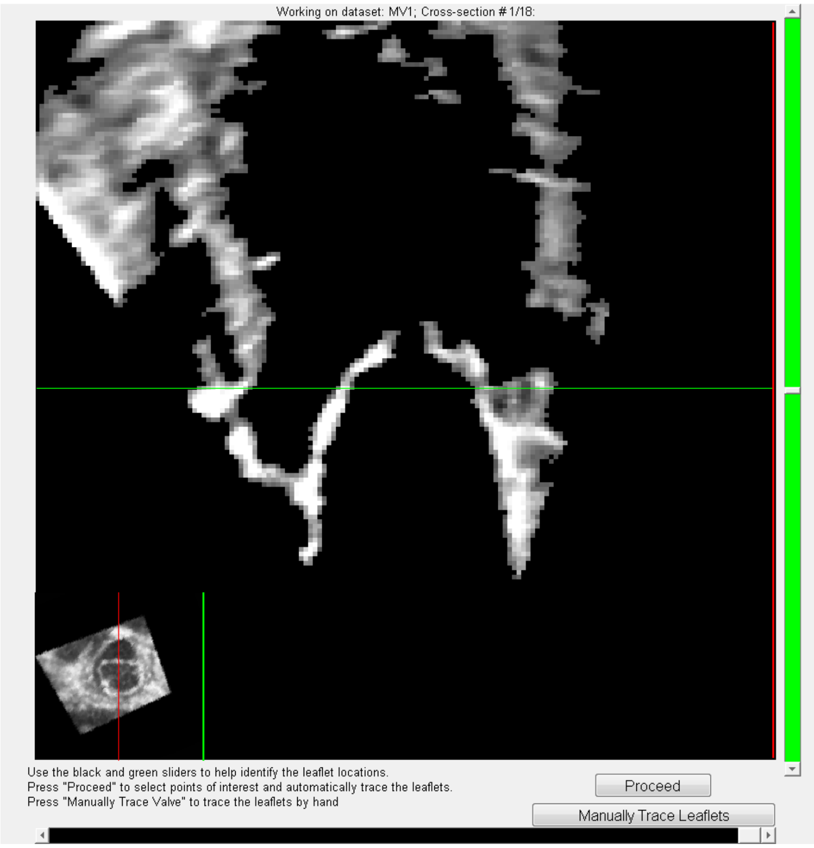

Working on dataset: MV1; Cross-section # 1/18:

Use the black and green sliders to help identify the leaflet locations.
Press "Proceed" to select points of interest and automatically trace the leaflets.
Press "Manually Trace Valve" to trace the leaflets by hand

Figure 4.6: Filtered and masked cross-sectional image of the mitral valve. The green and black sliders can be used to help identify the leaflet by adjusting the location of the inset short axis view and time frame, respectively.

There are two methods available to the user to collect the necessary geometric data. If the user selects the "Proceed" button, the masked and filtered image is converted to a binary image, allowing for a semi-automated leaflet edge detection process to be employed. In this case, the user must drag eight points to coincide with the annulus and free margin on the atrial and ventricular sides of each leaflet. The process starts by dragging the first point to the ventricular side of the annulus for the left leaflet and double-clicking on the point. The MATLAB program then automatically detects the nearest edge of the binary image and the MATLAB function bwtraceboundary is used to automatically trace the binary image. The selected point is then marked with a red, hollow circle, and the nearest point detected on the edge is marked with a green circle (Figure 4.7). Next, the second point is dragged to the free margin on the ventricular surface of the left leaflet. Again, the nearest point along the boundary of the binary image is automatically detected, and all points on the leaflet boundary between the two selected points are saved in a matrix. These data points represent the ventricular surface of the left leaflet. A third point is then placed at the left leaflet's free margin on the atrial surface, and the nearest point on the leaflet boundary is automatically detected. Finally, a fourth point is placed on the atrial side of the left leaflet's annulus. Again, the nearest point on the leaflet's boundary is automatically detected, and all points between the two selected locations on the atrial side are saved in a separate matrix. The same process is then followed for the leaflet on the right side of the image, and the atrial and ventricular data points are saved in the corresponding matrices. The automatically detected atrial and ventricular surfaces of both leaflets are then displayed over the original, unfiltered ultrasound image allowing the user to examine the quality of edge detection before continuing to the next cross-section (Figure 4.9).

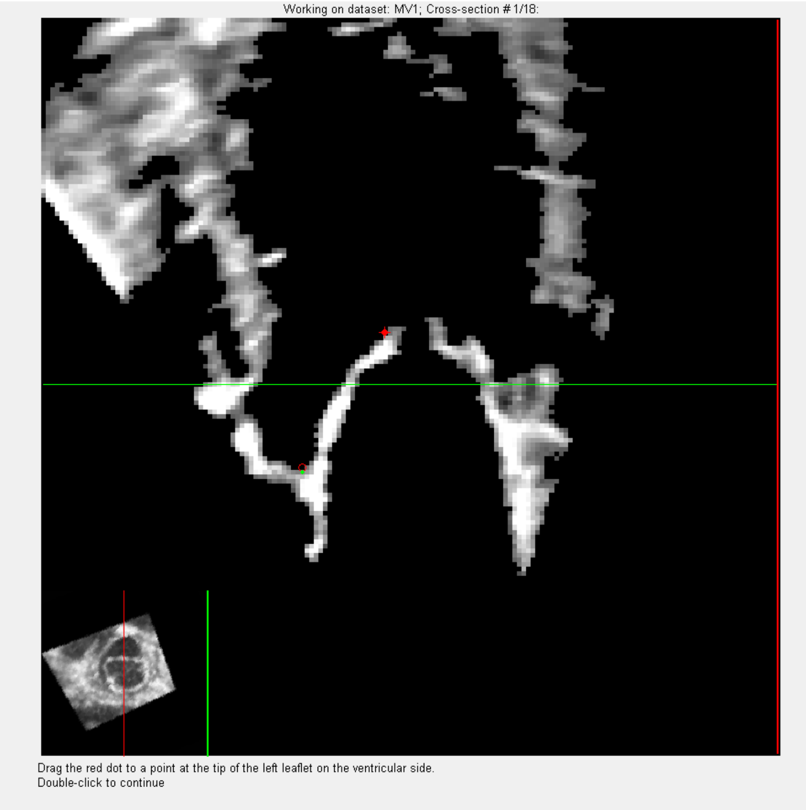

Working on dataset: MV1; Cross-section # 1/18:

Drag the red dot to a point at the tip of the left leaflet on the ventricular side.
Double-click to continue

Figure 4.7: The placement of points used for the automatic detection of the leaflets' boundaries.

If the user is unhappy with the results of the automatic edge detection program, or if it is apparent from the original filtered image that automatic edge detection will not work, there is the option to manually trace the atrial and ventricular surfaces of the two leaflets. In this case, the user is presented with a filtered, but unmasked, image. First the ventricular surface of the left leaflet should be traced, followed by the atrial surface. Next, the right leaflet can be traced, again starting with the ventricular surface, followed by the atrial surface. When the manual trace method is used, it does not matter whether the trace starts at the annulus or the free margin, but the four leaflet surfaces must be traced in the correct order. As was the case when the automatic edge detection method, the points along the manually traced surfaces are saved in the appropriate matrices. Before proceeding, the four leaflet surfaces are shown on the unfiltered ultrasound image (Figure 4.9).

Working on dataset: MV1; Cross-section # 1/18:

Trace the atrial surface of the left leaflet.
Press and hold the left mouse button to start freehand trace.
Release the left mouse button to finish tracing.

Figure 4.8: Manually traced ventricular surface of the left leaflet depicted by the blue line.

Working on dataset: MV1; Cross-section # 1/18:

Press "Proceed/Grab" to continue to the next cross-section.
Press "Redo" to reselect points of interest for the leaflets
Press "Manually Trace Valve" to trace the leaflets by hand

Figure 4.9: The blue lines depict the saved leaflet surface data points used for valve reconstruction.

4.3.2. Papillary Muscle Tips

After identifying the leaflet surfaces in the 18 cross-sectional images, the papillary muscles must be identified. The user is first presented with a screen that shows the three cross-sectional views of the valve as in Figure 4.4. Using the three coloured sliders, the cross-sectional images can be adjusted to help identify the location of the papillary muscles. Once the first papillary muscle has been identified, the height of the short axis view must be adjusted to ensure that the tip of the papillary muscle is visible in this cross-section. After pressing the "Proceed/Grab" button, the MVQ program proceeds to a new screen that displays this short axis view of the mitral valve. The user can then manually trace the papillary muscle tip and the data points are saved in a matrix. This same process is then repeated for the second papillary muscle, and the data points are added to the papillary muscle tip matrix. Finally, the user is presented with two options: they can retrace both papillary muscle tips, or they can continue. Selecting "Save & Exit" ends the MVQ program, and all of the relevant data is saved to a MATLAB file that will be used to generate a 3D model of the mitral valve.

4.4. Geometric Reconstruction of the Mitral Valve

After acquiring the geometric coordinates of the atrial and ventricular surfaces of the leaflets, and the papillary muscle tips the data must be processed to generate a finite element model of the mitral apparatus. A processing program, named MVSim, was created in MATLAB that is used to generate an LS-DYNA input file. Using the MATLAB data file that was created by the MVQ program, the mitral geometry is processed to create a finite element model and the relevant material properties are assigned to the mitral leaflets and chordae tendineae.

4.4.1. MVSim User Interface

Before going into the details of how the MVSim uses the geometric data from the MVQ program to generate a finite element model of the mitral apparatus, it is beneficial to briefly cover MVSim's user interface. In order to improve the robustness of the MVSim program, a variety of options are available to the user that are intended to help improve the accuracy of the finite element simulations. After loading the data file that was generated using the MVQ program, the user must select the appropriate material properties, the mesh density for the mitral leaflets, and the amount of smoothing applied to the leaflets. Currently there are five material properties options for each mitral leaflet, and two for the chordae tendineae. The leaflet properties were gathered from two separate studies—May-Newman and Yin's study on porcine mitral leaflets [51], and Pham and Sun's study of aged human mitral leaflets [53]—and the Guccione constants (required for the LS-DYNA material model MAT_HEART_TISSUE) were calculated using the procedure outlined in Section 3.1. Based on Pham and Sun's observations, the aged human mitral leaflet results were separated into four separate categories for each leaflet depending on the observed calcification level, and the patient's blood pressure (hypertensive or normotensive). Since this study only examined healthy mitral valve datasets only the porcine material model was implemented since it is the closest available model for healthy human mitral leaflet tissue. The two chordae material models available, healthy and calcified, both come from Casado *et al.*'s study on human marginal chordae tendineae [72]. Again, since this study only examined healthy datasets, the calcified human chordae tendineae material model was not implemented. Although these material models were not implemented in any of the finite element models in this study, they were included to help facilitate the transition to simulating diseased mitral valves in the future.

The next step in the MVSim program is to select the mesh density for the finite element model. Here, the mesh density is defined by three fields: the number of elements in the radial, circumferential, and thickness directions. The mesh in the circumferential direction is generated by interpolating points between two adjacent leaflet profiles. Since the leaflet surfaces were defined in 18 slices, with each cross-section containing two leaflets, there is a total of 36 leaflet profiles that are used to generate the mesh, each spaced 10° apart. As a result, the number of elements in the circumferential direction can only be increased in increments of 36. While any (non-zero, positive) number of elements can be used in the radial and thickness directions, the number of options were limited for practical purposes. In the radial direction, a minimum number of 10 elements can be selected which can be increased in increments of two up to a maximum of 20 elements. A minimum of 10 elements was selected to prevent excessively large elements, and a maximum of 20 elements was chosen to prevent excessively long simulation runtimes. In the thickness direction, the user can select between two or three elements. Increasing the number of elements above three in this direction is not feasible since the simulation would take days to weeks (depending on the mesh density in the other two directions) to complete.

Finally, the user can use two sliders to apply some smoothing to the finite element model in the radial directions. By using a weighted averaging algorithm (refer to Equation (4.20)) the leaflets' profile can be smoothed in the radial and circumferential directions. Since the smoothing process will reduce the accuracy of certain features like the annulus, free margin, and commissures, the amount of smoothing applied to the leaflets should kept to a minimum. After selecting the amount of smoothing to apply to the mitral model, the accuracy of the final model can be examined by displaying the generated leaflet surfaces on top of the original 3D ultrasound image.

4.4.2. Leaflet Mesh Generation

Since the leaflet geometry data is collected using the local, cylindrical coordinate system (r, z, θ), it was easiest to save these data points in cylindrical coordinates. However, for the purpose of generating the mesh required for the finite element model, it is easiest to convert these data points to a unique Cartesian coordinate system (x, y, z). Scaling factors, f, are also applied when converting to Cartesian coordinates to match the valve's anatomical measurements. These scaling factors are provided in the ultrasound dataset, and allow for the unit conversion from pixels (or voxels in 3D) to mm. Typically, one voxel is approximately 0.6 x 0.6 x 0.5 mm in the x, y, and z directions, respectively.

$$x = r\cos(\theta) f_x \tag{4.1}$$

$$y = r\sin(\theta) f_y \tag{4.2}$$

$$z = z f_z \tag{4.3}$$

This conversion to a Cartesian coordinate system is the first step towards generating a finite element model of the mitral leaflets. The next step requires the generation of data points, or nodes, which will be used to define the leaflets, via individual eight-node brick elements in the finite element model. The rationale for modeling the leaflets using brick elements instead of shell elements is discussed in Section 4.4.4. Since the surfaces of the leaflets were defined in each cross-section, there are plenty of data points available in the radial direction. However, these slices were taken at 10° increments, so the resolution in the circumferential direction is limited. Using the available data points, Coons-patch interpolation was selected to extend the results of the image segmentation into a more complete 3D model. This method can be used to generate a mesh from the boundary contours of an enclosed area. Figure 4.10 depicts a linearly interpolated Coons-patch generated using the four boundary contours $\mathbf{c}_1(u)$, $\mathbf{c}_2(u)$, $\mathbf{d}_1(v)$, and $\mathbf{d}_2(v)$, $u, v \in [0,1]$. Since Coons-patch interpolation produces a surface $x(u,v)$ between the boundary contour segments, the interpolation of the leaflets' surfaces must be done patch-by-patch to generate a mesh between each leaflet cross-section. As a result, 72 Coons-patches must be created—36 for the atrial surface, and 36 for the ventricular surface of the leaflets.

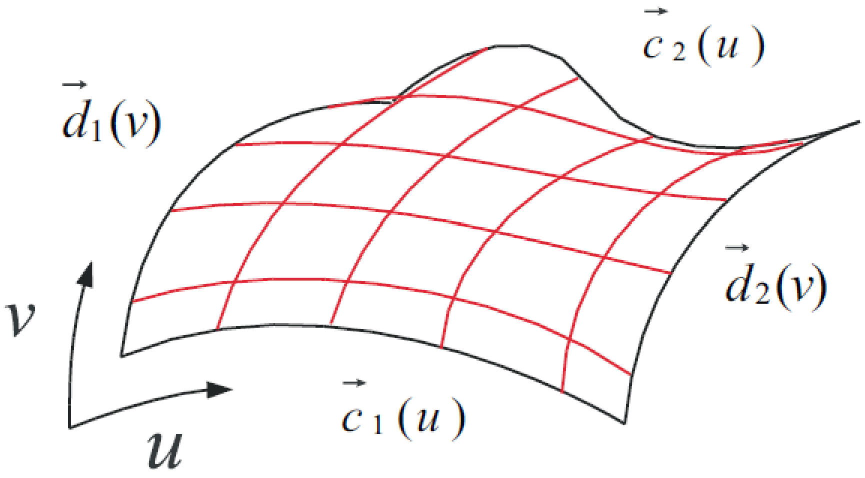

Figure 4.10: A linearly interpolated Coons-patch [73].

Assuming the same notation as Figure 4.10, the unit vectors u and v will be used to represent the circumferential and radial directions, respectively. Therefore, contours $\mathbf{c}_1(u)$ and $\mathbf{c}_2(u)$ represent sections of the annulus and free margin, respectively, while the contours $\mathbf{d}_1(v)$ and $\mathbf{d}_2(v)$ represent the cross-sectional slices of the leaflets. Unfortunately, linearly interpolated Coons-patches are treated completely separately from each other, leading to discontinuous first derivatives between patches [73]. However, if the interpolation is performed using the following cubic Hermite polynomials instead of linear interpolation, this is known as a bicubic Coons-patch, and no discontinuity exists between the adjacent patches.

$$H_0(t) = 2t^3 - 3t^2 + 1 \tag{4.4}$$

$$H_1(t) = t^3 - 2t^2 + t \tag{4.5}$$

$$H_2(t) = t^3 - t^2 \tag{4.6}$$

$$H_3(t) = -2t^3 + 3t^2 \tag{4.7}$$

The first step required to generate the Coons-patches is to develop the functions necessary to define the four boundary contours. Up until this point, the leaflet contours were only defined by individual data points along the atrial and ventricular surfaces. The best method to convert these data points to individual functions was determined to be through the use of cubic splines. Cubic splines are splines that are constructed of piecewise third-order polynomials which are calculated using a known set of data points. The cross-sections of the leaflets (contours $\mathbf{d}_1(v)$ and $\mathbf{d}_2(v)$) were defined using cubic B-splines, while the annulus and free margin were defined using natural cubic splines. B-splines were selected to model the leaflet cross-sections due to the large number of data points available for each cross-section. Since the B-spline does not have to pass through each individual data point, a small amount of smoothing is naturally included when this type of spline is employed. This is beneficial since the limited resolution of the ultrasound images resulted in slightly jagged contours. Using the spmak function in MATLAB, cubic B-splines were easily calculated from the known leaflet data points, and a set of user defined knots.

Since the B-splines are required for the proper implementation of bicubic Coons-patch interpolation, they must meet certain requirements. While B-splines do not have to pass through the data points, it is essential that the start and end of the B-splines match the first and last data points. Otherwise there will not be a closed boundary that can be used for the Coons-patch interpolation. Furthermore, the slope at the beginning and end of each spline must be known. Fortunately, these are both characteristics of clamped B-spline curves, which are defined by a specific knot sequence. First, the size of the knot vector (m) is related to the number of control points (n) and the order of the curve (k, where the degree of the polynomial = k-1) as follows:

$$m = n + k \tag{4.8}$$

Also, the first and last knot must be of the multiplicity k. Therefore, to generate a clamped, cubic B-spline the first four and last four knots must be identical. While the remaining knots can be anywhere in that domain, non-uniformly spaced knots will force the curve to move closer to or further from the related control point. This would only be helpful in forcing the spline to take a certain shape, therefore the following uniformly spaced knot sequences was used for all B-splines, where t_i is the i^{th} knot.

$$t_i = \begin{cases} 0, & i \leq k \\ i - k, & k < i \leq n \\ n - k + 1, & n < i \leq m \end{cases} \tag{4.9}$$

While the functions used to define the contours of the leaflet cross-sections only needed to pass through the two end points, the splines used to define the annulus and free margin needed to pass through the end points of all 36 cross-sections. As a result, B-splines could not be used. Instead, the MATLAB function cscvn was used to create natural cubic splines that passed through all 36 of the spline-defining points. This function is slightly easier to implement than the B-spline since it only requires the coordinates of the points that the spline passes through. Four natural cubic splines were created using this technique to model the atrial and ventricular edges of the free margin and annulus.

With the required boundary functions fully defined, bicubic Coons-patch interpolation could be implemented to generate the surface $x(u,v)$, from which the desired mesh can be obtained. By definition, the surface $x(u,v)$ between the contour segments must fulfill the following conditions:

$$\begin{aligned} x(u,0) &= c_1(u), \quad x(u,1) = c_2(u), \\ x(0,v) &= d_1(v), \quad x(1,v) = d_2(v). \end{aligned} \tag{4.10}$$

Therefore the first partial derivatives $x_n(u,v)$ with respect to $n \in \{u,v\}$ perpendicular to the boundaries of the patch can be interpolated from the known tangents at the end points ($u,v \in \{0,1\}$) of the contour segments as follows [73]:

$$\begin{aligned} x_u(0,v) &= x_u(0,0)H_0(v) + x_u(0,1)H_3(v) \\ x_u(1,v) &= x_u(1,0)H_0(v) + x_u(1,1)H_3(v) \\ x_v(u,0) &= x_v(0,0)H_0(u) + x_v(1,0)H_3(u) \\ x_v(u,1) &= x_v(0,1)H_0(u) + x_v(1,1)H_3(u) \end{aligned} \tag{4.11}$$

Next, this result is used to create the two temporary surfaces

$$\begin{aligned} h_c(u,v) &= x(0,v)H_0(u) + x_u(0,v)H_1(u) + x_u(1,v)H_2(u) + x_u(1,v)H_3(u) \\ h_d(u,v) &= x(u,0)H_0(v) + x_v(u,0)H_1(v) + x_v(u,1)H_2(v) + x_v(u,1)H_3(v) \end{aligned} \tag{4.12}$$

and the error surface

$$\begin{aligned} &h_{cd}(u,v) \\ &= \begin{bmatrix} H_0(u) & H_1(u) & H_2(u) & H_3(u) \end{bmatrix} \begin{bmatrix} x(0,0) & x_v(0,0) & x_v(0,1) & x(0,1) \\ x_u(0,0) & 0 & 0 & x_u(0,1) \\ x_u(1,0) & 0 & 0 & x_u(1,1) \\ x(1,0) & x_v(1,0) & x_v(1,1) & x(1,1) \end{bmatrix} \begin{bmatrix} H_0(v) \\ H_1(v) \\ H_2(v) \\ H_3(v) \end{bmatrix} \end{aligned} \tag{4.13}$$

These three surfaces are then combined to produce the bicubic Coons-patch

$$x(u,v) = h_c(u,v) + h_d(u,v) - h_{cd}(u,v) \tag{4.14}$$

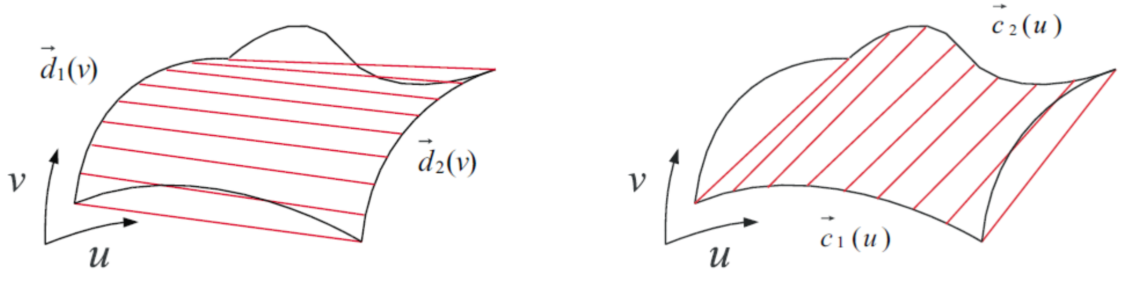

(a) temporary surface $\mathbf{r}_c(u,v)$ (b) temporary surface $\mathbf{r}_d(u,v)$

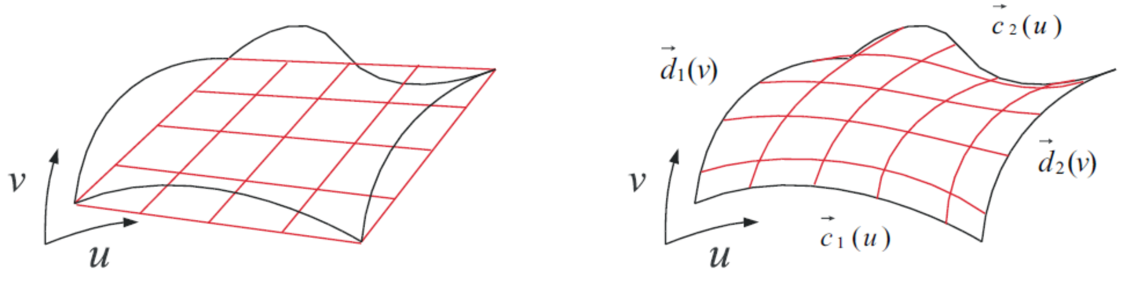

(c) *error-surface* $\mathbf{r}_{cd}(u,v)$ (d) linearly interpolated Coons-patch

Figure 4.11: Visual representation of the process used to calculate a Coons-patch. The linearly interpolated Coons-patch (d), is defined as the sum of the two temporary surfaces (a) and (b) minus the error-surface (c). The same process is employed for bicubic Coons-patch interpolation [73].

To generate a mesh of n by m nodes, the following vectors are substituted into Equation (4.14):

$$u = 0{:}\frac{1}{n-1}{:}1 \tag{4.15}$$

$$v = 0 : \frac{1}{m-1} : 1 \tag{4.16}$$

The constants m and n are calculated from the number of elements in the radial (M) and circumferential (N) directions, respectively, (as selected by the user in MVSim) as follows:

$$m = M + 1 \tag{4.17}$$

$$n = \frac{N}{36} + 1 \tag{4.18}$$

To remove any irregularities in the leaflets' atrial and ventricular surfaces, a small amount of smoothing is normally applied to the mesh. Any necessary smoothing is achieved using a weighted-average smoothing algorithm developed in MATLAB, which can be applied in the radial and circumferential directions. This technique ensures that the closest points have the largest impact on the calculated average which was found to be particularly helpful near the commissures where there is a rapid change in the leaflets' length. The amount of smoothing, s, is selected by the user and represents the number of nodes in each direction that will be considered in the smoothing algorithm.

$$p_{M,avg} = \frac{1}{(s+1)^2} \sum_{i=-s}^{s} (s + 1 - |i|) p_{M+i} \tag{4.19}$$

Here, p_M is a vector containing the x, y, and z coordinates of the point M, and $p_{M,avg}$ is a new vector containing the new x, y, and z coordinates for the same point after smoothing has been applied. Since the points representing the leaflet profile in the radial direction do not form a closed loop, this algorithm must be modified slightly. In this case, the points along the annulus and free margin are not smoothed to prevent the loss of information. For a dataset containing *n* data points that do not form a closed loop, the following smoothing algorithm was applied:

$$p_{M,avg} = \begin{cases} \dfrac{1}{M^2} \displaystyle\sum_{i=-(M-1)}^{2M-1} (M - |i|)\, p_{M+i}, & 2 \leq M \leq s \\ \dfrac{1}{(s+1)^2} \displaystyle\sum_{i=-s}^{s} (s + 1 - |i|) p_{M+i}, & s < M \leq n - s \\ \dfrac{1}{(n-M)^2} \displaystyle\sum_{i=-(n-M)}^{n-M} (n - M + 1 - |i|)\, p_{M+i}, & n - s < M < n \end{cases} \tag{4.20}$$

Again, p_M represents the M^{th} data point (with x, y, and z coordinates) in the dataset that is being smoothed. Finally, once the atrial and ventricular surfaces of the leaflets have been smoothed, linear interpolation is used to generate nodes between the two leaflet surfaces.

4.4.3. Definition of the Anterior and Posterior Leaflets

Up to this point, the two leaflets have been treated as a single entity which is defined by the mesh that was generated from the 18 cross-sectional slices of the mitral valve. However, the anterior and posterior leaflets do not have the same material properties. Therefore, to implement the two leaflet material properties, this mesh must be split into two groups; one set of nodes for the anterior leaflet, and a separate set of nodes for the posterior leaflet. The junction of the two leaflets is defined by the two commissures. Therefore, the commissures must first be identified before the leaflet nodes can be divided into two distinct groups.

The two commissures are defined as the two locations of the mitral valve with the shortest leaflet length in the radial direction. Generally, the posterior portion of the annulus comprises roughly two thirds of the annulus's total circumference, with the anterior portion forming the remaining third. Since the anteroposterior plane intersects the mid-point of both leaflets, there should be one commissure on each half of the valve when divided by this plane. Therefore, for commissure detection, the mesh is split into two equal groups (lateral and medial halves). To determine the leaflet lengths in the radial direction, the atrial and ventricular surfaces of the leaflet are defined using cubic splines for each set of nodes in the circumferential direction. The leaflet length at each circumferential position is then defined as the average length of the splines that are used to define the atrial and ventricular surfaces of the leaflets. The location of the shortest average leaflet length, on the lateral and medial sides of the valve, are then defined as the two commissures. The nodes that define the mitral leaflets are then split into two separate matrices—one for each leaflet.

4.4.4. Leaflet Element Generation

Having split the mitral valve into two distinct leaflets, the individual elements required for the finite element analysis can be defined. Both leaflets are modeled using hexahedral (brick) elements with eight nodes. Depending on the mesh selected by the user, one to three layers of elements are generated across the leaflet thickness. The material model (MAT_HEART_TISSUE) that is implemented in LS-DYNA requires the use of solid elements, therefore linear brick elements (ELEMENT_SOLID) are used, and the node numbering convention depicted in Figure 4.12 is implemented.

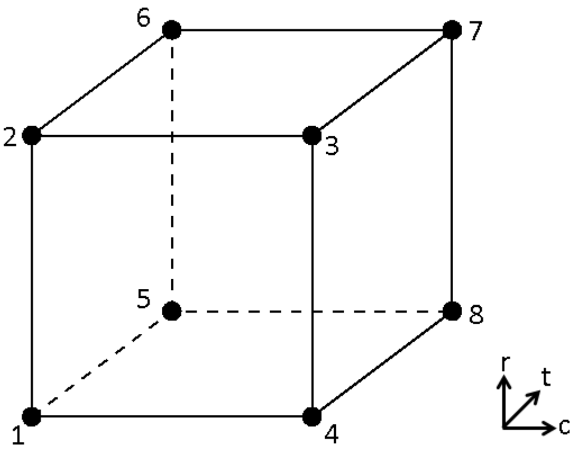

Figure 4.12: Node numbering convention for brick elements (r, c, and t are the radial, circumferential, and thickness directions, respectively)

Using this numbering convention, the leaflets are discretized into brick elements from the set of nodes used to define the anterior and posterior leaflets. The algorithm starts with the first node at the annulus of the ventricular surface of the anterior leaflet, and creates a row of elements in the radial direction (from the annulus to the free margin). The process continues in the circumferential direction until it reaches the other edge of the anterior leaflet, defined by the second commissure. If the user selected more than one element in the thickness direction, the algorithm follows the same procedure to generate the desired number of layers for the anterior leaflet. The same procedure is then followed to define the posterior leaflet's brick elements. The nodal data for each element is stored in a structure as follows:

$$E_x = \begin{bmatrix} N_1 \\ N_2 \\ N_3 \\ N_4 \\ N_5 \\ N_6 \\ N_7 \\ N_8 \end{bmatrix} = \begin{bmatrix} i + m[(j-1) + (k-1)N_A] \\ i + m[(j-1) + (k-1)N_A] + 1 \\ i + m[j + (k-1)N_A] + 1 \\ i + m[j + (k-1)N_A] \\ i + m[(j-1) + k * N_A] \\ i + m[(j-1) + k * N_A] + 1 \\ i + m[j + k * N_A] + 1 \\ i + m[j + k * N_A] \end{bmatrix}, \quad \begin{matrix} 1 \le i < m \\ 1 \le j < N_A \\ 1 \le k \le t \end{matrix} \tag{4.21}$$

$$E_x = \begin{bmatrix} N_1 \\ N_2 \\ N_3 \\ N_4 \\ N_5 \\ N_6 \\ N_7 \\ N_8 \end{bmatrix} = \begin{bmatrix} i + m(N_A - 1)k \\ i + m(N_A - 1)k + 1 \\ i + m[(k-1)N_P + N_A(t+1)] + 1 \\ i + m[(k-1)N_P + N_A(t+1)] \\ i + m[N_A(k+1) - 1] \\ i + m[N_A(k+1) - 1] + 1 \\ i + m[k * N_P + N_A(t+1)] + 1 \\ i + m[k * N_P + N_A(t+1)] \end{bmatrix}, \quad \begin{matrix} 1 \le i < m \\ 1 \le k \le t \end{matrix} \tag{4.22}$$

$$E_x = \begin{bmatrix} N_1 \\ N_2 \\ N_3 \\ N_4 \\ N_5 \\ N_6 \\ N_7 \\ N_8 \end{bmatrix} = \begin{bmatrix} i + m[(j-1) + (k-1)N_P + N_A(t+1)] \\ i + m[(j-1) + (k-1)N_P + N_A(t+1)] + 1 \\ i + m[j + (k-1)N_P + N_A(t+1)] + 1 \\ i + m[j + (k-1)N_P + N_A(t+1)] \\ i + m[(j-1) + k * N_P + N_A(t+1)] \\ i + m[(j-1) + k * N_P + N_A(t+1)] + 1 \\ i + m[j + k * N_P + N_A(t+1)] + 1 \\ i + m[j + k * N_P + N_A(t+1)] \end{bmatrix}, \quad \begin{matrix} 1 \le i < m \\ 1 \le j < N_P \\ 1 \le k \le t \end{matrix} \tag{4.23}$$

$$E_x = \begin{bmatrix} N_1 \\ N_2 \\ N_3 \\ N_4 \\ N_5 \\ N_6 \\ N_7 \\ N_8 \end{bmatrix} = \begin{bmatrix} i + m[k * N_P + N_A(t+1) - 1] \\ i + m[k * N_P + N_A(t+1) - 1] + 1 \\ i + m(k-1)N_A + 1 \\ i + m(k-1)N_A \\ i + m[N_P(k+1) + N_A(t+1) - 1] \\ i + m[N_P(k+1) + N_A(t+1) - 1] + 1 \\ i + k * m * N_A + 1 \\ i + k * m * N_A \end{bmatrix}, \quad \begin{matrix} 1 \le i < m \\ 1 \le k \le t \end{matrix} \tag{4.24}$$

Here x is the element number, m is the number of nodes in the radial direction, N_A and N_P are the number of nodes in the circumferential direction of the anterior and posterior leaflets, respectively, and t is the number of elements across the leaflets' thickness. The Equations (4.21) and (4.23) are used to generate the elements of the anterior and posterior leaflets, respectively, while the Equations (4.22) and (4.24) are required to generate elements between the nodes that represent the edges of the anterior and posterior leaflets. The element number, *x*, which starts at one, increases in increments of one for each subsequent element.

4.4.5. Chordae Tendineae Element Generation

Since the chordae tendineae are modeled using beam elements in LS-DYNA, each element only requires two nodes. However, midway between the papillary muscles and free margin, the chordae tendineae branch from one element into two elements. Furthermore, to better represent any bending of the chordae tendineae, each branch is composed of four beam elements. Therefore each chordae is composed of 13 nodes—one node at the papillary muscle (N_{PM}), two nodes on the leaflet's free margin ($N_{FM,1}$ and $N_{FM,2}$), one node midway between the free margin and papillary muscle (N_B), and three additional nodes per branch (Figure 4.13).

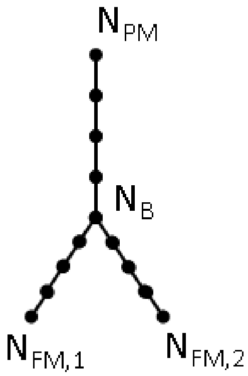

Figure 4.13: Schematic of a chordae tendineae with nodes.

On average, approximately 12 chordae tendineae originate from each papillary muscle in humans [74], [75]. Since the papillary muscles serve as anchor points for the chordae, 12 nodes were generated along each papillary muscle—one per chordae origin. Furthermore, one study that examined the chordae tendineae in human cadaveric hearts found that the mean number of marginal chordae per leaflet is 22.63 [75]. To simplify the model, this number was rounded up to 24, allowing each chordae to split into two branches before inserting into the free margin of the leaflets. To obtain the nodes required for the papillary muscles, two cubic splines were generated using the data points collected in the MVQ program. The coordinates of 12 equidistant points were then obtained from each spline, and stored as the papillary muscle nodes. Next, the chordae insertion points along the free margin of the leaflets needed to be calculated. Since real chordae attach across the thickness of the leaflet, the chordae were attached at mid-thickness of the free margin to better approximate the *in vivo* attachment. Having already located the two commissures and separated the two leaflets into two separate datasets, calculating the insertion points along the free margin is fairly straightforward. The numbers of nodes in the circumferential direction of the anterior and posterior leaflets were already determined to be N_A and N_P, respectively, and the chordae were assumed to be spaced equally along the free margin. Since these nodes have already been defined, only the associated node numbers were required, and were calculated as follows:

$$N_{FM,i} = m\left\lfloor\frac{i * N_A}{25}\right\rfloor + m * N_A, \qquad 1 \le i \le 24 \tag{4.25}$$

$$N_{FM,i+24} = m\left\lfloor\frac{i * N_P}{25}\right\rfloor + m(t+1)N_A + m * N_P, \qquad 1 \le i \le 24 \tag{4.26}$$

Here, m represents the number of nodes in the radial direction, t represents the number of nodes across the leaflet thickness, and the floor function ($\lfloor\ \rfloor$) rounds down to the next, lowest integer. Finally, new nodes needed to be created where the single chordae branches off into two parts. This was achieved by first calculating the mid-point between the two free margin nodes, the mid-point between the papillary muscle node and the average of the two free margin nodes was then calculated.

$$N_{FMavg,i} = \frac{N_{FM,2i} + N_{FM,2i-1}}{2}, \qquad 1 \leq i \leq 24 \tag{4.27}$$

$$N_{B,i} = \frac{N_{PM,i} + N_{FMavg,i}}{2}, \qquad 1 \leq i \leq 24 \tag{4.28}$$

After calculating the coordinates of the new chordae branching nodes, N_B, all of the data required to generate the chordae beam elements was available. However, as was previously mentioned, since the individual bar elements cannot bend, each branch was split into four beam elements to improve the accuracy of the chordae modeling. The nodes required for this were generated by interpolating three new nodes between the papillary muscle nodes and the associated branching node, as well as three new nodes between the branching nodes and each associated insertion node along the free margin. As a result, each of the 24 chordae is composed of 12 two node beam elements (ELEMENT_BEAM) in LS-DYNA.

4.5. Load and Boundary Conditions

4.5.1. Pressure Loading

The movement of the mitral leaflets is the result of a fluid-structure interaction between the blood and the mitral leaflets as blood is pumped into and out of the left ventricle. However, it is not currently possible to accurately model the changes in the heart's geometry throughout the heartbeat, and therefore the flow of blood through (and around) the mitral valve cannot be accurately modeled either. Consequently, a structural model was selected to model the mitral valve, as this simplifies the simulation of the mitral dynamics, and reduces computation time. Therefore, the mitral valve dynamics are simulated by approximating the transmitral pressure gradient over the cardiac cycle (from end-diastole to early diastole), which is then applied to the ventricular surface of the leaflets using the LOAD_SEGMENT command in LS-DYNA. Since the datasets were completely de-identified, blood pressure data was not available for any of the datasets. Therefore, a pressure curve for a normal, healthy individual was assumed. This pressure curve has been well documented, and was obtained from a Wiggers diagram (Figure 4.14a). Since only the mitral dynamics during systole are of interest, the pressure curve was truncated to ignore the diastolic phase of the heartbeat, thus reducing computational time. Transmitral pressure data points from end-diastole to early diastole from a Wiggers diagram were obtained from a previous study on mitral dynamics by Iain Baxter (Figure 4.14b) [76], and applied to the ventricular surface of the leaflets. To further reduce computation time, the cardiac cycle was reduced to 1/10th of the actual cycle time, which, due to negligible inertial effects, has previously been found to provide accurate results [69].

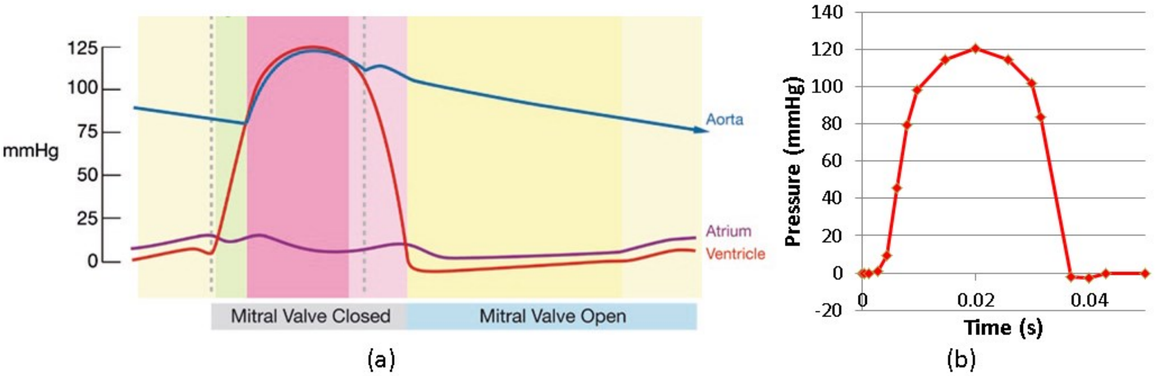

Figure 4.14: (a) Wiggers diagram depicting blood pressure in the heart over one heartbeat (modified from [15]), and (b) the transmitral pressure curve from end-diastole to early diastole employed in LS-DYNA.

4.5.2. Annular Displacements

The annulus experiences significant deformations during the cardiac cycle, with up to a 40% reduction in annular circumference during systole [15]. The annular area is largest during late diastole, begins to decrease at atrial systole, and reaches a minimum during late systole [15]. Measurements performed by Dagum *et al.* determined that the average change in diameter from commissure-to-commissure is 3.3 mm, and the average change in the peak-to-peak diameter is 3.7 mm [77]. To simplify the implementation of annular constriction, an average diameter change of 3.5 mm was assumed. Therefore, a displacement of 1.75 mm toward the long axis was applied to each node on the annulus using the BOUNDARY_PRESCRIBED_MOTION_NODE command in LS-DYNA. The annular circumference decreases linearly from end-diastole, reaching a minimum just prior to peak-systole. Following peak-systole, the annulus begins to dilate, and the annular circumference begins to increase linearly (Figure 4.15a). To simulate this change in annular area, the load curve presented in Figure 4.15b was employed in LS-DYNA to define the radial displacement of the annular nodes.

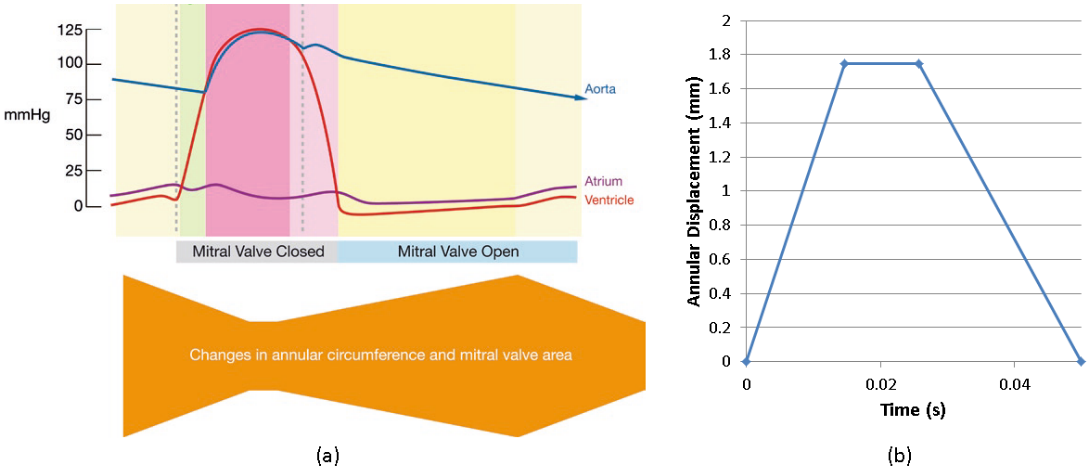

Figure 4.15: (a) Annular changes during the cardiac cycle (modified from [15]), and (b) the annular displacement applied in LS-DYNA.

4.5.3. Papillary Muscle Constraints

According to Sanfilippo *et al.*, the distance between the papillary muscles and annulus remains relatively constant throughout systole [78]. Since the annulus does not experience any vertical or rotational translation in this model, the papillary muscle nodes were fixed with respect to translation (but free to rotate). As a result, the distance between the papillary muscles and annulus is almost constant throughout the simulation—as expected. These constraints were applied to the papillary muscles using the BOUNDARY_SPC_NODE command in LS-DYNA.

4.6. Exporting the Model to LS-DYNA

The final step in the process of modeling the mitral valve requires the creation of an input file that can be opened by the FEA software LS-DYNA. Once all of the nodes, elements, material properties, and the loading and boundary conditions have been defined in MATLAB, they must be converted to a format that can used by LS-DYNA. This is achieved by creating a specifically formatted text file that contains all of the information required to generate the finite element model, and run the simulation. On top of the relevant finite element model information, this file also contains specific LS-DYNA commands required to run the mitral valve simulation. A sample of the MATLAB function that is used to generate the LS-DYNA input text files is included in Appendix B.

Chapter 5

5. Results and Discussion

In Chapters 3 and 4, the methods that were employed to generate the FE model of the mitral valve were presented, including the calculation and implementation of material properties, geometric reconstruction, and the application of loading and boundary conditions. This chapter will present the results of the mitral valve simulations, and highlight the importance of these results. To help determine the accuracy of the simulations, the following results will be considered:

- Leaflet geometry
- Mitral valve dynamics
- Leaflet stresses
- Chordae tendineae axial forces
- Leaflet bulging and leaflet angles

5.1. Introduction

Since this study focuses on validating the modeling and simulation of patient-specific mitral valve datasets, only healthy valves were considered. By focusing on modeling healthy mitral valves, the results can easily be compared to results obtained from previous studies that examined healthy mitral valves. Sixteen healthy datasets were obtained from the University of Ottawa Heart Institute, which were named MV1 to MV16. Of these 16 datasets, only 9 could be modeled. From the remaining seven datasets, five were omitted due to poor ultrasound image quality which prevented accurate geometric modeling of the mitral valve, and two were omitted because they did not contain the entire mitral apparatus.

5.2. Leaflet Geometry

In this study, two different methods were implemented to help determine the accuracy of the mitral models' geometry. First, the accuracy of the leaflets' geometry can be determined by directly comparing the model's geometry to the original ultrasound images (Figure 5.1). This is achieved by presenting the 3D ultrasound image using three perpendicular cross-sections, with the corresponding slices of the mitral model on top of these cross-sections. By adjusting the position of these three cross-sections, the entire valve can be examined and the user can determine if the final mitral model (after smoothing) is a good approximation of the real mitral valve. Using this method to examine all nine mitral models, they were all found to provide a very close match to the original ultrasound images. Specifically, the annulus and free-margin were consistently very close matches to the original ultrasound data. Furthermore, the commissures were accurately identified in all models, and the leaflets' profiles (from annulus to free-margin) were also accurately modeled. Finally, as anticipated, it was determined that a small amount of smoothing is beneficial to account for small errors when identifying the leaflet geometry. However, it is important to note that excessive smoothing negatively impacts the accuracy of the model—especially near the commissures.

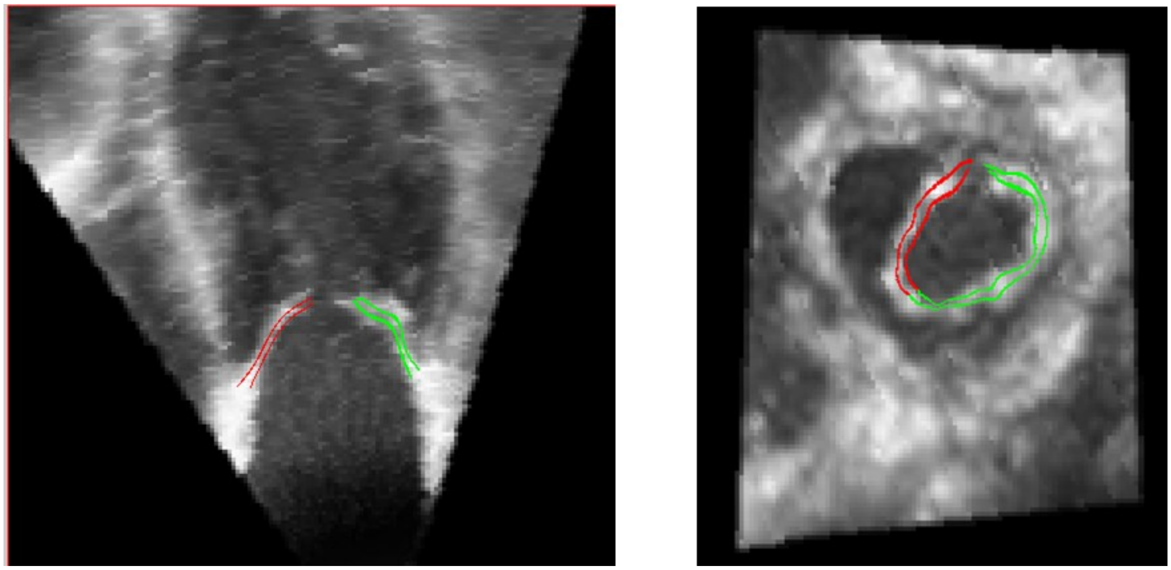

Figure 5.1: The anterior and posterior surfaces of a mitral valve model (MV1) are displayed in red and green, respectively, overlaid on a side view (left) and top view (right) of the original ultrasound image.

The second method used to determine the accuracy of the mitral models was the calculation of the mean, maximum, and minimum thicknesses of each leaflet. Since one of the main goals in the study was to accurately model local variations in leaflet thickness, this step was essential in determining the feasibility of this approach using ultrasound images. Unfortunately, due to the limited resolution of the ultrasound images, it is not possible to accurately calculate the leaflet thicknesses. However, since all of the datasets were obtained from individuals with healthy mitral valves, the leaflets' thicknesses could be compared to results from previous studies that measured leaflet thickness. The results of the mean, maximum, and minimum leaflet thicknesses are presented in Table 3. To help determine the accuracy of the mitral model, these results can be compared to the results from a study by Sahasakul *et al.* [79] which measured thicknesses at four locations on the anterior and posterior leaflets of 200 healthy human mitral valves (Table 4). For each leaflet, three thickness measurements were taken along the closing edge (sites 1, 2a, and

2b), and one measurement was taken at the centre of the leaflet's belly region (site 3) (Figure 5.2). While these measurements were only taken at select locations, the fact that the thicknesses of all nine mitral models fall within the study's range is promising. Although this method of data collection depends on the user's ability to identify the mitral leaflets, it would appear that local variations in thickness can be accurately modeled when proper care is taken.

Table 3: Finite element model leaflet thickness data for the nine healthy mitral valve datasets.

Mitral Model	Anterior Leaflet Thickness (mm)		Posterior Leaflet Thickness (mm)	
	Range	Mean ± SD	Range	Mean ± SD
MV1	0.48-3.20	1.457 ± 0.453	0.43-3.45	1.375 ± 0.504
MV3	0.24-2.53	1.257 ± 0.432	0.23-2.44	1.335 ± 0.383
MV4	0.71-2.95	1.597 ± 0.496	0.52-3.23	1.595 ± 0.538
MV7	0.34-3.14	1.584 ± 0.582	0.49-2.59	1.268 ± 0.380
MV8	0.36-2.72	1.300 ± 0.433	0.28-2.03	1.102 ± 0.325
MV9	0.35-3.35	1.281 ± 0.517	0.34-2.53	1.130 ± 0.395
MV12	0.35-2.67	1.359 ± 0.470	0.39-2.63	1.275 ± 0.455
MV13	0.87-4.06	2.314 ± 0.600	0.72-3.53	1.471 ± 0.474
MV14	0.43-2.25	1.181 ± 0.387	0.34-2.14	1.141 ± 0.376

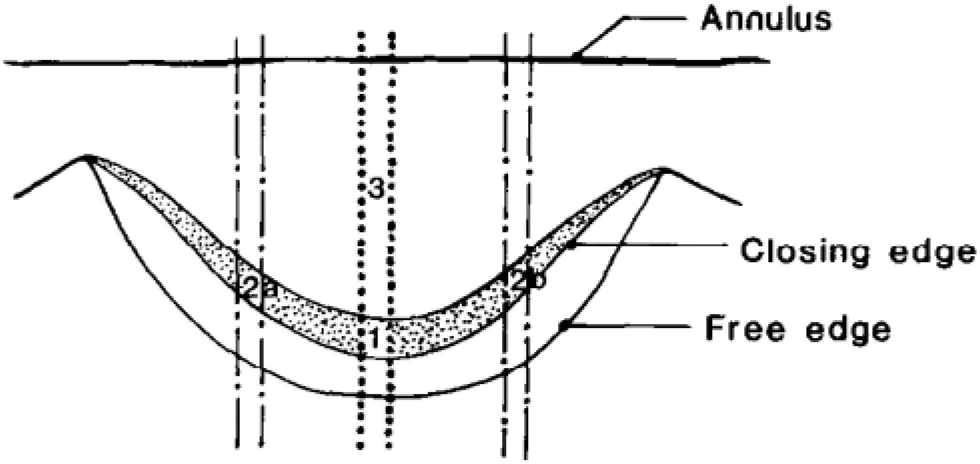

Figure 5.2: Diagram of the mitral valve illustrating the four sites of measurement selected by Sahasakul *et al.* (modified from [79]).

Table 4: Mitral valve thicknesses in 200 normal hearts (AL=anterior leaflet, PL=posterior leaflet) [79].

Site	Thickness (mm)	
	Range	Mean ± SD
AL1	0.40-3.40	1.21 ± 0.60
AL2a	0.50-5.60	1.73 ± 1.01
AL2b	0.50-9.00	2.19 ± 1.39
AL3	0.35-1.80	0.71 ± 0.30
PL1	0.45-3.00	1.18 ± 0.53
PL2a	0.55-3.00	1.32 ± 0.56
PL2b	0.55-3.20	1.45 ± 0.70
PL3	0.30-1.80	0.78 ± 0.24

5.3. Mitral Valve Dynamics

In this section, the mitral valve's dynamics will be presented using images of the mitral models at specific points during the simulation. These points, which are depicted in Figure 5.3, represent end diastole ($t = 0$ s, P = 0 mmHg), the end of isovolumetric contraction ($t = 0.008$ s, P = 79.5 mmHg), peak systole ($t = 0.02$ s, P = 121 mmHg), the end of systole ($t = 0.03$ s, P = 101 mmHg), the end of isovolumetric relaxation ($t = 0.037$ s, P = -2.29 mmHg), and early diastole ($t = 0.05$ s, P = -0.5 mmHg).

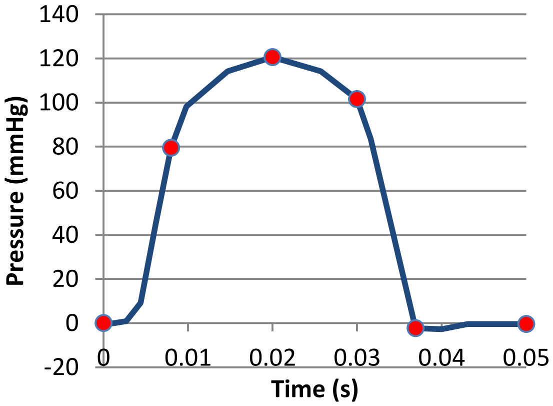

Figure 5.3: Pressure load curve applied to the ventricular surface of the mitral leaflet. The red circles depict the location for which the analysis images are presented.

The dynamics of a healthy mitral valve model (MV1) are presented in Figure 5.4, by displaying the valve's positioning at the six points of interest depicted by the red circles in Figure 5.3. As expected, all nine models displayed very similar behaviour throughout the simulation; therefore the dynamics of all nine models will be discussed together. However, images depicting the dynamics of each of the mitral models are presented in Appendix C.

During isovolumetric contraction ($t = 0 - 0.008$ s), the left ventricle begins to contract and pressure increases rapidly. The rapid increase in pressure causes the mitral valve to begin to close, and there is minimal back flow into the left atrium due to the formation of vortices [80]. In all nine simulations, the mitral valve was found to have almost completely closed by the end of the isovolumetric contraction phase. At this point, only small orifices remained near the creases in the leaflets, which occur at the two commissures, and often between the scallops of the posterior leaflet as well. The isovolumetric contraction phase is proceeded by the ejection phase, where ventricular contraction causes the blood to be pumped out of the left ventricle through the aortic valve. The mitral valve models quickly reached complete closure early in the ejection phase (around $t = 0.01$ s), preventing any backflow into the left atrium as the ventricular pressure continues to increase until peak systole ($t = 0.02$ s). Although the ventricular pressure begins to decrease after peak systole, the mitral valve remains completely closed until the end of the systolic phase ($t = 0.03$ s). Systole is followed by a rapid decrease in ventricular pressure caused by the isovolumetric relaxation of the left ventricle. However, the mitral valve remains closed for most of this stage, and the leaflets only begin to separate near the end of the isovolumetric relaxation phase as the ventricular pressure approaches the atrial pressure. Following the end of the isovolumetric relaxation phase, the mitral valve continues to open as the pressure gradient forces blood to flow from the left atrium, through the mitral valve, and into the left ventricle.

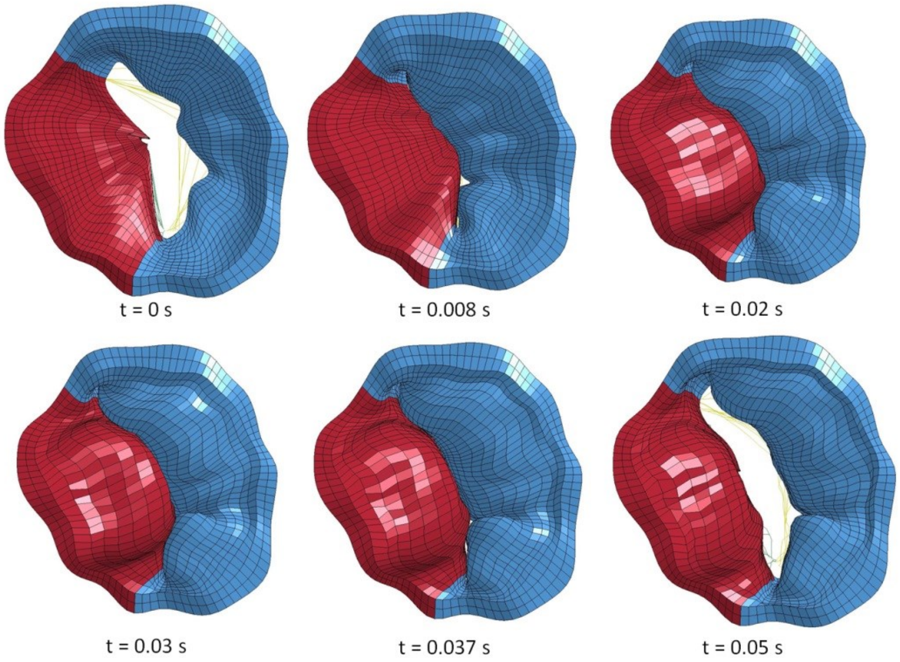

Figure 5.4: Top view (from the left atrium) showing the behaviour of the healthy mitral valve model, MV1, at specific points of interest.

While the main goal of this study was to develop a framework that allows for the accurate simulation of mitral valve dynamics from patient datasets, the results can be difficult to quantify. Therefore, the quality of the results may be determined qualitatively by comparing the simulations with the expected mitral behaviour. Since all mitral valve datasets were obtained from healthy subjects, all nine simulations should mimic the expected behaviour of healthy mitral valves. First and foremost, the two leaflets should fold at the commissures to form a tight seal during systole. Closure of the mitral valve is known to occur rapidly at the beginning of the systolic phase, as the pressure gradient increases rapidly from 0 to 100 mmHg [15], [80]. This behaviour was observed in all of the simulations, with initial closure occurring around 0.006 s after the ventricular pressure surpasses the atrial pressure, and complete closure occurring 0.003 s after that. The valves then remained closed until the end of the isovolumetric phase, as expected. Since these results closely match the expected results, it suggests that the geometric reconstruction, as well as the material properties, and the load and boundary conditions are capable of accurately approximating the *in vivo* mitral dynamics.

5.4. Leaflet Stresses

When examining the leaflet stresses in healthy mitral valves, the main point of interest is at peak systole when the pressure acting on the leaflets is highest. The leaflet stresses are presented in the form of contour plots depicting the von Mises stresses. To improve the contrast of the stress plots, a maximum von Mises stress of 0.5 MPa was selected for all models depicted in red. However, any regions where the von Mises stress exceeds 0.5 MPa are displayed in gray. Since similar stress patterns were present in all nine mitral models, the general stress distribution will be discussed in this section, but the von Mises contour plots of all nine models are available in Appendix C.

As shown by the von Mises stress contour plots in Figure 5.5, the belly region of the leaflets tend to experience moderate stresses at peak systole, with the anterior leaflet experiencing slightly higher stresses than the posterior leaflet. The stresses in the belly of the leaflets generally range from approximately 0.1-0.4 MPa and 0.05-0.3 MPa in the anterior and posterior leaflets, respectively. The stresses tend to diminish towards the annulus and commissures, but increases near the centre of the free margin on both leaflets. The high stresses that are often present at the free margin are likely caused by the chordae tendineae. In this model, each chordae tendineae attaches to the leaflet at a single node, therefore resulting in large, localized forces. However, *in vivo*, the chordae attach to the leaflet over a larger area, therefore these large stresses along the leaflets' free margin are likely larger than the *in vivo*, stresses. Furthermore, since the distribution of the chordae tendineae could not be determined from the ultrasound images, and therefore had to be assumed, improper distribution of the chordae could also affect the magnitude of the stresses near the free margin. Finally, some models showed small regions of high stress near the annulus. Since a simplified model of the annular dynamics was assumed for the mitral models, this could be responsible for the localized regions of high stress along the annulus. Although *in vivo* leaflet stress measurements are not available, the observed von Mises stress patterns appear to match the results of previously reported mitral valve models [39], [42].

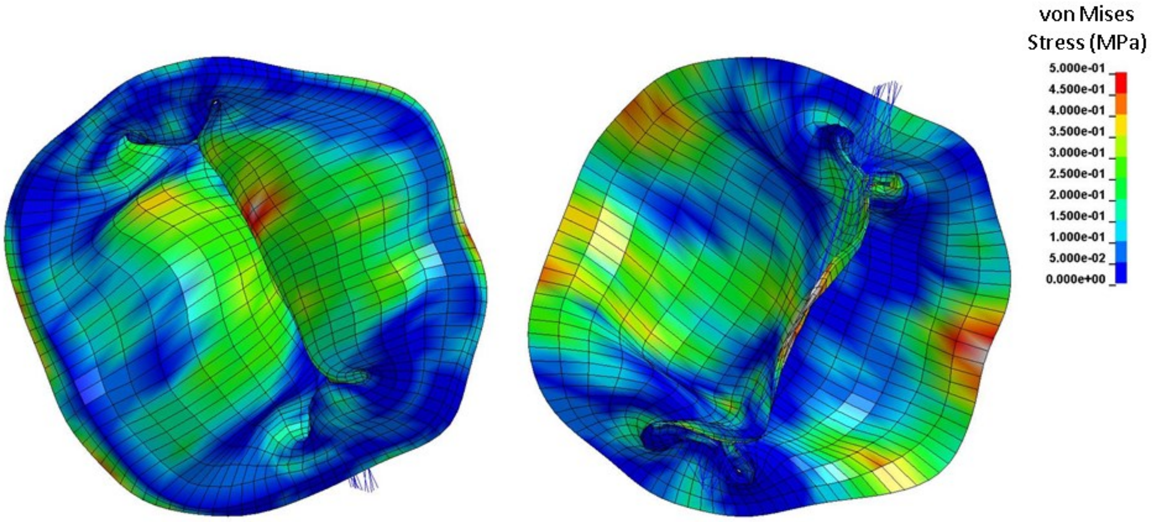

Figure 5.5: von Mises stress contour plot of the healthy mitral valve dataset MV3 viewed from the atrial (left) and ventricular (right) sides. Note that all stresses exceeding 0.5 MPa are displayed in gray.

5.5. Chordae Tendineae Axial Forces

The chordae tendineae are responsible for preventing leaflet prolapse during ventricular systole. Therefore, the tensile loads experienced by the chordae are closely linked to the ventricular pressure. The average and maximum axial forces experienced by the chordae were determined for each analysis. These values were calculated in LS-DYNA and output to a text file at 11 time points (0.005 s intervals). The chordae forces for each model are presented in Appendix C, but for the purpose of displaying the data, the chordae forces for the nine models were averaged, and along with the standard deviation, were plotted in Microsoft Excel (Figure 5.6). In all nine cases, the axial load increased rapidly at the start of systole, reaching a maximum at peak systole. The axial forces remained roughly constant between peak systole and the end of systole (start of isovolumetric relaxation), where the forces dropped rapidly to nearly zero at the beginning of diastole. As the error bars in Figure 5.6 indicate, there was a significant difference between the maximum tensile forces experienced by each model, but the average tensile loads were very similar in all nine models. Since the average forces remained relatively constant between models, and was significantly lower than the maximum tensile forces, this suggests that loads were not distributed evenly across the chordae tendineae.

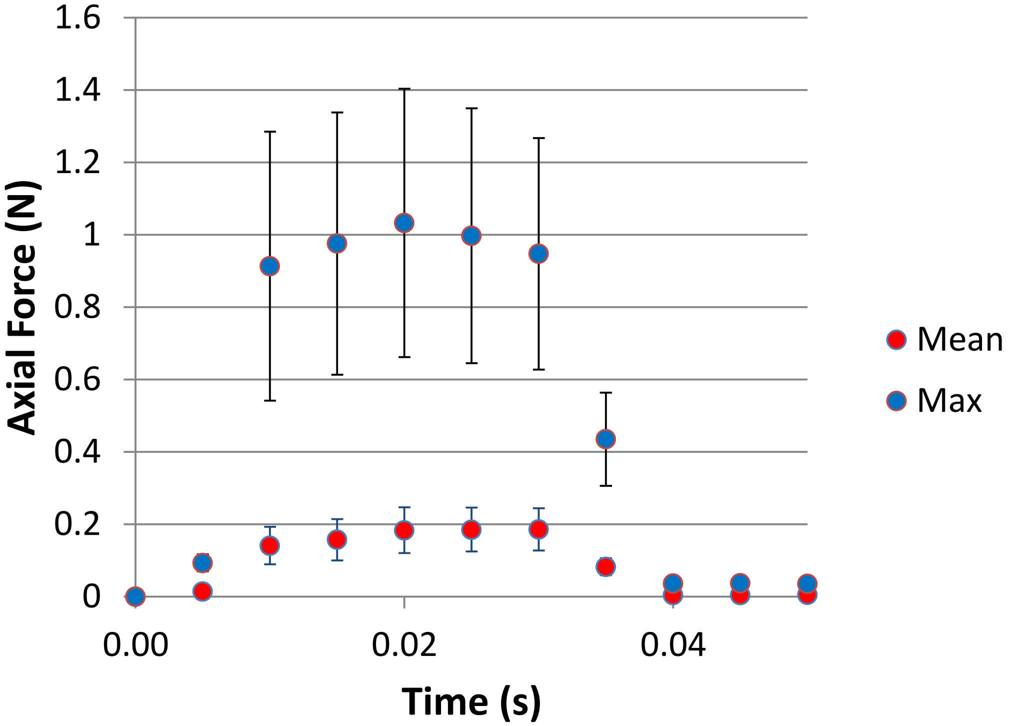

Figure 5.6: The mean and maximum chordae forces, averaged from the nine mitral models.

In each model, the chordae forces fluctuated throughout the cardiac cycle but followed the expected trend, with the forces increasing rapidly at the start of systole, and decreasing rapidly at the start of diastole. One study by Nielsen *et al.* attempted to determine the average chordal forces by using a left heart simulator to measure the chordae forces *in vitro* [81]. This study found an average tensile load of approximately 0.46 N per chordae, which is significantly higher than the average chordae force measured in all nine models. Since the number of chordae varies significantly between valves, it is possible that the discrepancy between the experimental results and the average chordae forces calculated in the finite element model could be the result of the total load being distributed among fewer chordae in the *in vitro* study. However, another study performed by Jensen *et al.* found that the papillary muscle heads carry a load of approximately 2.5 N at mid-systole [82]. If this load were distributed across 12 chordae it would equate to approximately 0.21 N per chordae, which is very close to the simulated results which had an average peak systolic load of 0.183 N per chordae. Despite the uneven load distribution among chordae, the total load on the papillary muscle heads appears to agree with the available experimental data. Furthermore, since there is no *in vivo* data available on the distribution of forces among the marginal chordae, it is not unreasonable to assume that certain chordae would experience significantly higher than average loads, as was observed in these simulations.

5.6. Leaflet Bulging and Leaflet Angles

The degree to which the mitral leaflets bulge into the left atrium during systole is another method of analysing valve function. Healthy mitral valves are normally relatively flat when closed, showing very little bulging towards the atrium. For the purpose of this study, bulging will only be considered when one or both of the leaflets cross the plane that connects the anterior and posterior annulus, as this is abnormal for healthy mitral valves. A second metric that will be considered is the leaflet angles, defined as the angle between the line connecting the anterior and posterior annulus, and the straight line that connects the annulus to the site of leaflet coaptation. Both the leaflet bulging and the leaflet angles were determined from a cross-sectional image that intersects the centre of both leaflets at peak systole ($t = 0.02$ s).

To determine the amount of bulging, the distance from the anterior to posterior annulus was measured in LS-DYNA (in millimeters). This cross-sectional image was then exported to ImageJ, where the five dimensions indicated in Figure 5.7 were measured (in pixels), and using these dimensions the two leaflet angles (also indicated in Figure 5.7) were calculated. First, the ratio between the annulus measurement in LS-DYNA and ImageJ was used to convert the pixel measurements into millimeters $\left(l_{mm} = l_{pixels}\frac{l_{AP,LS-DYNA}}{l_{AP,ImageJ}}\right)$. Although the curvature of the leaflets was greater than normally expected in healthy mitral valves, most leaflets did not cross the transannular plane, which is depicted by the line l_{AP}. The leaflet angles, α_A and α_P, were calculated using the lengths l_{AP}, l_{AC}, and l_{PC}, and the cosine law. The results are presented in Table 5, and the raw data is available in Appendix C.

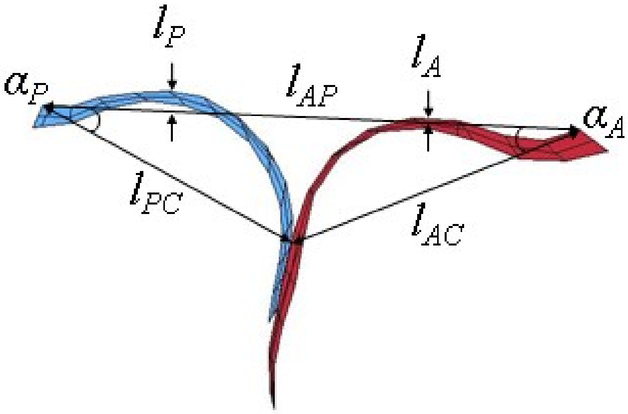

Figure 5.7: Measurements used to determine leaflet bulging and leaflet angles.

Table 5: Relevant measurements for calculating leaflet bulging and leaflet angles.

Mitral Model	l_{AP} (mm)	l_{AC} (mm)	l_{PC} (mm)	l_P (mm)	l_A (mm)	α_A (degrees)	α_P (degrees)
MV1	24.817	17.783	12.476	N/A	N/A	28.393	42.670
MV3	35.148	20.282	18.490	1.265	0.265	23.763	26.232
MV4	28.936	17.452	16.400	N/A	N/A	30.198	32.362
MV7	34.332	22.061	17.389	0.450	N/A	25.870	33.610
MV8	35.017	22.133	17.391	1.910	1.258	24.221	31.476
MV9	30.523	20.915	14.411	0.672	N/A	24.544	37.075
MV12	34.411	23.388	16.185	N/A	N/A	24.112	36.180
MV13	28.722	28.405	4.617	N/A	1.944	9.250	81.452
MV14	24.622	17.469	11.858	N/A	N/A	26.362	40.854

Although most of the leaflets did not bulge into the left atrium, more curvature of the leaflets was observed than is typical of healthy leaflets. As was previously mentioned, healthy leaflets generally form a fairly straight line between the annulus and site of coaptation at peak-systole, while the simulated leaflets displayed noticeable bending. This increased bending is likely the result of using porcine material data to model the leaflets' mechanical properties as previous research by Prot *et al.* found that implementing human leaflet material properties significantly reduced bulging of the leaflets [52]. Unfortunately, there was not enough published data available to calculate the material constants required to model healthy human mitral leaflets.

Despite the limitations due the use of porcine material data for both leaflets, leaflet angles were a very close match to the reported results for healthy mitral valves. In a study that examined CT images of 84 healthy mitral valves, Delgado *et al.* found that the mean anterior and posterior leaflet angles were 24.6 ± 7.0° and 34.7 ± 9.6°, respectively [83]. Of the nine healthy mitral valves that were examined, only one valve (MV13) did not fall within this range. Although both of the measured leaflet angles for MV13 ($\alpha_A = 9.25°$ and $\alpha_P = 81.452°$) were well outside of the expected range, this result does not appear to be indicative of an error with the simulation. Instead, this valve appears to be an anomaly, as examining the initial ultrasound data appears to confirm these results. This valve has an abnormally short posterior leaflet, and as a result the anterior leaflet must reach a much smaller angle to ensure valve closure. Due to the limited resolution, accurately determining leaflet angles from the ultrasound data is very difficult; nevertheless, in an attempt to confirm the results of dataset MV13, the necessary measurements were taken from the ultrasound image at peak systole to estimate the leaflet angles. From the ultrasound data, it was determined that the anterior and posterior leaflet angles were approximately 11° and 77°, respectively, at peak systole. Since the ultrasound's limited resolution makes it difficult to identify the point of coaptation at peak systole, these angles are merely an approximation. However, since these values are only a few degrees different than the angles observed in the simulation, it helps to confirm that the abnormal angles are not a result of simulation errors. Since the angles for the other valves were within the expected range, and due to the limited accuracy that can be expected from leaflet angle measurements taken from the ultrasound images, the ultrasound leaflet angles were not calculated for the other datasets. Despite the excessive bulging resulting from the use of porcine leaflet properties, the simulations appear to provide accurate results, with simulated leaflet angles matching previously reported results.

Chapter 6

6. Conclusions and Future Work

In this thesis, the challenges facing the generation of accurate finite element models of the mitral valve were addressed. This work included exploring the challenges of accurately modeling the mitral apparatus's geometry, the material properties of biological tissues, and the *in vivo* loading and boundary conditions.

6.1.Summary of Findings

The objectives of this study were to develop a framework for constructing accurate, patient-specific finite element models of the mitral apparatus using 4D TEE data. First, a method was described for optimizing the leaflet material properties based on previously reported experimental results. The non-linear, transversely isotropic material properties of the mitral valve leaflets were implemented using the Guccione strain energy equation in LS-DYNA (MAT_HEART_TISSUE). Simulated biaxial tests were performed in LS-DYNA to optimize the material constants of the Guccione strain energy equation to match the results of previous studies that implemented different strain energy functions to model the leaflets' mechanical behaviour. Next, two MATLAB programs were developed to process the 4D TEE datasets, and extract the valve's geometric data to generate 3D finite element models of the valve. Both the atrial and ventricular surfaces of the leaflets were identified in the ultrasound images, resulting in a 3D finite element model that closely matched the ultrasound data, and closely matched the expected leaflet thicknesses reported in the literature.

Sixteen ultrasound datasets from healthy mitral valves were provided by the University of Ottawa Heart Institute. Of these sixteen datasets, seven were discarded due to poor image quality. The remaining nine datasets were processed, and simulations were run from end-diastole to early diastole using LS-DYNA. As anticipated, analysis of all nine mitral models revealed normal functioning valves. The dynamics of the valves was consistent with the literature, thus validating the accuracy of the mitral modeling algorithm. The leaflet stresses and chordae tendineae forces also corresponded with the values reported in the literature. However, a few models displayed localized areas of relatively high stresses near the annulus and free margin. Since these models did not include patient-specific annular dynamics, slight discrepancies between the *in vivo* and simulated annular motion were likely responsible for areas of high stress near the annulus. Furthermore, since the chordae tendineae attach at a single node in the mitral models, instead of being distributed over a slightly larger area as is the case with real chordae tendineae, this is likely the cause of the high localized stresses near the leaflets' free margin.

6.2. Possibilities for Future Work

There are a few possibilities for future work involving the modeling methods developed in this study. First, this framework could be used to predict the outcome of various mitral valve surgeries. By generating finite element models of diseased mitral valves and simulating a variety of surgeries using these models, surgical outcomes could be predicted. This could provide surgeons with a tool for determining the most appropriate repair technique(s). Furthermore, to help improve long-term success rates, several iterations of a surgery could be performed to help optimize surgical results by minimizing the leaflet stresses and improving leaflet coaptation. This could also be used to help in the development of new designs for annuloplasty rings, and other surgical repair techniques.

Another possibility is to continue to improve upon the accuracy of the mitral models by including more patient-specific data. Due to a lack of patient data, the current model assumes a normal pressure curve based on the Wiggers diagram. However, by implementing patient-specific transvalvular pressure gradient data, the accuracy of the simulations could be improved. Furthermore, by including patient-specific annular and papillary muscle dynamics, the accuracy of the leaflet stresses and dynamics could be improved.

The accuracy of the simulations could also be improved by implementing more accurate material properties. Unfortunately, very little material data is currently available for human mitral tissues. Therefore, it was necessary to employ porcine material data to model healthy human mitral leaflets. While some data is available for diseased human mitral leaflets, more material data would also be beneficial to help validate these results. Improving the accuracy of the material properties is essential to ensuring accurate mitral simulations.

Finally, by implementing fluid-structure interaction methods, blood flow could be included in the model. By including blood flow in the simulation, local variations in pressure due to the formation of vortices could be modeled, which should improve the accuracy of the simulations. This could also prove to be beneficial in the simulation of mitral repairs as it would help to ensure proper filling of the left ventricle during diastole.

References

[1] “WHO | Cardiovascular diseases (CVDs),” *WHO*. [Online]. Available: http://www.who.int/mediacentre/factsheets/fs317/en/. [Accessed: 13-May-2015].

[2] “World Population Ageing 2013,” United Nations.

[3] J. L. d’Arcy, B. D. Prendergast, J. B. Chambers, S. G. Ray, and B. Bridgewater, “Valvular heart disease: the next cardiac epidemic,” *Heart*, vol. 97, no. 2, pp. 91–93, Jan. 2011.

[4] A. S. Go, D. Mozaffarian, V. L. Roger, E. J. Benjamin, J. D. Berry, W. B. Borden, D. M. Bravata, S. Dai, E. S. Ford, C. S. Fox, S. Franco, H. J. Fullerton, C. Gillespie, S. M. Hailpern, J. A. Heit, V. J. Howard, M. D. Huffman, B. M. Kissela, S. J. Kittner, D. T. Lackland, J. H. Lichtman, L. D. Lisabeth, D. Magid, G. M. Marcus, A. Marelli, D. B. Matchar, D. K. McGuire, E. R. Mohler, C. S. Moy, M. E. Mussolino, G. Nichol, N. P. Paynter, P. J. Schreiner, P. D. Sorlie, J. Stein, T. N. Turan, S. S. Virani, N. D. Wong, D. Woo, and M. B. Turner, “Heart Disease and Stroke Statistics—2013 Update A Report From the American Heart Association,” *Circulation*, vol. 127, no. 1, pp. e6–e245, Jan. 2013.

[5] S. F. Bolling, “Can We Predict Mitral Valve Repair Rates by Individual Surgeons’ Mitral Volume?,” *Tex. Heart Inst. J.*, vol. 38, no. 6, pp. 703–704, 2011.

[6] W. Flameng, P. Herijgers, and K. Bogaerts, “Recurrence of Mitral Valve Regurgitation After Mitral Valve Repair in Degenerative Valve Disease,” *Circulation*, vol. 107, no. 12, pp. 1609–1613, Apr. 2003.

[7] E. Braunberger, A. Deloche, A. Berrebi, F. Abdallah, J. A. Celestin, P. Meimoun, G. Chatellier, S. Chauvaud, J. N. Fabiani, and A. Carpentier, “Very long-term results (more than 20 years) of valve repair with Carpentier’s techniques in nonrheumatic mitral valve insufficiency,” *Circulation*, vol. 104, no. 12 Suppl 1, pp. I8–11, 2001.

[8] A. M. Gillinov, E. H. Blackstone, E. R. Nowicki, W. Slisatkorn, G. Al-Dossari, D. R. Johnston, K. M. George, P. L. Houghtaling, B. Griffin, J. F. Sabik, and L. G. Svensson, “Valve repair versus valve replacement for degenerative mitral valve disease,” *J. Thorac. Cardiovasc. Surg.*, vol. 135, no. 4, pp. 885–e2.

[9] D. Mohty, T. A. Orszulak, H. V. Schaff, J.-F. Avierinos, J. A. Tajik, and M. Enriquez-Sarano, “Very Long-Term Survival and Durability of Mitral Valve Repair for Mitral Valve Prolapse,” *Circulation*, vol. 104, no. suppl 1, pp. I–1–I–7, Sep. 2001.

[10] C.-H. Lee, J.-P. Rabbah, A. P. Yoganathan, R. C. Gorman, J. H. Gorman, and M. S. Sacks, “On the effects of leaflet microstructure and constitutive model on the closing behavior of the mitral valve,” *Biomech. Model. Mechanobiol.*, May 2015.

[11] F. J. Schoen and R. J. Levy, “Calcification of Tissue Heart Valve Substitutes: Progress Toward Understanding and Prevention,” *Ann. Thorac. Surg.*, vol. 79, no. 3, pp. 1072–1080, Mar. 2005.

[12] “Blood Flow Through The Heart Oxygenated And Deoxygenated.” [Online]. Available: http://imgkid.com/blood-flow-through-the-heart-oxygenated-and-deoxygenated.shtml. [Accessed: 13-May-2015].

[13] “OpenStax CNX - Heart Anatomy.” [Online]. Available: http://cnx.org/contents/6394ffc1-5482-4aa6-9233-23ad34848fa0@4/Heart_Anatomy. [Accessed: 13-May-2015].

[14] A. Pick, "'What Is The Mitral Valve Annulus?' Asks Dana," *Adam's Heart Valve Surgery Blog*, 02-Sep-2008. .

[15] A. Haverich, *Mitral Valve Surgery*. 2011.

[16] J. J. Silbiger, "Anatomy, mechanics, and pathophysiology of the mitral annulus," *Am. Heart J.*, vol. 164, no. 2, pp. 163–176, 2012.

[17] S. A. Gunnal, M. S. Farooqui, and R. N. Wabale, "Study of Mitral Valve in Human Cadaveric Hearts," *Heart Views Off. J. Gulf Heart Assoc.*, vol. 13, no. 4, pp. 132–135, 2012.

[18] "Mitral Valve Stenosis - Overview," 24-Sep-2014. [Online]. Available: https://myhealth.alberta.ca/health/Pages/conditions.aspx?hwid=ue1003. [Accessed: 15-May-2015].

[19] "Mitral stenosis: MedlinePlus Medical Encyclopedia." [Online]. Available: http://www.nlm.nih.gov/medlineplus/ency/article/000175.htm. [Accessed: 19-May-2015].

[20] "Normal heart and heart with mitral valve stenosis - Mayo Clinic." [Online]. Available: http://www.mayoclinic.org/diseases-conditions/mitral-valve-stenosis/multimedia/img-20110854. [Accessed: 19-May-2015].

[21] L. A. Piérard and B. A. Carabello, "Ischaemic mitral regurgitation: pathophysiology, outcomes and the conundrum of treatment," *Eur. Heart J.*, p. ehq411, Dec. 2010.

[22] "CT Scan vs MRI - Difference and Comparison | Diffen." [Online]. Available: http://www.diffen.com/difference/CT_Scan_vs_MRI. [Accessed: 21-May-2015].

[23] C. Storrs, "How Much Do CT Scans Increase the Risk of Cancer?," *Scientific American*, 18-Jun-2013. [Online]. Available: http://www.scientificamerican.com/article/how-much-ct-scans-increase-risk-cancer/. [Accessed: 21-May-2015].

[24] "Valve Surgery & Balloon Valvotomy," *Cleveland Clinic*. [Online]. Available: http://my.clevelandclinic.org/services/heart/disorders/valvetreatment. [Accessed: 22-May-2015].

[25] "Components of a Mechanical Heart Valve," *On-X Life Technologies, Inc.* [Online]. Available: http://www.onxlti.com/patient-guide/components-mechanical-heart-valve/. [Accessed: 22-May-2015].

[26] A. Pick, "Mechanical Or Bioprosthetic Heart Valve Replacements?," *Adam's Heart Valve Surgery Blog*. .

[27] "CVT Surgical Center - Services: Cardiac - Mitral Valve Repair and Replacement." [Online]. Available: http://www.cvtsc.com/surgery/cardiac_mitral-valve.html. [Accessed: 22-May-2015].

[28] "Magna Mitral Heart Valve Implantation Manual - Introduction and Product Description." [Online]. Available: http://www.edwards.com/Products/HeartValves/Pages/mmimplantintro.aspx. [Accessed: 22-May-2015].

[29] "Mitral Valve Repair," *Cleveland Clinic*. [Online]. Available: http://my.clevelandclinic.org/services/heart/disorders/valvetreatment/mitral-valve-repair. [Accessed: 22-May-2015].

[30] M. Enriquez-Sarano, H. V. Schaff, T. A. Orszulak, A. J. Tajik, K. R. Bailey, and R. L. Frye, "Valve Repair Improves the Outcome of Surgery for Mitral Regurgitation A Multivariate Analysis," *Circulation*, vol. 91, no. 4, pp. 1022–1028, Feb. 1995.

[31] J. S. Rankin, B. G. Hammill, T. B. Ferguson Jr., D. D. Glower, S. M. O'Brien, E. R. DeLong, E. D. Peterson, and F. H. Edwards, "Determinants of operative mortality in valvular heart surgery," *J. Thorac. Cardiovasc. Surg.*, vol. 131, no. 3, pp. 547–557, Mar. 2006.

[32] J. S. Gammie, S. Sheng, B. P. Griffith, E. D. Peterson, J. S. Rankin, S. M. O'Brien, and J. M. Brown, "Trends in Mitral Valve Surgery in the United States: Results From The Society of Thoracic Surgeons Adult Cardiac Database," *Ann. Thorac. Surg.*, vol. 87, no. 5, pp. 1431–1439, May 2009.

[33] J. J. Jokinen, M. J. Hippeläinen, O. A. Pitkänen, and J. E. K. Hartikainen, "Mitral Valve Replacement Versus Repair: Propensity-Adjusted Survival and Quality-of-Life Analysis," *Ann. Thorac. Surg.*, vol. 84, no. 2, pp. 451–458.

[34] C. A. Milano, M. A. Daneshmand, J. S. Rankin, E. Honeycutt, M. L. Williams, M. Swaminathan, L. Linblad, L. K. Shaw, D. D. Glower, and P. K. Smith, "Survival Prognosis and Surgical Management of Ischemic Mitral Regurgitation," *Ann. Thorac. Surg.*, vol. 86, no. 3, pp. 735–744, Sep. 2008.

[35] D. H. Adams, A. C. Anyanwu, P. B. Rahmanian, and F. Filsoufi, "Current concepts in mitral valve repair for degenerative disease," *Heart Fail. Rev.*, vol. 11, no. 3, pp. 241–257.

[36] "Mayo Clinic leads multinational study establishing benefit of early surgical correction of mitral valve regurgitation - For Medical Professionals - Mayo Clinic," *Mayo Clinic*. [Online]. Available: http://www.mayoclinic.org/medical-professionals/clinical-updates/cardiovascular/early-surgical-correction-mitral-valve-regurgitation. [Accessed: 25-May-2015].

[37] J. Bonet and R. D. Wood, *Nonlinear Continuum Mechanics for Finite Element Analysis*. Cambridge: Cambridge University Press, 2008.

[38] T. Mansi, I. Voigt, B. Georgescu, X. Zheng, E. A. Mengue, M. Hackl, R. I. Ionasec, T. Noack, J. Seeburger, and D. Comaniciu, "An integrated framework for finite-element modeling of mitral valve biomechanics from medical images: Application to MitralClip intervention planning," *Med. Image Anal.*, vol. 16, no. 7, pp. 1330–1346, Oct. 2012.

[39] Y. Rim, D. D. McPherson, K. B. Chandran, and H. Kim, "The effect of patient-specific annular motion on dynamic simulation of mitral valve function," *J. Biomech.*, vol. 46, no. 6, pp. 1104–1112, Apr. 2013.

[40] E. Votta, E. Caiani, F. Veronesi, M. Soncini, F. M. Montevecchi, and A. Redaelli, "Mitral valve finite-element modelling from ultrasound data: a pilot study for a new approach to understand mitral function and clinical scenarios," *Philos. Trans. R. Soc. Lond. Math. Phys. Eng. Sci.*, vol. 366, no. 1879, pp. 3411–3434, Sep. 2008.

[41] B. Skallerud, V. Prot, and I. S. Nordrum, "Modeling active muscle contraction in mitral valve leaflets during systole: a first approach," *Biomech. Model. Mechanobiol.*, vol. 10, no. 1, pp. 11–26, Apr. 2010.

[42] A. M. Pouch, C. Xu, P. A. Yushkevich, A. S. Jassar, M. Vergnat, J. H. Gorman III, R. C. Gorman, C. M. Sehgal, and B. M. Jackson, "Semi-automated mitral valve morphometry and computational stress analysis using 3D ultrasound," *J. Biomech.*, vol. 45, no. 5, pp. 903–907, Mar. 2012.

[43] A. S. Jassar, C. J. Brinster, M. Vergnat, J. D. Robb, T. J. Eperjesi, A. M. Pouch, A. T. Cheung, S. J. Weiss, M. A. Acker, J. H. Gorman III, R. C. Gorman, and B. M.

Jackson, “Quantitative Mitral Valve Modeling Using Real-Time Three-Dimensional Echocardiography: Technique and Repeatability,” *Ann. Thorac. Surg.*, vol. 91, no. 1, pp. 165–171, Jan. 2011.

[44] T. Mansi, I. Voigt, E. A. Mengue, R. Ionasec, B. Georgescu, T. Noack, J. Seeburger, and D. Comaniciu, “Towards Patient-Specific Finite-Element Simulation of MitralClip Procedure,” in *Medical Image Computing and Computer-Assisted Intervention – MICCAI 2011*, G. Fichtinger, A. Martel, and T. Peters, Eds. Springer Berlin Heidelberg, 2011, pp. 452–459.

[45] Y. Rim, S. T. Laing, D. D. McPherson, and H. Kim, “Mitral Valve Repair Using ePTFE Sutures for Ruptured Mitral Chordae Tendineae: A Computational Simulation Study,” *Ann. Biomed. Eng.*, vol. 42, no. 1, pp. 139–148, Sep. 2013.

[46] M. Stevanella, F. Maffessanti, C. A. Conti, E. Votta, A. Arnoldi, M. Lombardi, O. Parodi, E. G. Caiani, and A. Redaelli, “Mitral Valve Patient-Specific Finite Element Modeling from Cardiac MRI: Application to an Annuloplasty Procedure,” *Cardiovasc. Eng. Technol.*, vol. 2, no. 2, pp. 66–76, Jun. 2011.

[47] Q. Wang and W. Sun, “Finite Element Modeling of Mitral Valve Dynamic Deformation Using Patient-Specific Multi-Slices Computed Tomography Scans,” *Ann. Biomed. Eng.*, vol. 41, no. 1, pp. 142–153, Jul. 2012.

[48] G. A. Holzapfel and R. W. Ogden, “On planar biaxial tests for anisotropic nonlinearly elastic solids. A continuum mechanical framework,” *Math. Mech. Solids*, vol. 14, no. 5, pp. 474–489, Jul. 2009.

[49] K. S. Kunzelman and R. P. Cochran, “Stress/Strain Characteristics of Porcine Mitral Valve Tissue: Parallel Versus Perpendicular Collagen Orientation,” *J. Card. Surg.*, vol. 7, no. 1, pp. 71–78, Mar. 1992.

[50] K. May-Newman and F. C. Yin, “Biaxial mechanical behavior of excised porcine mitral valve leaflets,” *Am. J. Physiol.*, vol. 269, no. 4 Pt 2, pp. H1319–1327, Oct. 1995.

[51] K. May-Newman and F. C. P. Yin, “A Constitutive Law for Mitral Valve Tissue,” *J. Biomech. Eng.*, vol. 120, no. 1, pp. 38–47, Feb. 1998.

[52] V. Prot, B. Skallerud, G. Sommer, and G. A. Holzapfel, “On modelling and analysis of healthy and pathological human mitral valves: Two case studies,” *J. Mech. Behav. Biomed. Mater.*, vol. 3, no. 2, pp. 167–177, Feb. 2010.

[53] T. Pham and W. Sun, “Material properties of aged human mitral valve leaflets,” *J. Biomed. Mater. Res. A*, vol. 102, no. 8, pp. 2692–2703, Aug. 2014.

[54] G. Krishnamurthy, A. Itoh, W. Bothe, J. C. Swanson, E. Kuhl, M. Karlsson, D. C. Miller, and N. B. Ingels, “Stress–strain behavior of mitral valve leaflets in the beating ovine heart,” *J. Biomech.*, vol. 42, no. 12, pp. 1909–1916, Aug. 2009.

[55] M. Stevanella, G. Krishnamurthy, E. Votta, J. C. Swanson, A. Redaelli, and N. B. Ingels, “Mitral leaflet modeling: Importance of in vivo shape and material properties,” *J. Biomech.*, vol. 44, no. 12, pp. 2229–2235, Aug. 2011.

[56] D. R. Einstein, P. Reinhall, M. Nicosia, R. P. Cochran, and K. Kunzelman, “Dynamic Finite Element Implementation of Nonlinear, Anisotropic Hyperelastic Biological Membranes,” *Comput. Methods Biomech. Biomed. Engin.*, vol. 6, no. 1, pp. 33–44, Feb. 2003.

[57] D. D. R. Einstein, K. S. Kunzelman, P. G. Reinhall, M. A. Nicosia, and R. P. Cochran, “Haemodynamic determinants of the mitral valve closure sound: A finite element study,” *Med. Biol. Eng. Comput.*, vol. 42, no. 6, pp. 832–846, Nov. 2004.

[58] V. Prot, B. Skallerud, and G. A. Holzapfel, “Transversely isotropic membrane shells with application to mitral valve mechanics. Constitutive modelling and finite element implementation,” *Int. J. Numer. Methods Eng.*, vol. 71, no. 8, pp. 987–1008, Aug. 2007.

[59] G. A. Holzapfel, G. Sommer, C. T. Gasser, and P. Regitnig, “Determination of layer-specific mechanical properties of human coronary arteries with nonatherosclerotic intimal thickening and related constitutive modeling,” *Am. J. Physiol. - Heart Circ. Physiol.*, vol. 289, no. 5, pp. H2048–H2058, Nov. 2005.

[60] M. K. Rausch, N. Famaey, T. O. Shultz, W. Bothe, D. C. Miller, and E. Kuhl, “Mechanics of the mitral valve,” *Biomech. Model. Mechanobiol.*, vol. 12, no. 5, pp. 1053–1071, Dec. 2012.

[61] R. P. Cochran, K. S. Kunzelman, C. J. Chuong, M. S. Sacks, and R. C. Eberhart, “Nondestructive Analysis of Mitral Valve Collagen Fiber Orientation,” *ASAIO Trans.*, vol. 37, no. 3, Sep. 1991.

[62] K. S. Kunzelman, D. R. Einstein, and R. P. Cochran, “Fluid-Structure Interaction Models of the Mitral Valve: Function in Normal and Pathological States,” *Philos. Trans. Biol. Sci.*, vol. 362, no. 1484, pp. 1393–1406, Aug. 2007.

[63] D. R. Einstein, F. Del Pin, X. Jiao, A. P. Kuprat, J. P. Carson, K. S. Kunzelman, R. P. Cochran, J. M. Guccione, and M. B. Ratcliffe, “Fluid-structure interactions of the mitral valve and left heart: Comprehensive strategies, past, present and future,” *Int. J. Numer. Methods Biomed. Eng.*, vol. 26, no. 3/4, pp. 348–380, Mar. 2010.

[64] K. B. Chandran and H. Kim, “Computational Mitral Valve Evaluation and Potential Clinical Applications,” *Ann. Biomed. Eng.*, vol. 43, no. 6, pp. 1348–1362, Jun. 2015.

[65] “Wiggers diagram,” *Wikipedia, the free encyclopedia*. 25-Aug-2014.

[66] M. Misfeld and H.-H. Sievers, “Heart valve macro- and microstructure,” *Philos. Trans. R. Soc. B Biol. Sci.*, vol. 362, no. 1484, pp. 1421–1436, Aug. 2007.

[67] J. M. Guccione, A. D. McCulloch, and L. K. Waldman, “Passive material properties of intact ventricular myocardium determined from a cylindrical model,” *J. Biomech. Eng.*, vol. 113, no. 1, pp. 42–55, Feb. 1991.

[68] M. R. Labrosse, C. J. Beller, T. Mesana, and J. P. Veinot, “Mechanical behavior of human aortas: Experiments, material constants and 3-D finite element modeling including residual stress,” *J. Biomech.*, vol. 42, no. 8, pp. 996–1004, May 2009.

[69] M. R. Labrosse, K. Lobo, and C. J. Beller, “Structural analysis of the natural aortic valve in dynamics: From unpressurized to physiologically loaded,” *J. Biomech.*, vol. 43, no. 10, pp. 1916–1922, Jul. 2010.

[70] C. Millington-Sanders, A. Meir, L. Lawrence, and C. Stolinski, “Structure of chordae tendineae in the left ventricle of the human heart,” *J. Anat.*, vol. 192, no. 4, pp. 573–581, May 1998.

[71] J. Ritchie, J. Jimenez, Z. He, M. S. Sacks, and A. P. Yoganathan, “The material properties of the native porcine mitral valve chordae tendineae: An in vitro investigation,” *J. Biomech.*, vol. 39, no. 6, pp. 1129–1135, 2006.

[72] J. A. Casado, S. Diego, D. Ferreño, E. Ruiz, I. Carrascal, D. Méndez, J. M. Revuelta, A. Pontón, J. M. Icardo, and F. Gutiérrez-Solana, “Determination of the mechanical

properties of normal and calcified human mitral chordae tendineae," *J. Mech. Behav. Biomed. Mater.*, vol. 13, pp. 1–13, Sep. 2012.

[73] I. Wolf, A. Eid, M. Vetter, P. Hassenpflug, and H.-P. Meinzer, "Extension of 2D segmentation methods into 3D by means of Coons-patch interpolation," 2003, pp. 1413–1420.

[74] D. Ozbag, Y. Gumusalan, and A. Demirant, "The comparative investigation of morphology of papillary muscles of left ventricle in different species," *Int. J. Clin. Pract.*, vol. 59, no. 5, pp. 529–536, May 2005.

[75] S. Gunnal, R. Wabale, and M. Farooqui, "Morphological Study of Chordae Tendinae in Human Cadaveric Hearts," *Heart Views*, vol. 16, no. 1, p. 1, 2015.

[76] I. A. Baxter, "Finite Element Modeling of the Mitral Valve and Mitral Valve Repair," 2012.

[77] P. Dagum, T. A. Timek, R. G. Green, D. Lai, G. T. M. Daughters, D. H. Liang, M. Hayase, N. B. J. Ingels, and C. D. Miller, "Coordinate-Free Analysis of Mitral Valve Dynamics in Normal and Ischemic Hearts. [Miscellaneous Article]," *Circulation*, vol. 102, no. 19, Nov. 2000.

[78] A. J. Sanfilippo, P. Harrigan, A. D. Popovic, A. E. Weyman, and R. A. Levine, "Papillary muscle traction in mitral valve prolapse: Quantitation by two-dimensional echocardiography," *J. Am. Coll. Cardiol.*, vol. 19, no. 3, pp. 564–571, Mar. 1992.

[79] Y. Sahasakul, W. D. Edwards, J. M. Naessens, and A. J. Tajik, "Age-related changes in aortic and mitral valve thickness: Implications for two-dimensional echocardiography based on an autopsy study of 200 normal human hearts," *Am. J. Cardiol.*, vol. 62, no. 7, pp. 424–430, 1988.

[80] J. R. Levick, *An Introduction to cardiovascular physiology*, 5th ed. London: Hodder Arnold, 2010.

[81] S. L. Nielsen, H. Nygaard, A. A. Fontaine, J. M. Hasenkam, S. He, N. T. Andersen, and A. P. Yoganathan, "Chordal force distribution determines systolic mitral leaflet configuration and severity of functional mitral regurgitation," *J. Am. Coll. Cardiol.*, vol. 33, no. 3, pp. 843–853, Mar. 1999.

[82] M. Ø. J. Jensen, A. A. Fontaine, and A. P. Yoganathan, "Improved In Vitro Quantification of the Force Exerted by the Papillary Muscle on the Left Ventricular Wall: Three-Dimensional Force Vector Measurement System," *Ann. Biomed. Eng.*, vol. 29, no. 5, pp. 406–413, May 2001.

[83] V. Delgado, L. F. Tops, J. D. Schuijf, A. de Roos, J. Brugada, M. J. Schalij, J. D. Thomas, and J. J. Bax, "Assessment of Mitral Valve Anatomy and Geometry With Multislice Computed Tomography," *JACC Cardiovasc. Imaging*, vol. 2, no. 5, pp. 556–565, May 2009.

Appendix A: Derivation of the Cauchy Stresses

A.1. May-Newman Strain Energy Model

The May-Newman model assumes that the strain energy function, W, is a function of the principal stretches, λ_1 and λ_2. In the following equations, the subscripts 1, 2, and 3 represent the circumferential, radial, and thickness directions, respectively.

$$W(\lambda_1, \lambda_2) = c_0(e^Q - 1) \tag{A.1}$$

$$Q = c_1(I_1 - 3)^2 + c_2(\alpha - 1)^4 \tag{A.2}$$

$$I_1 = tr\left(\bar{\bar{C}}\right) \tag{A.3}$$

$$\alpha^2 = \vec{N} \cdot \bar{\bar{C}} \cdot \vec{N} \tag{A.4}$$

Where $\vec{N}$ is a unit vector describing the orientation of the collagen fibres, and $\bar{\bar{C}}$ is the right Cauchy-Green strain tensor defined using the deformation gradient tensor, $\bar{\bar{F}}$, as follows:

$$\bar{\bar{C}} = \bar{\bar{F}}^T \cdot \bar{\bar{F}} \tag{A.5}$$

$$\bar{\bar{F}} = \begin{bmatrix} \lambda_1 & \kappa_{12} & \kappa_{13} \\ \kappa_{21} & \lambda_2 & \kappa_{23} \\ \kappa_{31} & \kappa_{32} & \lambda_3 \end{bmatrix} \tag{A.6}$$

Here λ_1 and κ_{ij} represent the principal stretch ratios and shear strains, respectively. However, the collagen fibres are assumed to be parallel to the annulus in the belly region, and as a result, no shear strains are developed. Therefore,

$$\vec{N}^T = [1\ 0\ 0] \tag{A.7}$$

$$\bar{\bar{F}} = \begin{bmatrix} \lambda_1 & 0 & 0 \\ 0 & \lambda_2 & 0 \\ 0 & 0 & \lambda_3 \end{bmatrix} \tag{A.8}$$

and,

$$\alpha = \lambda_1 \tag{A.9}$$

Consequently,

$$\bar{\bar{C}} = \begin{bmatrix} \lambda_1^2 & 0 & 0 \\ 0 & \lambda_2^2 & 0 \\ 0 & 0 & \lambda_3^2 \end{bmatrix} \tag{A.10}$$

$$I_1 = \lambda_1^2 + \lambda_2^2 + \lambda_3^2 \tag{A.11}$$

Furthermore, for an incompressible material $\det\left(\bar{\bar{F}}\right) = 1$. Therefore,

$$\lambda_3 = \frac{1}{\lambda_1 \lambda_2} \tag{A.12}$$

As a result, from Equations (A.3), (A.10), and (A.12), it can be shown that the first invariant of the right Cauchy-Green strain tensor is

$$I_1 = \lambda_1^2 + \lambda_2^2 + \frac{1}{\lambda_1^2 \lambda_2^2} \tag{A.13}$$

Therefore, substituting (A.13) and (A.9) into (A.2) we get

$$Q = c_1 \left(\lambda_1^2 + \lambda_2^2 + \frac{1}{\lambda_1^2 \lambda_2^2} - 3 \right)^2 + c_2 (\lambda_1 - 1)^4 \tag{A.14}$$

Next, the Cauchy stress tensor, $\bar{\bar{t}}$, is defined as a function of the deformation gradient tensor, $\bar{\bar{F}}$, and the 2nd Piola-Kirchoff stress tensor, $\bar{\bar{S}}$, as follows:

$$\bar{\bar{t}} = \frac{1}{J}\left(\bar{\bar{F}} \cdot \bar{\bar{S}} \cdot \bar{\bar{F}}^T\right) = \frac{1}{J}\left(\bar{\bar{F}} \cdot \frac{\partial W}{\partial E_{ij}} \cdot \bar{\bar{F}}^T\right) \tag{A.15}$$

where J is the determinant of $\bar{\bar{F}}$, and the Green strain tensor, $\bar{\bar{E}}$, is a function of the right Cauchy-Green strain tensor, and the identity tensor, $\bar{\bar{I}}$.

$$\bar{\bar{E}} = \frac{1}{2}\left(\bar{\bar{C}} - \bar{\bar{I}}\right) = \frac{1}{2}\begin{bmatrix} \lambda_1^2 - 1 & 0 & 0 \\ 0 & \lambda_2^2 - 1 & 0 \\ 0 & 0 & \dfrac{1}{\lambda_1^2\lambda_2^2} - 1 \end{bmatrix} \tag{A.16}$$

Furthermore, using the multivariable chain rule and substituting $\mathrm{J} = \det\left(\bar{\bar{F}}\right) = 1$ for an incompressible material, the Cauchy stress tensor can be expressed as follows:

$$\bar{\bar{t}} = \lambda_i^2 \frac{\partial W}{\partial Q}\frac{\partial Q}{\partial \lambda_i}\frac{\partial \lambda_i}{\partial E_{ii}} \tag{A.17}$$

where

$$\frac{\partial W}{\partial Q} = c_0 e^Q \tag{A.18}$$

$$\frac{\partial Q}{\partial \lambda_1} = 2c_1(\lambda_1^2 + \lambda_2^2 + \lambda_1^{-2}\lambda_2^{-2} - 3)(2\lambda_1 - 2\lambda_1^{-3}\lambda_2^{-2}) + 4c_2(\lambda_1 - 1)^3 \tag{A.19}$$

$$\frac{\partial Q}{\partial \lambda_2} = 2c_1(\lambda_1^2 + \lambda_2^2 + \lambda_1^{-2}\lambda_2^{-2} - 3)(2\lambda_2 - 2\lambda_1^{-2}\lambda_2^{-3}) \tag{A.20}$$

$$\frac{\partial \lambda_i}{\partial E_{ii}} = \frac{1}{\lambda_i} \tag{A.21}$$

Therefore, the principal Cauchy stresses in the circumferential and radial directions are

$$t_{11} = 4\lambda_1 c_0 e^Q[c_1(\lambda_1^2 + \lambda_2^2 + \lambda_1^{-2}\lambda_2^{-2} - 3)(\lambda_1 - \lambda_1^{-3}\lambda_2^{-2}) + c_2(\lambda_1 - 1)^3] \tag{A.22}$$

$$t_{22} = 4\lambda_2 c_0 c_1 e^Q(\lambda_1^2 + \lambda_2^2 + \lambda_1^{-2}\lambda_2^{-2} - 3)(\lambda_2 - \lambda_1^{-2}\lambda_2^{-3}) \tag{A.23}$$

Finally, from the thin membrane assumption, no stresses develop across the thickness of the tissue sample, therefore $t_{33} = 0$, and since the shear stresses are assumed to be negligible the Cauchy shear stresses are also zero.

A.2. LS-DYNA (Guccione) Strain Energy Model

The Guccione model employed by LS-DYNA in the material model MAT_HEART_TISSUE is very similar to the model implemented by May-Newman *et al.* that was covered in Appendix A.1. Therefore, many of the same assumptions will be employed when deriving the Cauchy stresses. Specifically, the shear strains and stresses are assumed to be negligible again, and the tissue is assumed to be incompressible. The main difference between the May-Newman model and the Guccione strain energy model is that the Guccione model is defined as a function of the Green strain tensor, $\bar{\bar{E}}$, as follows:

$$W(\bar{\bar{E}}) = \frac{c}{2}(e^{Q} - 1) + \frac{p}{2}(I_3 - 1) \tag{A.24}$$

$$Q = b_1 E_{11}^2 + b_2(E_{22}^2 + E_{33}^2 + E_{23}^2 + E_{32}^2) + b_3(E_{12}^2 + E_{21}^2 + E_{13}^2 + E_{31}^2) \tag{A.25}$$

where p is a Lagrange multiplier used to enforce the incompressibility constraint, and I_3 is the third invariant of the right Cauchy-Green strain tensor.

$$I_3 = \det(\bar{\bar{C}}) = \lambda_1^2 \lambda_2^2 \lambda_3^2 \tag{A.26}$$

By applying the incompressibility constraint ($I_3 = 1$), λ_3 can be defined as a function of the first two principal stresses, such that $\lambda_3 = \lambda_1^{-1}\lambda_2^{-1}$. As was covered in Appendix A.1, the principal Cauchy stresses are defined as

$$t_{ii} = \lambda_i^2 \frac{\partial W}{\partial Q} \frac{\partial Q}{\partial \lambda_i} \frac{\partial \lambda_i}{\partial E_{ii}} \tag{A.27}$$

where

$$\frac{\partial W}{\partial Q} = \frac{c}{2} e^{Q} \tag{A.28}$$

$$\frac{\partial Q}{\partial \lambda_1} = b_1\lambda_1(\lambda_1^2 - 1) - b_2\frac{\lambda_1^{-2}\lambda_2^{-2} - 1}{\lambda_1^3\lambda_2^2} \tag{A.29}$$

$$\frac{\partial Q}{\partial \lambda_2} = b_2\left[\lambda_2(\lambda_2^2 - 1) - \frac{\lambda_1^{-2}\lambda_2^{-2} - 1}{\lambda_1^2\lambda_2^3}\right] \tag{A.30}$$

$$\frac{\partial \lambda_i}{\partial E_{ii}} = \frac{1}{\lambda_i} \tag{A.31}$$

Therefore, the Cauchy stresses in the circumferential and radial directions are

$$t_{11} = \frac{c\lambda_1}{2}e^Q[b_1\lambda_1(\lambda_1^2 - 1) + b_2(\lambda_1^{-3}\lambda_2^{-2} - \lambda_1^{-5}\lambda_2^{-4})] \tag{A.32}$$

$$t_{22} = \frac{c\lambda_2}{2}e^Q b_2[\lambda_2(\lambda_2^2 - 1) + \lambda_1^{-2}\lambda_2^{-3} - \lambda_1^{-4}\lambda_2^{-5}] \tag{A.33}$$

where

$$Q = b_1\left[\frac{1}{2}(\lambda_1^2 - 1)\right]^2 + \frac{b_2}{4}[(\lambda_2^2 - 1)^2 + (\lambda_1^{-2}\lambda_2^{-2} - 1)^2] \tag{A.34}$$

and because of the thin membrane and the negligible shear stress assumptions, all other Cauchy stresses are zero.

A.3. Fung Strain Energy Model

The Fung strain energy model was employed by Pham *et al.* in their study of diseased human mitral valves [53]. As with the previous two models, the shear stress is assumed to be negligible and the tissue samples are assumed to be incompressible. As was the case with the Guccione model, the strain energy model is defined as a function of the Green strain tensor.

$$W(\bar{\bar{E}}) = \frac{c}{2}(e^Q - 1) \tag{A.35}$$

$$Q = A_1E_{11}^2 + A_2E_{22}^2 + 2A_3E_{11}E_{22} + A_4E_{12}^2 + 2A_5E_{11}E_{12} + 2A_6E_{22}E_{12} \tag{A.36}$$

Assuming negligible shear stress, the exponent, Q, is simplified to

$$Q = A_1E_{11}^2 + A_2E_{22}^2 + 2A_3E_{11}E_{22} \tag{A.37}$$

As in Appendix A.1, the principal Cauchy stresses are

$$t_{ii} = \lambda_i^2 \frac{\partial W}{\partial Q}\frac{\partial Q}{\partial \lambda_i}\frac{\partial \lambda_i}{\partial E_{ii}} \tag{A.38}$$

where

$$\frac{\partial W}{\partial Q} = \frac{c}{2}e^Q \tag{A.39}$$

$$\frac{\partial Q}{\partial \lambda_1} = A_1\lambda_1(\lambda_1^2 - 1) + A_3\lambda_1(\lambda_2^2 - 1) \tag{A.40}$$

$$\frac{\partial Q}{\partial \lambda_2} = A_2\lambda_2(\lambda_2^2 - 1) + A_3\lambda_2(\lambda_1^2 - 1) \tag{A.41}$$

$$\frac{\partial \lambda_i}{\partial E_{ii}} = \frac{1}{\lambda_i} \tag{A.42}$$

Therefore, the Cauchy stresses in the circumferential and radial directions are

$$t_{11} = \frac{\lambda_1^2 c e^Q}{2}[A_1(\lambda_1^2 - 1) + A_3(\lambda_2^2 - 1)] \tag{A.43}$$

$$t_{22} = \frac{\lambda_2^2 c e^Q}{2}[A_2(\lambda_2^2 - 1) + A_3(\lambda_1^2 - 1)] \tag{A.44}$$

respectively, and the remaining Cauchy stresses are zero due to the thin membrane and negligible shear stress assumptions.

Appendix B: MATLAB Programs

B.1. LS-DYNA Simulated Biaxial Tensile Test Input File

```
function run_LSDYNA(constants,part,npart,Nodes,Elements,Dim,BC)
savefile = 'LSDynaInputBox.dyn';
fid = fopen(savefile, 'wt');
fprintf(fid, '*KEYWORD\n');
fprintf(fid, '$---+----1----+----2----+----3----+----4----+----5----+----
6----+----7----+----8\n');
fprintf(fid, '$                    TITLE CARD\n');
fprintf(fid, '$---+----1----+----2----+----3----+----4----+----5----+----
6----+----7----+----8\n');
fprintf(fid, '*TITLE\n');
fprintf(fid, 'Mitral valve\n');
fprintf(fid, '$---+----1----+----2----+----3----+----4----+----5----+----
6----+----7----+----8\n');
fprintf(fid, '$                    CONTROL CARDS\n');
fprintf(fid, '$---+----1----+----2----+----3----+----4----+----5----+----
6----+----7----+----8\n');
fprintf(fid, '*CONTROL_TERMINATION\n');
fprintf(fid, '$   ENDTIM    ENDCYC     DTMIN    ENDNEG    ENDMAS\n');
fprintf(fid, '%10f         0       0.0       0.0       0.0\n',
Dim.endtime);
fprintf(fid, '*CONTROL_TIMESTEP\n');
fprintf(fid, '$   DTINIT      SCFT      ISDO    TSLIMT      DTMS
LCTM     ERODE     MS1ST\n');
fprintf(fid, '      0.00       0.7         0\n');
fprintf(fid, '*CONTROL_HOURGLASS\n');
fprintf(fid, '$      IHQ        QH\n');
fprintf(fid, '         1       0.1\n');
fprintf(fid, '*CONTROL_BULK_VISCOSITY\n');
fprintf(fid, '$       Q2        Q1\n');
fprintf(fid, ' 0.150E+01 0.600E-01\n');
fprintf(fid, '*CONTROL_OUTPUT\n');
fprintf(fid, '$    NPOPT    NEECHO    NREFUP    IACCOP     OPIFS
IPNINT    IKEDIT\n');
fprintf(fid, '         0         0         0         0 0.000E+00
0        0\n');
fprintf(fid, '*CONTROL_ENERGY\n');
fprintf(fid, '$     HGEN      RWEN    SLNTEN     RYLEN\n');
fprintf(fid, '         1         2         1         1\n');
fprintf(fid, '$---+----1----+----2----+----3----+----4----+----5----+----
6----+----7----+----8\n');
fprintf(fid, '$                    DATABASE CONTROL CARDS FOR ASCII
FILE\n');
fprintf(fid, '$---+----1----+----2----+----3----+----4----+----5----+----
6----+----7----+----8\n');
fprintf(fid, '*DATABASE_GLSTAT\n');
fprintf(fid, '   0.12E-3\n');
fprintf(fid, '*DATABASE_RCFORC\n');
fprintf(fid, '   0.12E-3\n');
fprintf(fid, '$---+----1----+----2----+----3----+----4----+----5----+----
6----+----7----+----8\n');
```

```
fprintf(fid, '$                    DATABASE CONTROL CARDS FOR BINARY
FILE\n');
fprintf(fid, '$---+----1----+----2----+----3----+----4----+----5----+----
6----+----7----+----8\n');
fprintf(fid, '*DATABASE_BINARY_D3PLOT\n');
fprintf(fid, '%10f \n', Dim.TimeStep);
fprintf(fid, '*DATABASE_BINARY_D3THDT\n');
fprintf(fid, '%10f \n', Dim.TimeStep);
fprintf(fid, '*DATABASE_BINARY_INTFOR\n');
fprintf(fid, '%10f \n', Dim.TimeStep);
fprintf(fid, '*DATABASE_EXTENT_BINARY\n');
fprintf(fid, '         0         0         3         0         1
1         1         1\n');
fprintf(fid, '         0         0         0         0         0
0\n');
fprintf(fid, '$---+----1----+----2----+----3----+----4----+----5----+----
6----+----7----+----8\n');
fprintf(fid, '$                    DEFINE PARTS CARDS\n');
fprintf(fid, '$---+----1----+----2----+----3----+----4----+----5----+----
6----+----7----+----8\n');
for i = 1:npart
   fprintf(fid, '*PART\n');
   fprintf(fid, '$ HEADING\n');
   fprintf(fid, ' PART PID =      %2i PART NAME : %s\n',
i,char(part(i)));
   fprintf(fid, '$      PID       SID       MID     EOSID      HGID
GRAV    ADPOPT      TMID\n');
   fprintf(fid, '%10i %9i %9i\n', i,i,i);
end
fprintf(fid, '$---+----1----+----2----+----3----+----4----+----5----+----
6----+----7----+----8\n');
fprintf(fid, '$                    MATERIAL CARDS\n');
fprintf(fid, '$---+----1----+----2----+----3----+----4----+----5----+----
6----+----7----+----8\n');
for i = 1:npart
   fprintf(fid, '*MAT_HEART_TISSUE\n');
   fprintf(fid, '$ MATERIAL NAME :%s\n', char(part(i)));
   fprintf(fid, '$      MID        RO         C        B1        B2
B3        P\n');
   fprintf(fid, '%10i %9.2E %9.2E %9.2E %9.2E %9.2E %9.2E \n', i,1.06E-
9,constants(1),constants(2),constants(3),constants(4),constants(5));
   fprintf(fid, '$     AOPT\n');
   fprintf(fid, '         0\n');
   fprintf(fid, '$       XP        YP        ZP        A1        A2
A3\n\n');
   fprintf(fid, '$       V1        V2        V3        D1        D2
D3      BETA\n\n');
end
fprintf(fid, '$---+----1----+----2----+----3----+----4----+----5----+----
6----+----7----+----8\n');
fprintf(fid, '$                    SECTION CARDS\n');
fprintf(fid, '$---+----1----+----2----+----3----+----4----+----5----+----
6----+----7----+----8\n');
for i = 1:npart
   fprintf(fid, '*SECTION_SOLID\n');
   fprintf(fid, '$    SECID    ELFORM       AET\n');
```

```
   fprintf(fid, '%10i %9i\n', i,1); % 1 means constant stress elements; 2
would mean constant pressure elements
end
fprintf(fid, '$---+----1----+----2----+----3----+----4----+----5----+----
6----+----7----+----8\n');
fprintf(fid, '$                     (8) NODAL POINT CARDS\n');
fprintf(fid, '$---+----1----+----2----+----3----+----4----+----5----+----
6----+----7----+----8\n');
fprintf(fid, '*NODE\n');
fprintf(fid, '$   NODE               X               Y               Z
TC      RC\n');
for i = 1:Dim.Nnodes
    fprintf(fid, '%8i %15.9f %15.9f
%15.9f\n',Nodes(i,1),Nodes(i,2),Nodes(i,3),Nodes(i,4));
end
fprintf(fid, '$---+----1----+----2----+----3----+----4----+----5----+----
6----+----7----+----8\n');
fprintf(fid, '$                     (11) SOLID ELEMENT CARDS\n');
fprintf(fid, '$---+----1----+----2----+----3----+----4----+----5----+----
6----+----7----+----8\n');
fprintf(fid, '*ELEMENT_SOLID\n');
fprintf(fid, '$    EID     PID      N1      N2      N3      N4      N5
N6      N7      N8\n');
for i = 1:Dim.NEl
    pid = 1;
    fprintf(fid, '%8i %7i %7i %7i %7i %7i %7i %7i %7i
%7i\n',Elements(i,1),pid,Elements(i,2),Elements(i,3),Elements(i,4),Elemen
ts(i,5),Elements(i,6),Elements(i,7),Elements(i,8),Elements(i,9));
end
fprintf(fid, '$---+----1----+----2----+----3----+----4----+----5----+----
6----+----7----+----8\n');
fprintf(fid, '$                    BOUNDARY CONDITION CARDS\n');
fprintf(fid, '$---+----1----+----2----+----3----+----4----+----5----+----
6----+----7----+----8\n');
%constrain motion at nodes on x and y axes
fprintf(fid, '*BOUNDARY_SPC_NODE\n');
fprintf(fid, '$ NID/NSID       CID      DOFX      DOFY      DOFZ
DOFRX     DOFRY     DOFRZ\n');
fprintf(fid, '%10i %9i %9i %9i %9i \n',BC.Cnode(1),0,1,1,1);     % no x,
y or z displacements at origin
for i=2:Dim.MeshZ
   fprintf(fid, '%10i %9i %9i %9i %9i \n',BC.Cnode(i),0,1,1,0);     % no
x or y displacements
end
for i = 1:Dim.MeshX-1
    fprintf(fid, '%10i %9i %9i %9i %9i \n',BC.Bnode(i),0,0,1,1);     % no
y or z displacements
end
for i = Dim.MeshX:BC.nBnode
    fprintf(fid, '%10i %9i %9i %9i %9i \n',BC.Bnode(i),0,0,1,0);     % no
y displacements
end
for i = 1:Dim.MeshY-1
    fprintf(fid, '%10i %9i %9i %9i %9i \n',BC.Lnode(i),0,1,0,1);     % no
x or z displacements
end
for i = Dim.MeshY:BC.nLnode
```

```
    fprintf(fid, '%10i %9i %9i %9i %9i \n',BC.Lnode(i),0,1,0,0);     % no
x displacements
end
for i = 1:Dim.MeshX
    fprintf(fid, '%10i %9i %9i %9i %9i \n',BC.Tnode(i),0,0,0,1);     % no
z displacements
end
for i = 1:Dim.MeshY
    fprintf(fid, '%10i %9i %9i %9i %9i \n',BC.Rnode(i),0,0,0,1);     % no
z displacements
end
fprintf(fid, '*BOUNDARY_PRESCRIBED_MOTION_NODE\n');
fprintf(fid, '$      NID       DOF       VAD      LCID        SF
VID     DEATH     BIRTH\n');
%displacement in y-direction
for i = 1:BC.nTnode
    fprintf(fid, '%10i %9i %9i %9i %9f
%9i\n',BC.Tnode(i),4,2,1,0.100E+01,i);   % -4: movement on plane
perpendicular to vector VID is not permitted; 4:it is permitted
end
%displacement in x-direction
for i = 1:BC.nRnode
    fprintf(fid, '%10i %9i %9i %9i %9f
%9i\n',BC.Rnode(i),4,2,2,0.100E+01,BC.nTnode+i);   % -4: movement on
plane perpendicular to vector VID is not permitted; 4:it is permitted
end
fprintf(fid, '*DEFINE_VECTOR\n');
fprintf(fid, '$      VID        XT        YT        ZT        XH
YH        ZH\n');
for i=1:BC.nTnode
    ii=BC.Tnode(i);
    fprintf(fid, '%10i %9.4f %9.4f %9.4f %9.4f %9.4f
%9.4f\n',i,Nodes(ii,2),Nodes(ii,3),Nodes(ii,4),Nodes(ii,2),Nodes(ii,3)+10
0,Nodes(ii,4));
end
for i=1:BC.nRnode
    ii=BC.Rnode(i);
    fprintf(fid, '%10i %9.4f %9.4f %9.4f %9.4f %9.4f
%9.4f\n',BC.nTnode+i,Nodes(ii,2),Nodes(ii,3),Nodes(ii,4),Nodes(ii,2)+100,
Nodes(ii,3),Nodes(ii,4));
end

%Define edge node displacements
fprintf(fid, '*DEFINE_CURVE\n');
fprintf(fid, '$     LCID      SIDR      SCLA      SCLO      OFFA
OFFO\n');
fprintf(fid, '%10i %9i\n',1,0);
fprintf(fid, '$                A1                  O1\n');
fprintf(fid, '      0.00000000E+00      0.00000000E+00\n');
fprintf(fid, '      %14.9f
%14.9f\n',(Dim.endtime+Dim.TimeStep),Dim.XBox*(Dim.MaxStretchY-1));
fprintf(fid, '*DEFINE_CURVE\n');
fprintf(fid, '$     LCID      SIDR      SCLA      SCLO      OFFA
OFFO\n');
fprintf(fid, '%10i %9i\n',2,0);
fprintf(fid, '$                A1                  O1\n');
fprintf(fid, '      0.00000000E+00      0.00000000E+00\n');
```

```
fprintf(fid, '      %14.9f
%14.9f\n',(Dim.endtime+Dim.TimeStep),Dim.XBox*(Dim.MaxStretchX-1));
fprintf(fid, '*END\n');
fclose(fid);
command = strcat('C:\LSDYNA\program\ls971_s_R5.1.1_winx64_p.exe
I="C:\Users\chris\Documents\MATLAB\LSDynaInputBox.dyn" S="intfor"');
system(command);
end
```

B.2. LS-DYNA Simulated Pressure Test Input File

```
function run_LSDYNA(constants,P,part,npart,Nodes,Dim,BCnode)
savefile = 'LSDynaInputBoxP.dyn';
fid = fopen(savefile, 'wt');
fprintf(fid, '*KEYWORD\n');
fprintf(fid, '$---+----1----+----2----+----3----+----4----+----5----+----
6----+----7----+----8\n');
fprintf(fid, '$                    TITLE CARD\n');
fprintf(fid, '$---+----1----+----2----+----3----+----4----+----5----+----
6----+----7----+----8\n');
fprintf(fid, '*TITLE\n');
fprintf(fid, 'Mitral valve\n');
fprintf(fid, '$---+----1----+----2----+----3----+----4----+----5----+----
6----+----7----+----8\n');
fprintf(fid, '$                    CONTROL CARDS\n');
fprintf(fid, '$---+----1----+----2----+----3----+----4----+----5----+----
6----+----7----+----8\n');
fprintf(fid, '*CONTROL_TERMINATION\n');
fprintf(fid, '$   ENDTIM    ENDCYC     DTMIN    ENDNEG    ENDMAS\n');
fprintf(fid, '%10f         0       0.0       0.0       0.0\n',
Dim.endtime);
fprintf(fid, '*CONTROL_TIMESTEP\n');
fprintf(fid, '$   DTINIT      SCFT      ISDO    TSLIMT      DTMS
LCTM     ERODE     MS1ST\n');
fprintf(fid, '      0.00       0.9         0\n');
fprintf(fid, '*CONTROL_HOURGLASS\n');
fprintf(fid, '$      IHQ        QH\n');
fprintf(fid, '         1       0.1\n');
fprintf(fid, '*CONTROL_BULK_VISCOSITY\n');
fprintf(fid, '$       Q2        Q1\n');
fprintf(fid, ' 0.150E+01 0.600E-01\n');
fprintf(fid, '*CONTROL_OUTPUT\n');
fprintf(fid, '$    NPOPT    NEECHO    NREFUP    IACCOP     OPIFS
IPNINT    IKEDIT\n');
fprintf(fid, '         0         0         0         0 0.000E+00
0         0\n');
fprintf(fid, '*CONTROL_ENERGY\n');
fprintf(fid, '$     HGEN      RWEN    SLNTEN     RYLEN\n');
fprintf(fid, '         1         2         1         1\n');
fprintf(fid, '$---+----1----+----2----+----3----+----4----+----5----+----
6----+----7----+----8\n');
fprintf(fid, '$                    DATABASE CONTROL CARDS FOR ASCII
FILE\n');
fprintf(fid, '$---+----1----+----2----+----3----+----4----+----5----+----
6----+----7----+----8\n');
fprintf(fid, '*DATABASE_GLSTAT\n');
```

```
fprintf(fid, '   0.12E-3\n');
fprintf(fid, '*DATABASE_RCFORC\n');
fprintf(fid, '   0.12E-3\n');
fprintf(fid, '$---+----1----+----2----+----3----+----4----+----5----+----
6----+----7----+----8\n');
fprintf(fid, '$                    DATABASE CONTROL CARDS FOR BINARY
FILE\n');
fprintf(fid, '$---+----1----+----2----+----3----+----4----+----5----+----
6----+----7----+----8\n');
fprintf(fid, '*DATABASE_BINARY_D3PLOT\n');
fprintf(fid, '%10f \n', Dim.TimeStep);%0.54/Dim.timescale*0.9999/200);  %
this time step needs to be preserved so that GOA analysis stays the same
fprintf(fid, '*DATABASE_BINARY_D3THDT\n');
fprintf(fid, '%10f \n', Dim.TimeStep);%0.54/Dim.timescale*0.9999/200);
fprintf(fid, '*DATABASE_BINARY_INTFOR\n');
fprintf(fid, '%10f \n', Dim.TimeStep);%0.54/Dim.timescale*0.9999/200);
fprintf(fid, '*DATABASE_EXTENT_BINARY\n');
fprintf(fid, '         0         0         3         0         1
1         1         1\n');
fprintf(fid, '         0         0         0         0         0
0\n');
fprintf(fid, '$---+----1----+----2----+----3----+----4----+----5----+----
6----+----7----+----8\n');
fprintf(fid, '$                    DEFINE PARTS CARDS\n');
fprintf(fid, '$---+----1----+----2----+----3----+----4----+----5----+----
6----+----7----+----8\n');
for i = 1:npart
   fprintf(fid, '*PART\n');
   fprintf(fid, '$ HEADING\n');
   fprintf(fid, ' PART PID =      %2i PART NAME : %s\n',
i,char(part(i)));
   fprintf(fid, '$      PID       SID       MID     EOSID      HGID
GRAV    ADPOPT      TMID\n');
   fprintf(fid, '%10i %9i %9i\n', i,i,i);
end
fprintf(fid, '$---+----1----+----2----+----3----+----4----+----5----+----
6----+----7----+----8\n');
fprintf(fid, '$                    MATERIAL CARDS\n');
fprintf(fid, '$---+----1----+----2----+----3----+----4----+----5----+----
6----+----7----+----8\n');
for i = 1:npart
   fprintf(fid, '*MAT_HEART_TISSUE\n');
   fprintf(fid, '$ MATERIAL NAME :%s\n', char(part(i)));
   fprintf(fid, '$      MID        RO         C        B1        B2
B3        P\n');
   fprintf(fid, '%10i %9.2E %9.2E %9.2E %9.2E %9.2E %9.2E \n', i,0.1E-
8,constants(1),constants(2),constants(3),constants(4),P);
   fprintf(fid, '$     AOPT\n');
   fprintf(fid, '         0\n');
   fprintf(fid, '$       XP        YP        ZP        A1        A2
A3\n\n');
   fprintf(fid, '$       V1        V2        V3        D1        D2
D3      BETA\n\n');
end
fprintf(fid, '$---+----1----+----2----+----3----+----4----+----5----+----
6----+----7----+----8\n');
fprintf(fid, '$                    SECTION CARDS\n');
```

```
fprintf(fid, '$---+----1----+----2----+----3----+----4----+----5----+----
6----+----7----+----8\n');
for i = 1:npart
   fprintf(fid, '*SECTION_SOLID\n');
   fprintf(fid, '$    SECID    ELFORM       AET\n');
   fprintf(fid, '%10i %9i\n', i,1); % 1 means constant stress elements; 2
would mean constant pressure elements
end
fprintf(fid, '$---+----1----+----2----+----3----+----4----+----5----+----
6----+----7----+----8\n');
fprintf(fid, '$                     (8) NODAL POINT CARDS\n');
fprintf(fid, '$---+----1----+----2----+----3----+----4----+----5----+----
6----+----7----+----8\n');
fprintf(fid, '*NODE\n');
fprintf(fid, '$   NODE               X               Y               Z
TC      RC\n');
for i = 1:Dim.Nnodes
    fprintf(fid, '%8i %15.9f %15.9f
%15.9f\n',Nodes(i,1),Nodes(i,2),Nodes(i,3),Nodes(i,4));
end
fprintf(fid, '$---+----1----+----2----+----3----+----4----+----5----+----
6----+----7----+----8\n');
fprintf(fid, '$                    ELEMENT CARDS\n');
fprintf(fid, '$---+----1----+----2----+----3----+----4----+----5----+----
6----+----7----+----8\n');
fprintf(fid, '*ELEMENT_SOLID\n');
fprintf(fid, '$    EID     PID      N1      N2      N3      N4      N5
N6      N7      N8\n');
for i = 1:Dim.NEl
    pid = 1;
    fprintf(fid, '%8i %7i %7i %7i %7i %7i %7i %7i %7i
%7i\n',Dim.Elements(i,1),pid,Dim.Elements(i,2),Dim.Elements(i,3),Dim.Elem
ents(i,4),Dim.Elements(i,5),Dim.Elements(i,6),Dim.Elements(i,7),Dim.Eleme
nts(i,8),Dim.Elements(i,9));
end
fprintf(fid, '*LOAD_SEGMENT\n');
fprintf(fid, '$     LCID        SF        AT        N1        N2
N3        N4\n');
for i = 1:Dim.NSEl
    fprintf(fid, '%10i %9.1f %9.1i %9i %9i %9i
%9i\n',1,1,0,Dim.SElements(i,2),Dim.SElements(i,3),Dim.SElements(i,4),Dim
.SElements(i,5));
end
fprintf(fid, '$---+----1----+----2----+----3----+----4----+----5----+----
6----+----7----+----8\n');
fprintf(fid, '$                    BOUNDARY CONDITION CARDS\n');
fprintf(fid, '$---+----1----+----2----+----3----+----4----+----5----+----
6----+----7----+----8\n');
%constrain motion at nodes on x and y axes
fprintf(fid, '*BOUNDARY_SPC_NODE\n');
fprintf(fid, '$ NID/NSID       CID      DOFX      DOFY      DOFZ
DOFRX     DOFRY     DOFRZ\n');
for i=1:Dim.NBCnodes
   fprintf(fid, '%10i %9i %9i %9i %9i \n',BCnode(i,1),0,1,1,1);     % no
x, y or z displacements
end
%Define pressure curve
```

```
fprintf(fid, '*DEFINE_CURVE\n');
fprintf(fid, '$     LCID      SIDR      SCLA      SCLO      OFFA
OFFO\n');
fprintf(fid, '%10i %9i\n',1,0);
fprintf(fid, '$                 A1                  O1\n');
fprintf(fid, '%20.9E      -.00000000E+00\n',0);
fprintf(fid, '%20.9E      -.66499997E-04\n',.500000024E-
02/Dim.timescale);
fprintf(fid, '%20.9E      -.00000000E+00\n',.130000000E-
01/Dim.timescale);
fprintf(fid, '%20.9E      0.11969999E-03\n',.270000007E-
01/Dim.timescale);
fprintf(fid, '%20.9E      0.12236000E-02\n',.439999998E-
01/Dim.timescale);
fprintf(fid, '%20.9E      0.60913996E-02\n',.620000018E-
01/Dim.timescale);
fprintf(fid, '%20.9E      0.10600099E-01\n',.800000038E-
01/Dim.timescale);
fprintf(fid, '%20.9E      0.13100500E-01\n',.980000012E-
01/Dim.timescale);
fprintf(fid, '%20.9E      0.15228499E-01\n',.147000002E-
00/Dim.timescale);
fprintf(fid, '%20.9E      0.16079700E-01\n',.199999996E-
00/Dim.timescale);
fprintf(fid, '%20.9E      0.15228499E-01\n',.256999992E-
00/Dim.timescale);
fprintf(fid, '%20.9E      0.13526100E-01\n',.302000009E-
00/Dim.timescale);
fprintf(fid, '%20.9E      0.11145400E-01\n',.315999985E-
00/Dim.timescale);
fprintf(fid, '%20.9E      -.30590000E-03\n',.368999988E-
00/Dim.timescale);
fprintf(fid, '%20.9E      -.35910000E-03\n',.399999991E-
00/Dim.timescale);
fprintf(fid, '%20.9E      -.66499997E-04\n',.430999994E-
00/Dim.timescale);
fprintf(fid, '%20.9E      -.66499997E-04\n',.500000007E-
00/Dim.timescale);
fprintf(fid, '*END\n');
fclose(fid);
command = strcat('C:\LSDYNA\program\ls971_s_R5.1.1_winx64_p.exe
I="C:\Users\chris\Documents\MATLAB\LSDynaInputBoxP.dyn" S="intfor"');
system(command);
end
```

B.3. LS-DYNA Mitral Valve Simulation Input File

```
function InputDeck(xn,yn,zn,MV)

% Writing the LS_Dyna input file for the problem
par.sutures=0;
par.npart=5;
part = cell(1,par.npart);
part(1) = cellstr('ALeaflet');
part(2) = cellstr('PLeaflet');
part(3) = cellstr('AChordae');
```

```
part(4) = cellstr('PChordae');
if par.sutures == 1
    part(5) = cellstr('Sutures');
end
date=datestr(now,'dd-mmm-yyyy HHMMSS');
savefile = [handles.source,handles.FolderName,' LSDYNA Input ',date,
'.dyn'];
fid = fopen(savefile, 'wt');
fprintf(fid, '*KEYWORD\n');
fprintf(fid, '$---+----1----+----2----+----3----+----4----+----5----+----
6----+----7----+----8\n');
fprintf(fid, '$                    TITLE CARD\n');
fprintf(fid, '$---+----1----+----2----+----3----+----4----+----5----+----
6----+----7----+----8\n');
fprintf(fid, '*TITLE\n');
fprintf(fid, '%s\n',handles.FolderName);
fprintf(fid, '$---+----1----+----2----+----3----+----4----+----5----+----
6----+----7----+----8\n');
fprintf(fid, '$                    CONTROL CARDS\n');
fprintf(fid, '$---+----1----+----2----+----3----+----4----+----5----+----
6----+----7----+----8\n');
fprintf(fid, '*CONTROL_TERMINATION\n');
fprintf(fid, '$   ENDTIM    ENDCYC     DTMIN    ENDNEG    ENDMAS\n');
fprintf(fid, ' 0.500E-01         0       0.0       0.0       0.0\n');
fprintf(fid, '*CONTROL_TIMESTEP\n');
fprintf(fid, '$   DTINIT      SCFT      ISDO    TSLIMT      DTMS
LCTM     ERODE     MS1ST\n');
fprintf(fid, '      0.00       0.8         0\n');
fprintf(fid, '*CONTROL_HOURGLASS\n');
fprintf(fid, '$      IHQ        QH\n');
fprintf(fid, '         1       0.1\n');
fprintf(fid, '*CONTROL_BULK_VISCOSITY\n');
fprintf(fid, '$       Q2        Q1\n');
fprintf(fid, ' 0.150E+01 0.600E-01\n');
fprintf(fid, '*CONTROL_OUTPUT\n');
fprintf(fid, '$    NPOPT    NEECHO    NREFUP    IACCOP     OPIFS
IPNINT    IKEDIT\n');
fprintf(fid, '         0         0         0         0 0.000E+00
0         0\n');
fprintf(fid, '*CONTROL_ENERGY\n');
fprintf(fid, '$     HGEN      RWEN    SLNTEN     RYLEN\n');
fprintf(fid, '         1         2         1         1\n');
fprintf(fid, '*CONTROL_CONTACT\n');
fprintf(fid, '\n\n\n         2\n'); %ignore initial contact, but
penetration warnings are still printed
fprintf(fid, '$---+----1----+----2----+----3----+----4----+----5----+----
6----+----7----+----8\n');
fprintf(fid, '$                    DATABASE CONTROL CARDS FOR ASCII
FILE\n');
fprintf(fid, '$---+----1----+----2----+----3----+----4----+----5----+----
6----+----7----+----8\n');
fprintf(fid, '$*DATABASE_HISTORY_OPTION\n');
fprintf(fid, '$      ID1       ID2       ID3       ID4       ID5
ID6       ID7       ID8\n');
fprintf(fid, '$OPTION : BEAM    BEAM_SET   NODE   NODE_SET\n');
fprintf(fid, '$         SHELL   SHELL_SET  SOLID  SOLID_SET\n');
fprintf(fid, '$         TSHELL  TSHELL_SET\n');
```

```
fprintf(fid, '$*DATABASE_OPTION\n');
fprintf(fid, '$       DT\n');
fprintf(fid, '$OPTION : SECFORC RWFORC NODOUT ELOUT  GLSTAT\n');
fprintf(fid, '$         DEFORC  MATSUM NCFORC RCFORC DEFGEO\n');
fprintf(fid, '$         SPCFORC SWFORC ABSTAT NODFOR BNDOUT\n');
fprintf(fid, '$         RBDOUT  GCEOUT SLEOUT MPGS   SBTOUT\n');
fprintf(fid, '$         JNTFORC AVSFLT MOVIE\n');
fprintf(fid, '*DATABASE_GLSTAT\n');
fprintf(fid, '   0.12E-3\n');
fprintf(fid, '*DATABASE_RCFORC\n');
fprintf(fid, '   0.12E-3\n');
fprintf(fid, '$---+----1----+----2----+----3----+----4----+----5----+----
6----+----7----+----8\n');
fprintf(fid, '$                    DATABASE CONTROL CARDS FOR BINARY
FILE\n');
fprintf(fid, '$---+----1----+----2----+----3----+----4----+----5----+----
6----+----7----+----8\n');
fprintf(fid, '*DATABASE_BINARY_D3PLOT\n');
fprintf(fid, '$  DT/CYCL      LCDT      NOBEAM\n');
fprintf(fid, ' 0.100E-02\n');
fprintf(fid, '*DATABASE_BINARY_D3THDT\n');
fprintf(fid, '$  DT/CYCL      LCDT      NOBEAM\n');
fprintf(fid, ' 0.100E-02\n');
fprintf(fid, '$*DATABASE_BINARY_OPTION\n');
fprintf(fid, '$  DT/CYCL      LCDT      NOBEAM\n');
fprintf(fid, '$OPTION : D3DRFL D3DUMP RUNRSF INTFOR\n');
fprintf(fid, '*DATABASE_EXTENT_BINARY\n');
fprintf(fid, '         0         0         3         0         1
1         1         1\n');
fprintf(fid, '         0         0         0         0         0
0\n');
fprintf(fid, '$---+----1----+----2----+----3----+----4----+----5----+----
6----+----7----+----8\n');
fprintf(fid, '$                    DEFINE PARTS CARDS\n');
fprintf(fid, '$---+----1----+----2----+----3----+----4----+----5----+----
6----+----7----+----8\n');
for i = 1:4
    fprintf(fid, '*PART\n');
    fprintf(fid, '$ HEADING\n');
    fprintf(fid, ' PART PID =      %2i PART NAME : %s\n',
i,char(part(i)));
    fprintf(fid, '$      PID       SID       MID     EOSID      HGID
GRAV    ADPOPT      TMID\n');
    fprintf(fid, '%10i %9i %9i\n', i,i,i);
end
if par.sutures == 1
    fprintf(fid, '*PART\n');
    fprintf(fid, '$ HEADING\n');
    fprintf(fid, ' PART PID =      %2i PART NAME : %s\n',
6,char(part(5)));
    fprintf(fid, '$      PID       SID       MID     EOSID      HGID
GRAV    ADPOPT      TMID\n');
    fprintf(fid, '%10i %9i %9i\n', 5,5,5);
end
fprintf(fid, '$---+----1----+----2----+----3----+----4----+----5----+----
6----+----7----+----8\n');
fprintf(fid, '$                    MATERIAL CARDS\n');
```

```
fprintf(fid, '$---+----1----+----2----+----3----+----4----+----5----+----
6----+----7----+----8\n');
for i = 1:2
    fprintf(fid, '*MAT_HEART_TISSUE\n');
    fprintf(fid, '$ MATERIAL NAME :%s\n', char(part(i)));
    fprintf(fid, '$      MID        RO         C        B1        B2
B3        P\n');
    fprintf(fid, '%10i %9.2E ',i,1.06E-9);
    fprintf(fid, strrep(sprintf('%9.4E ',handles.mat_c(1,i)),'E-00','E-
'));
    if handles.mat_b1(1,i)>=100 %if b1>=100 only 5 decimal places can be
used
        fprintf(fid, '%9.5f ', handles.mat_b1(1,i));
    elseif handles.mat_b1(1,i)>=1000
        fprintf(fid, '%9.4f ', handles.mat_b1(1,i));
    else
        fprintf(fid, '%9.6f ', handles.mat_b1(1,i));
    end
    if handles.mat_b2(1,i)>=100
        fprintf(fid, '%9.5f %9.2E %9.2E \n',
handles.mat_b2(1,i),handles.mat_b3(1,i),handles.mat_p(1,i));
    elseif handles.mat_b2(1,i)>=1000
        fprintf(fid, '%9.4f %9.2E %9.2E \n',
handles.mat_b2(1,i),handles.mat_b3(1,i),handles.mat_p(1,i));
    else
        fprintf(fid, '%9.6f %9.2E %9.2E \n',
handles.mat_b2(1,i),handles.mat_b3(1,i),handles.mat_p(1,i));
    end
    fprintf(fid, '$     AOPT\n');
    fprintf(fid, '         0\n');
    fprintf(fid, '$       XP        YP        ZP        A1        A2
A3\n\n');
    fprintf(fid, '$       V1        V2        V3        D1        D2
D3      BETA\n\n');
end
fprintf(fid, '*MAT_CABLE_DISCRETE_BEAM\n');
fprintf(fid, '$MATERIAL NAME:AChordae\n');
fprintf(fid, '$      MID        RO         E     LCID       F0\n');
fprintf(fid, '         3  1.06E-09                  3\n');
fprintf(fid, '*MAT_CABLE_DISCRETE_BEAM\n');
fprintf(fid, '$MATERIAL NAME:PChordae\n');
fprintf(fid, '$      MID        RO         E     LCID       F0\n');
fprintf(fid, '         4  1.06E-09                  3\n');
fprintf(fid, '$---+----1----+----2----+----3----+----4----+----5----+----
6----+----7----+----8\n');
fprintf(fid, '$                    SECTION CARDS\n');
fprintf(fid, '$---+----1----+----2----+----3----+----4----+----5----+----
6----+----7----+----8\n');
for i = 1:2
    fprintf(fid, '*SECTION_SOLID\n');
    fprintf(fid, '$    SECID    ELFORM       AET\n');
    fprintf(fid, '%10i %9i\n', i,1); % 1 means constant stress elements;
2 would mean constant pressure elements
end
fprintf(fid, '*SECTION_BEAM\n');%Anterior chordae
fprintf(fid, '$    SECID    ELFORM      SHRF   QR/IRID       CST
SCOOR       NSM\n');
```

```
fprintf(fid, '         3         6\n');
fprintf(fid, '$      VOL      INER       CID        CA    OFFSET\n');
fprintf(fid, '           %9.2E         0 %9.5f
0\n',MV.Inertia,MV.Area);
fprintf(fid, '*SECTION_BEAM\n');%Posterior chordae
fprintf(fid, '$    SECID    ELFORM      SHRF   QR/IRID       CST
SCOOR       NSM\n');
fprintf(fid, '         4         6\n');
fprintf(fid, '$      VOL      INER       CID        CA    OFFSET\n');
fprintf(fid, '           %9.2E         0 %9.5f
0\n',MV.Inertia,MV.Area);
fprintf(fid, '$---+----1----+----2----+----3----+----4----+----5----+----
6----+----7----+----8\n');
fprintf(fid, '$                    NODAL POINT CARDS\n');
fprintf(fid, '$---+----1----+----2----+----3----+----4----+----5----+----
6----+----7----+----8\n');
fprintf(fid, '*NODE\n');
fprintf(fid, '$   NODE               X               Y               Z
TC      RC\n');
for i = 1:MV.nn
    if isnan(xn(1,i))
    else
        fprintf(fid, '%8i %15.9f %15.9f
%15.9f\n',i,xn(1,i),yn(1,i),zn(1,i));
    end
end
fprintf(fid, '$---+----1----+----2----+----3----+----4----+----5----+----
6----+----7----+----8\n');
fprintf(fid, '$                    ELEMENT CARDS\n');
fprintf(fid, '$---+----1----+----2----+----3----+----4----+----5----+----
6----+----7----+----8\n');
fprintf(fid, '*ELEMENT_SOLID\n');
fprintf(fid, '$    EID     PID      N1      N2      N3      N4      N5
N6      N7      N8\n');
for i = 1:MV.velAL
    fprintf(fid, '%8i %7i %7i %7i %7i %7i %7i %7i %7i
%7i\n',i,1,MV.vn1(i),MV.vn2(i),MV.vn3(i),MV.vn4(i),MV.vn5(i),MV.vn6(i),MV
.vn7(i),MV.vn8(i));
end
for i = MV.velAL+1:MV.velNUM
    fprintf(fid, '%8i %7i %7i %7i %7i %7i %7i %7i %7i
%7i\n',i,2,MV.vn1(i),MV.vn2(i),MV.vn3(i),MV.vn4(i),MV.vn5(i),MV.vn6(i),MV
.vn7(i),MV.vn8(i));
end
fprintf(fid, '*LOAD_SEGMENT\n');
fprintf(fid, '$     LCID        SF        AT        N1        N2
N3        N4\n');
for i = 1:MV.selNUM
    fprintf(fid, '%10i %9.1f %9.1i %9i %9i %9i
%9i\n',1,1,0,MV.sn1(i),MV.sn2(i),MV.sn3(i),MV.sn4(i));
end
fprintf(fid, '*ELEMENT_BEAM\n');
fprintf(fid, '$    EID     PID      N1      N2      N3\n');
elnum=MV.velNUM;
for i = 1:MV.ChNUM/2
    for j=1:MV.nsubel
        elnum=elnum+1;
```

```
        fprintf(fid, '%8i %7i %7i
%7i\n',elnum,3,MV.subbn1(j,i),MV.subbn1(j+1,i));
    end
    for j=1:MV.nsubel
        elnum=elnum+1;
        fprintf(fid, '%8i %7i %7i
%7i\n',elnum,3,MV.subbn2(j,i),MV.subbn2(j+1,i));
    end
    for j=1:MV.nsubel
        elnum=elnum+1;
        fprintf(fid, '%8i %7i %7i
%7i\n',elnum,3,MV.subbn3(j,i),MV.subbn3(j+1,i));
    end
end
fprintf(fid, '*ELEMENT_BEAM\n');
fprintf(fid, '$    EID     PID      N1      N2      N3\n');
for i = MV.ChNUM/2+1:MV.ChNUM
    for j=1:MV.nsubel
        elnum=elnum+1;
        fprintf(fid, '%8i %7i %7i
%7i\n',elnum,4,MV.subbn1(j,i),MV.subbn1(j+1,i));
    end
    for j=1:MV.nsubel
        elnum=elnum+1;
        fprintf(fid, '%8i %7i %7i
%7i\n',elnum,4,MV.subbn2(j,i),MV.subbn2(j+1,i));
    end
    for j=1:MV.nsubel
        elnum=elnum+1;
        fprintf(fid, '%8i %7i %7i
%7i\n',elnum,4,MV.subbn3(j,i),MV.subbn3(j+1,i));
    end
end
fprintf(fid, '$---+----1----+----2----+----3----+----4----+----5----+----
6----+----7----+----8\n');
fprintf(fid, '$                    BOUNDARY CONDITION CARDS\n');
fprintf(fid, '$---+----1----+----2----+----3----+----4----+----5----+----
6----+----7----+----8\n');
fprintf(fid, '*BOUNDARY_PRESCRIBED_MOTION_NODE\n');
fprintf(fid, '$      NID       DOF       VAD      LCID        SF
VID     DEATH     BIRTH\n');
for i = 1:MV.anNUM
    fprintf(fid, '%10i %9i %9i %9i %9.2E %9i\n',MV.ann(i),-
4,2,2,0.100E+01,i);   % -4: movement on plane perpendicular to vector VID
is not permitted; 4:it is permitted
end
fprintf(fid, '*DEFINE_VECTOR\n');
fprintf(fid, '$      VID        XT        YT        ZT        XH
YH        ZH\n');
for i=1:MV.anNUM
    ii=MV.ann(i);
    fprintf(fid, '%10i %9.4f %9.4f %9.4f %9.4f %9.4f
%9.4f\n',i,xn(1,ii),yn(1,ii),zn(1,ii),0.0,0.0,zn(1,ii));
end
%Define annulus displacements
fprintf(fid, '*DEFINE_CURVE\n');
```

```
fprintf(fid, '$     LCID      SIDR      SCLA      SCLO      OFFA
OFFO\n');
fprintf(fid, '%10i %9i\n',2,0);
fprintf(fid, '$                 A1                 O1\n');
fprintf(fid, '      .000000000E+00      0.00000000E+00\n');
fprintf(fid, '      .147000002E-01      0.17500000E+01\n');
fprintf(fid, '      .256999992E-01      0.17500000E+01\n');
fprintf(fid, '      .500000007E-01      0.00000000E+00\n');
%define left ventricular pressure curve
fprintf(fid, '*DEFINE_CURVE\n');
fprintf(fid, '$     LCID      SIDR      SCLA      SCLO      OFFA
OFFO\n');
fprintf(fid, '%10i %9i\n',1,0);
fprintf(fid, '$                 A1                 O1\n');
fprintf(fid, '      .000000000E+00      -.00000000E+00\n');
fprintf(fid, '      .500000024E-03      -.66499997E-04\n');
fprintf(fid, '      .130000000E-02      -.00000000E+00\n');
fprintf(fid, '      .270000007E-02      0.11969999E-03\n');
fprintf(fid, '      .439999998E-02      0.12236000E-02\n');
fprintf(fid, '      .620000018E-02      0.60913996E-02\n');
fprintf(fid, '      .800000038E-02      0.10600099E-01\n');
fprintf(fid, '      .980000012E-02      0.13100500E-01\n');
fprintf(fid, '      .147000002E-01      0.15228499E-01\n');
fprintf(fid, '      .199999996E-01      0.16079700E-01\n');
fprintf(fid, '      .256999992E-01      0.15228499E-01\n');
fprintf(fid, '      .302000009E-01      0.13526100E-01\n');
fprintf(fid, '      .315999985E-01      0.11145400E-01\n');
fprintf(fid, '      .368999988E-01      -.30590000E-03\n');
fprintf(fid, '      .399999991E-01      -.35910000E-03\n');
fprintf(fid, '      .430999994E-01      -.66499997E-04\n');
fprintf(fid, '      .500000007E-01      -.66499997E-04\n');
%define engineering stress-strain curve for chordae
fprintf(fid, '*DEFINE_CURVE\n');
fprintf(fid, '$     LCID      SIDR      SCLA      SCLO      OFFA
OFFO\n');
fprintf(fid, '%10i %9i\n',3,0);
fprintf(fid, '$                 A1                 O1\n');
fprintf(fid, '                  -1                   0\n');
fprintf(fid, '                   0                   0\n');
fprintf(fid, '%20.4f %19.4f\n',MV.epsilonA,MV.sigmaA);
fprintf(fid, '%20.4f %19.4f\n',MV.epsilonP,MV.sigmaP);
fprintf(fid, '%20.4f %19.4f\n',MV.epsilonR,MV.sigmaR);
%PM tip constraints
fprintf(fid, '*BOUNDARY_SPC_NODE\n');
fprintf(fid, '$ NID/NSID       CID      DOFX      DOFY      DOFZ
DOFRX     DOFRY     DOFRZ\n');
for i = MV.nLn+1:MV.nPChn
    fprintf(fid, '%10i %9i %9i %9i %9i \n',i,0,1,1,1);     % no
displacements
end
fprintf(fid, '*SET_SEGMENT\n');
fprintf(fid, '$      SID\n');
fprintf(fid, '%10i\n',1);
for i = 1:MV.celNUM
    fprintf(fid, '%10i %9i %9i %9i
\n',MV.cn1(i),MV.cn2(i),MV.cn3(i),MV.cn4(i));
end
```

```
%Contact management between atrial surfaces
fprintf(fid, '*CONTACT_AUTOMATIC_SURFACE_TO_SURFACE\n');
fprintf(fid, '$     SSID      MSID     SSTYP     MSTYP    SBOXID
MBOXID       SPR       MPR\n');
fprintf(fid, '%10i %9i %9i %9i %9i %9i %9i %9i \n',1,1,0,0,0,0,0,1);
fprintf(fid, '%10i %9i %9i %9i %9i %9i %9i %9.2E
\n\n',0,0,0,0,20,0,0,1E+20);
fprintf(fid, '*END\n');
fclose(fid);
end
end
```

Appendix C: Mitral Valve Simulation Results

C.1. Mitral Valve Dynamics

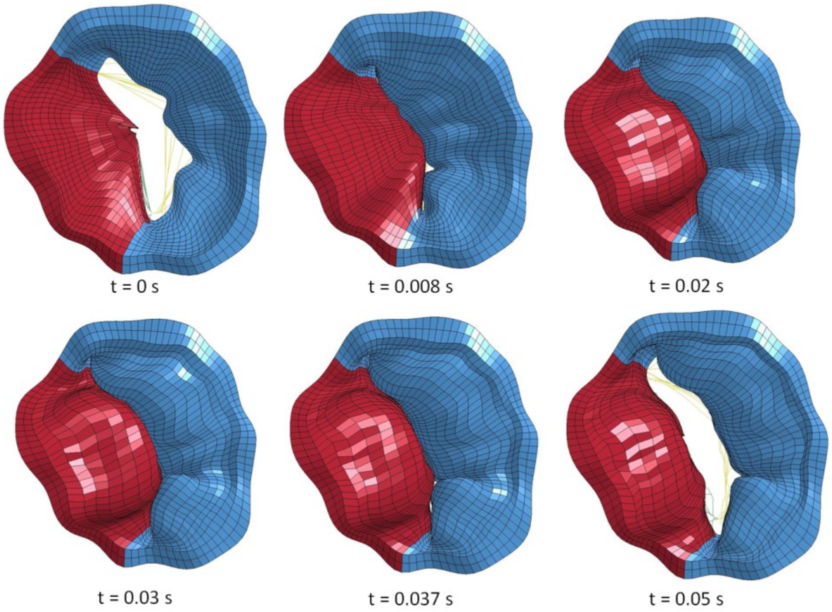

Figure C.1: Top view (from the left atrium) showing the behaviour of the healthy mitral valve model, MV1, at specific points of interest.

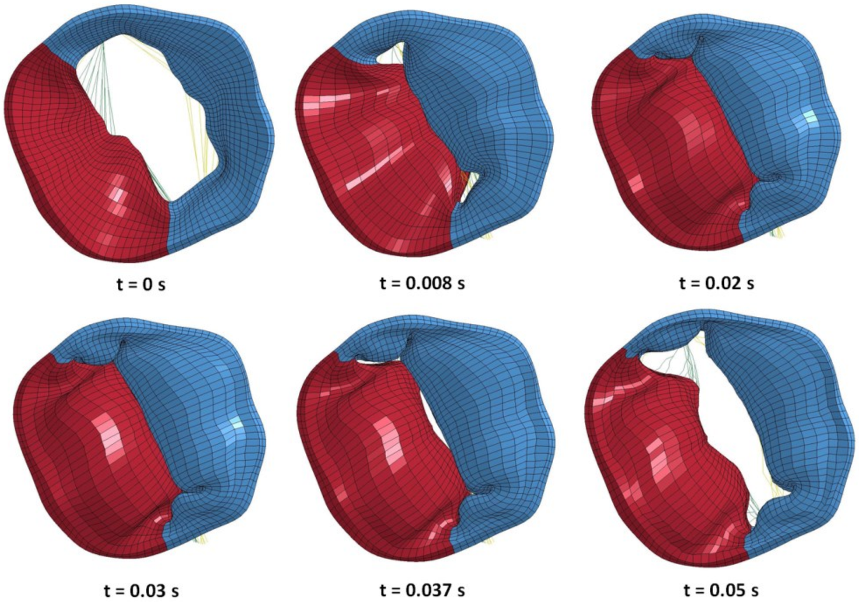

Figure C.2: Top view (from the left atrium) showing the behaviour of the healthy mitral valve model, MV3, at specific points of interest.

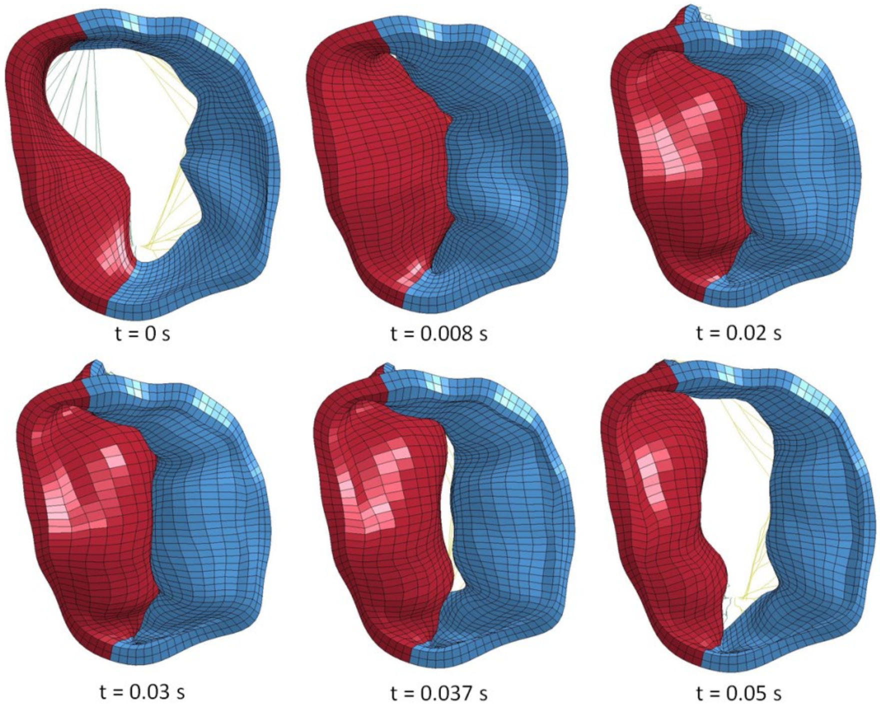

Figure C.3: Top view (from the left atrium) showing the behaviour of the healthy mitral valve model, MV4, at specific points of interest.

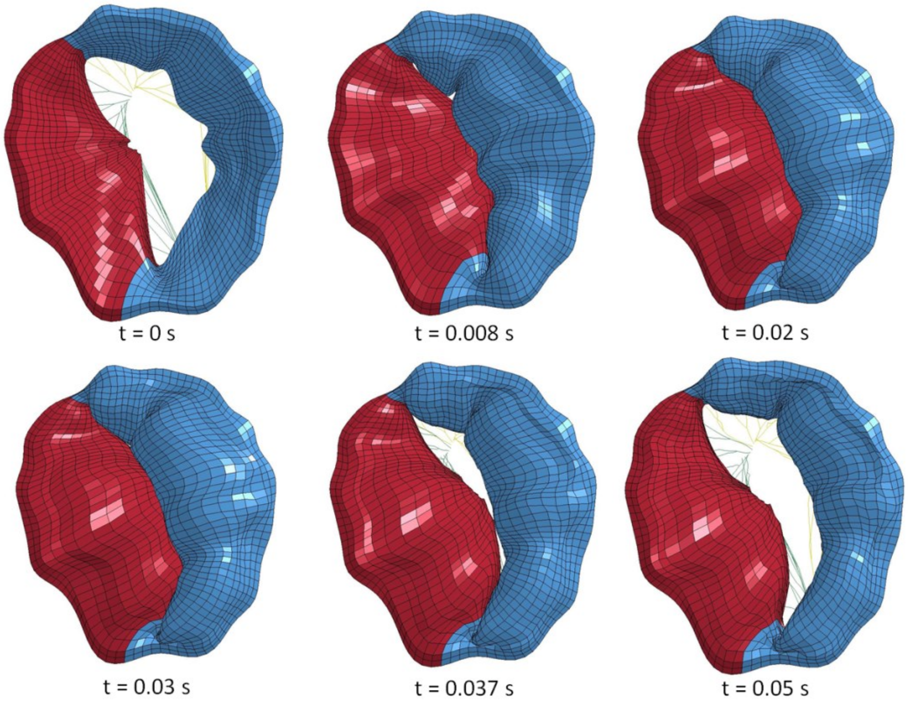

Figure C.4: Top view (from the left atrium) showing the behaviour of the healthy mitral valve model, MV7, at specific points of interest.

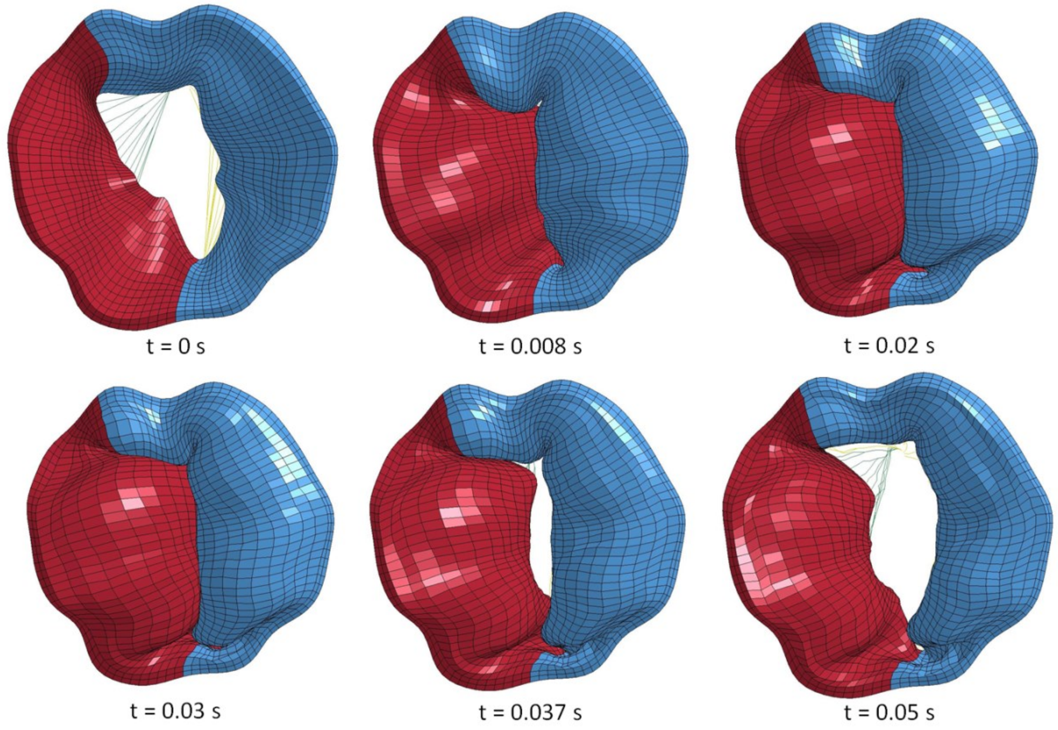
t = 0 s
t = 0.008 s
t = 0.02 s
t = 0.03 s
t = 0.037 s
t = 0.05 s

Figure C.5: Top view (from the left atrium) showing the behaviour of the healthy mitral valve model, MV8, at specific points of interest.

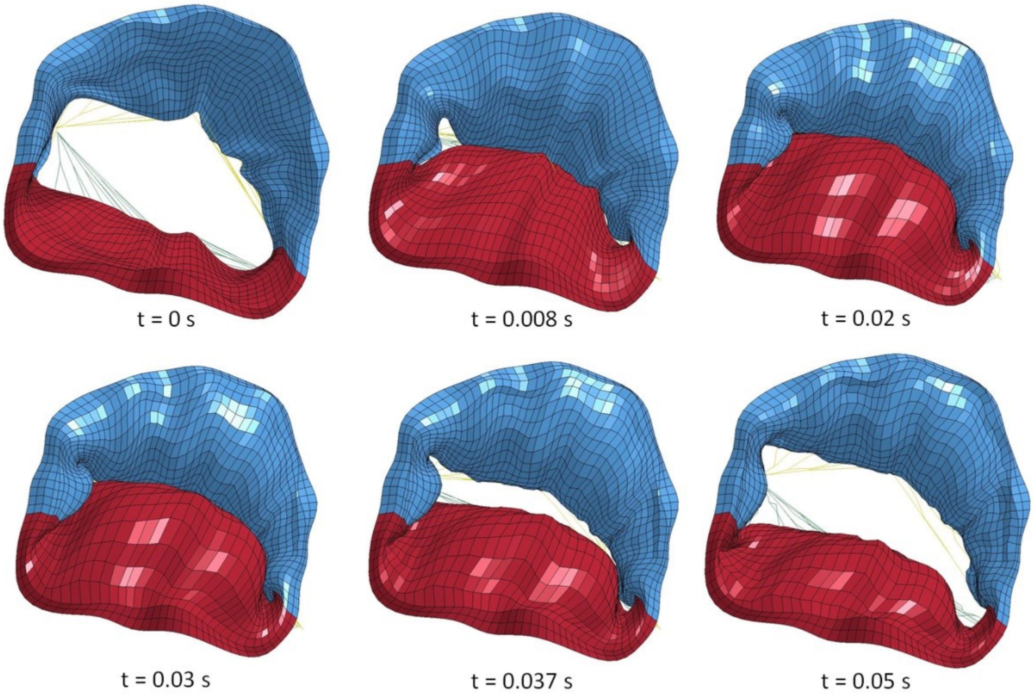
t = 0 s
t = 0.008 s
t = 0.02 s
t = 0.03 s
t = 0.037 s
t = 0.05 s

Figure C.6: Top view (from the left atrium) showing the behaviour of the healthy mitral valve model, MV9, at specific points of interest.

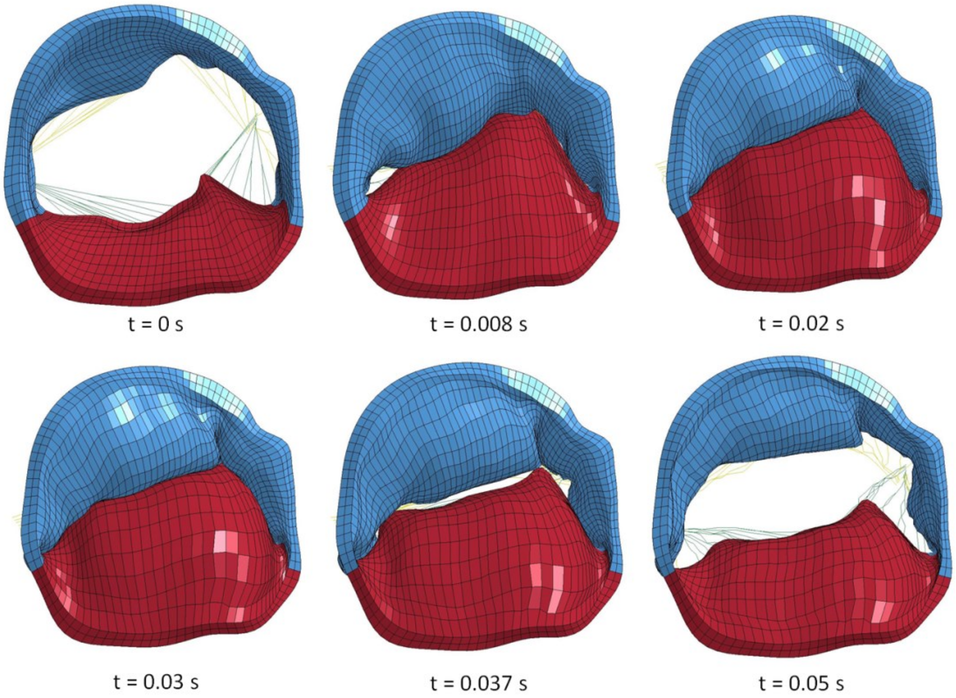

Figure C.7: Top view (from the left atrium) showing the behaviour of the healthy mitral valve model, MV12, at specific points of interest.

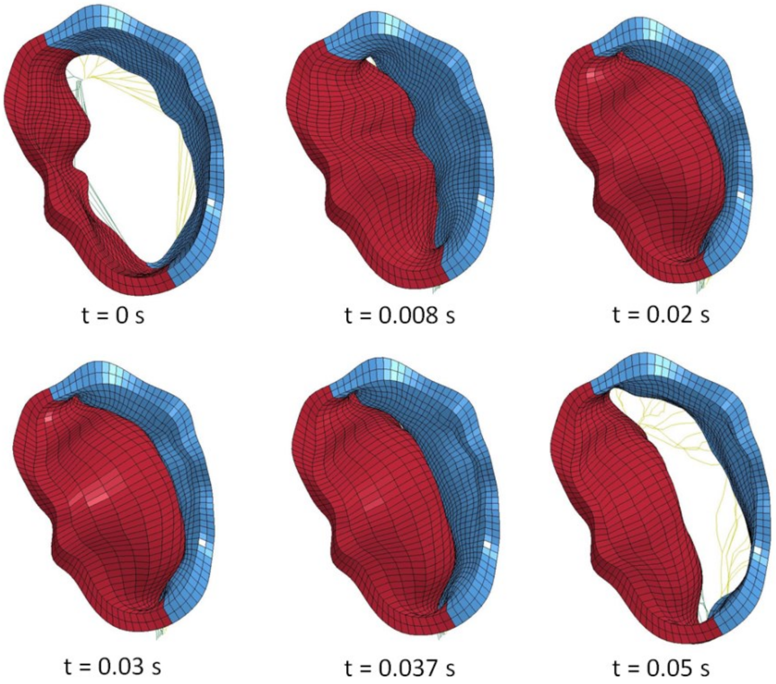

Figure C.8: Top view (from the left atrium) showing the behaviour of the healthy mitral valve model, MV13, at specific points of interest.

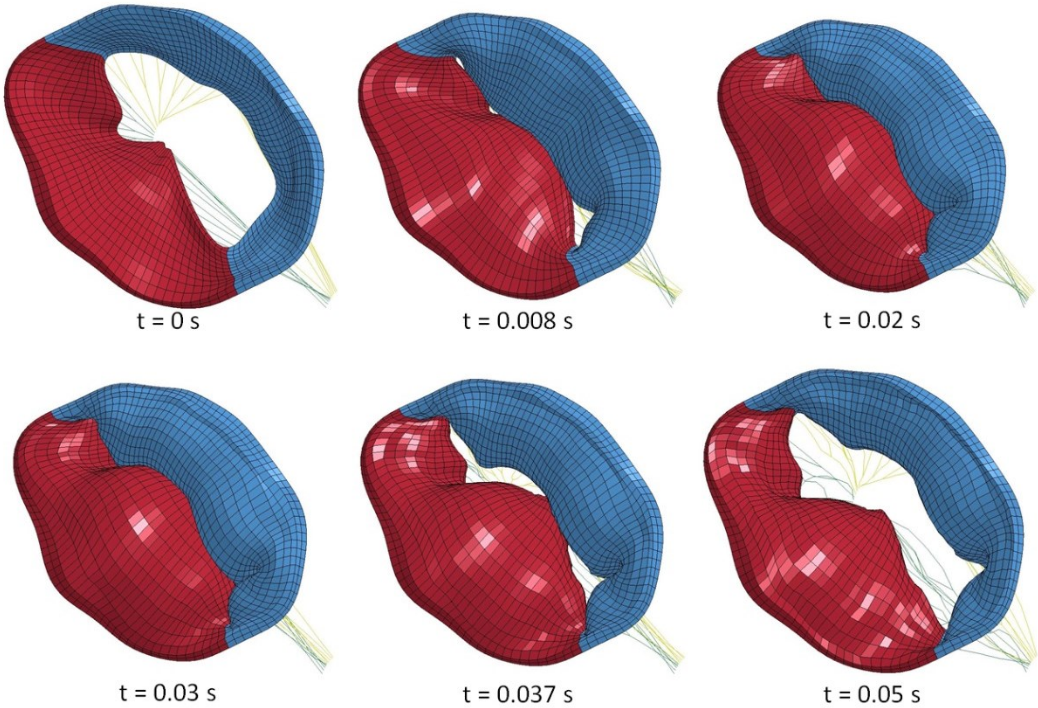

Figure C.9: Top view (from the left atrium) showing the behaviour of the healthy mitral valve model, MV14, at specific points of interest.

C.2. von Mises Stress Contour Plots

To improve contrast and continuity between models, a maximum von Mises stress of 0.5 MPa (depicted in red) was selected for all mitral valve models. Locations where the von Mises stress exceeds 0.5 MPa are depicted in gray.

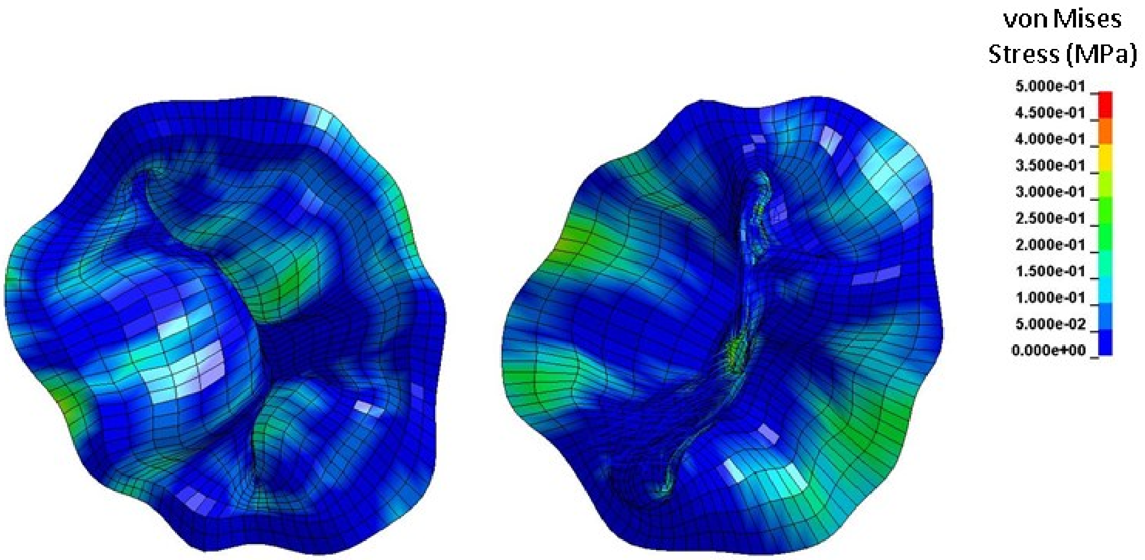

Figure C.10: von Mises stress contour plot of the healthy mitral valve dataset MV1 viewed from the atrial (left) and ventricular (right) sides.

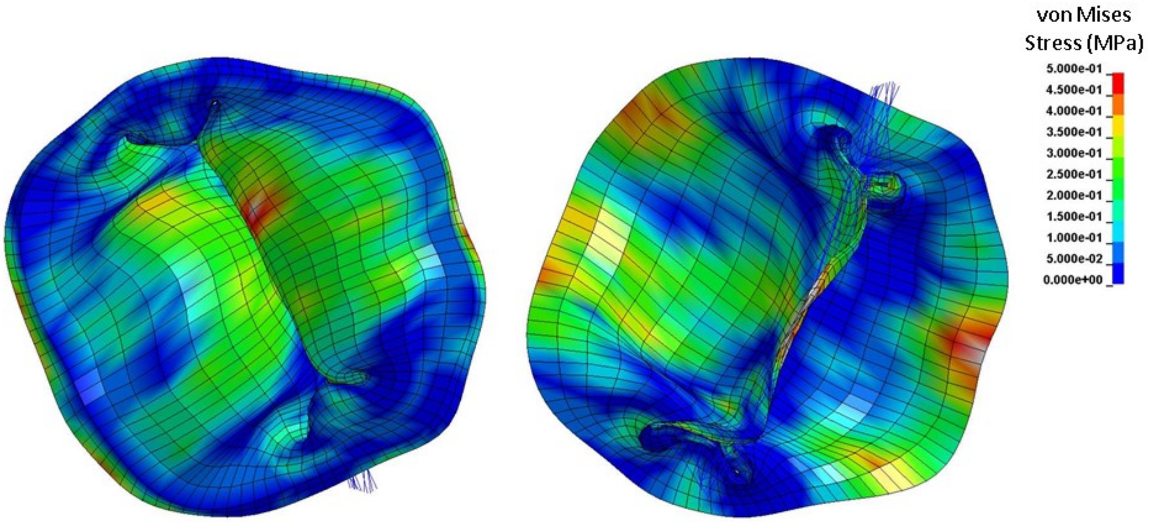

Figure C.11: von Mises stress contour plot of the healthy mitral valve dataset MV3 viewed from the atrial (left) and ventricular (right) sides.

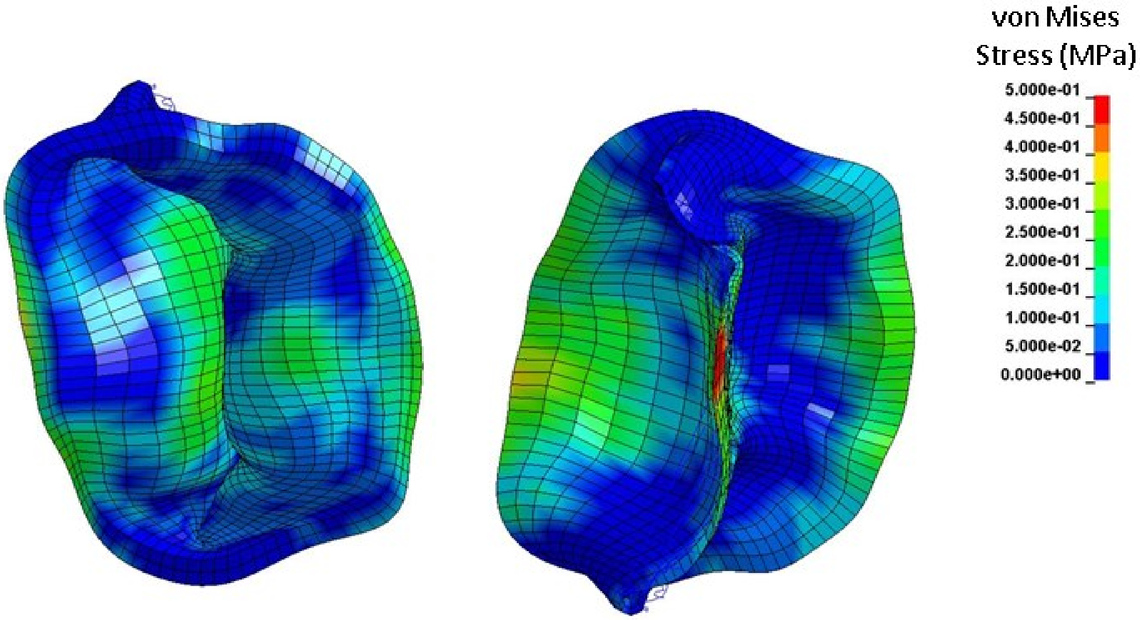

Figure C.12: von Mises stress contour plot of the healthy mitral valve dataset MV4 viewed from the atrial (left) and ventricular (right) sides.

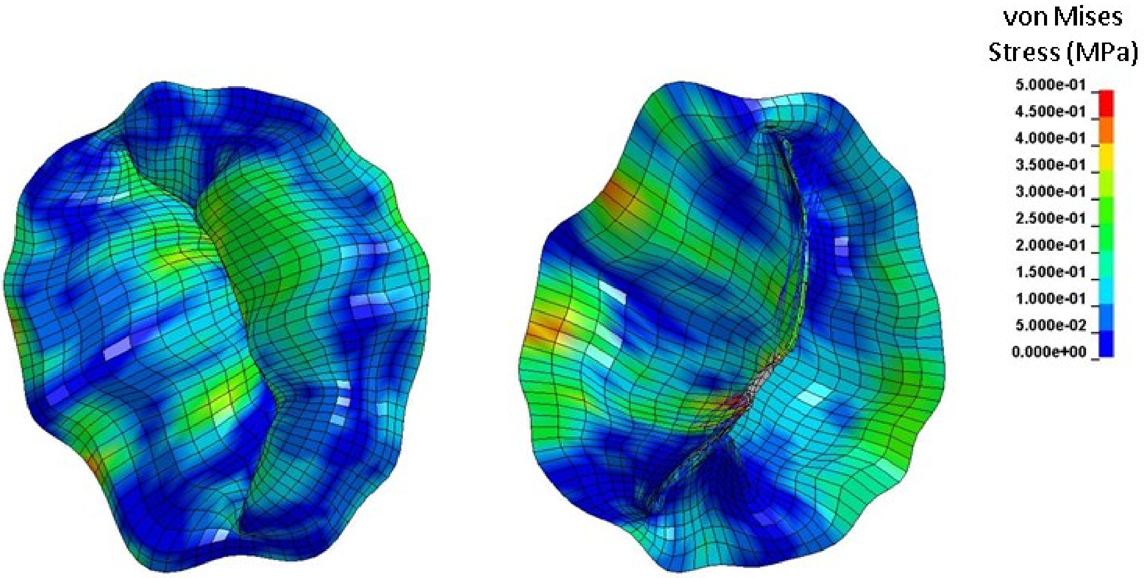

Figure C.13: von Mises stress contour plot of the healthy mitral valve dataset MV7 viewed from the atrial (left) and ventricular (right) sides.

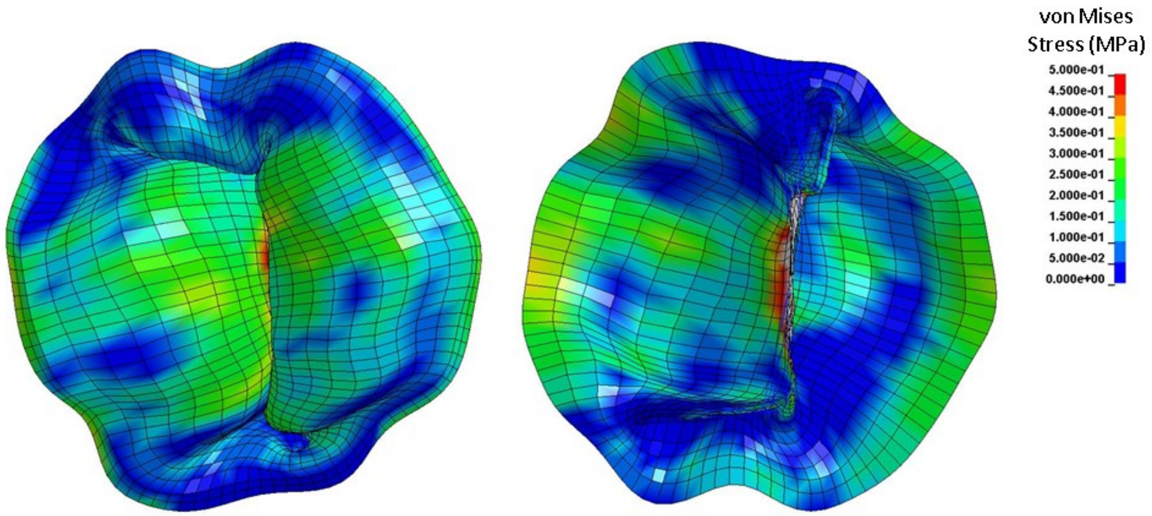

Figure C.14: von Mises stress contour plot of the healthy mitral valve dataset MV8 viewed from the atrial (left) and ventricular (right) sides.

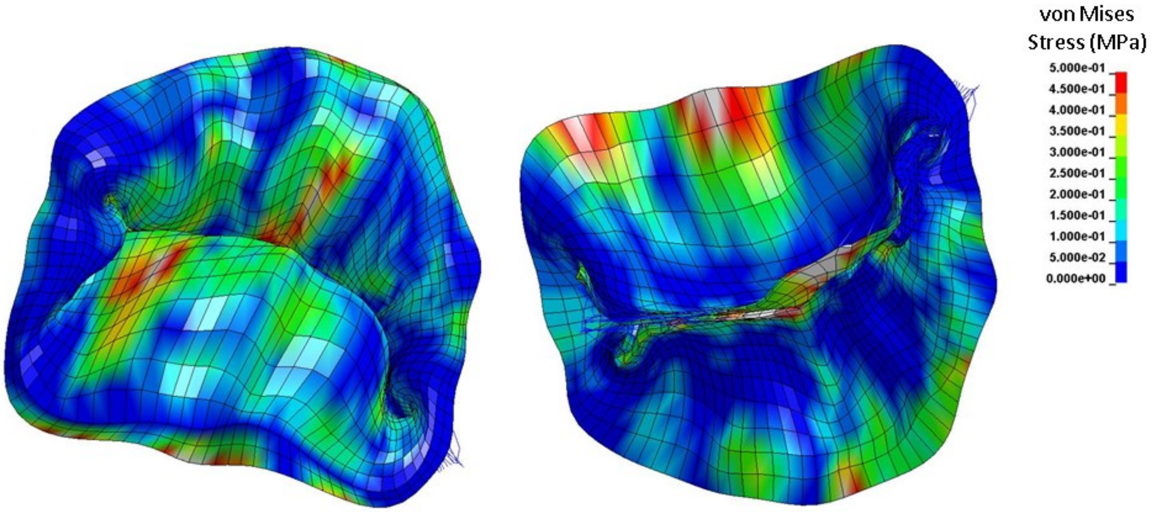

Figure C.15: von Mises stress contour plot of the healthy mitral valve dataset MV9 viewed from the atrial (left) and ventricular (right) sides.

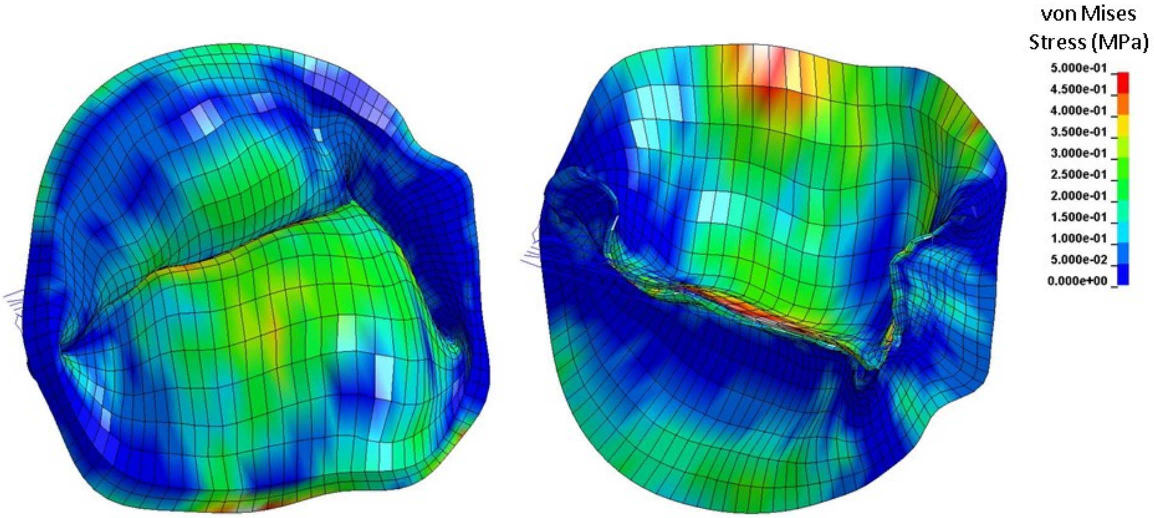

Figure C.16: von Mises stress contour plot of the healthy mitral valve dataset MV12 viewed from the atrial (left) and ventricular (right) sides.

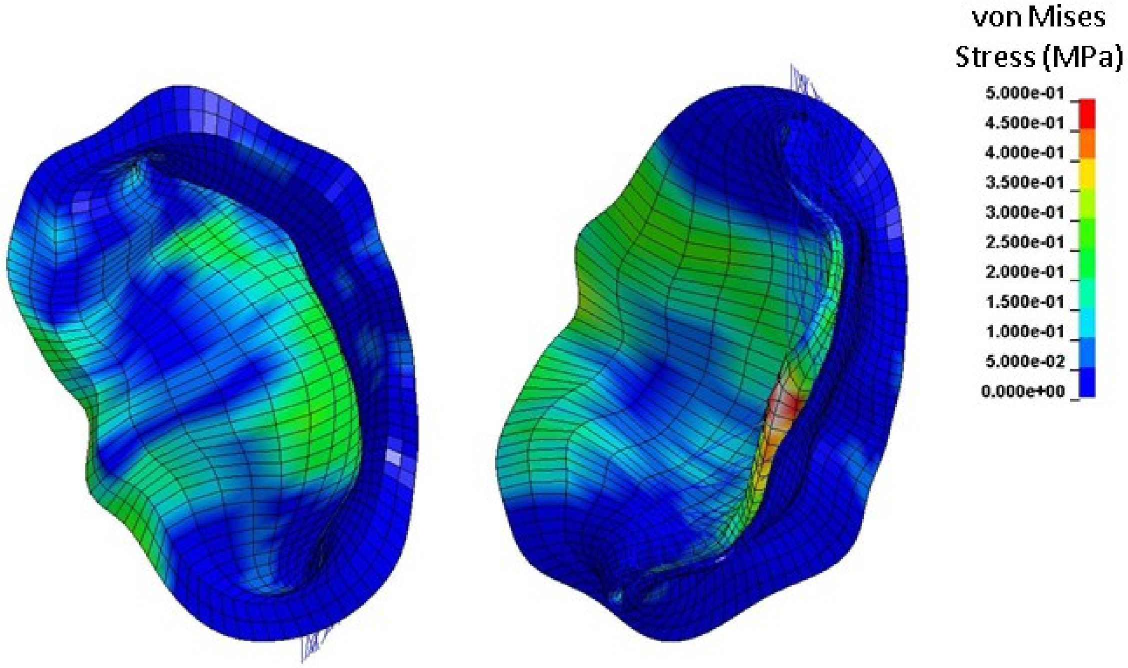

Figure C.17: von Mises stress contour plot of the healthy mitral valve dataset MV13 viewed from the atrial (left) and ventricular (right) sides.

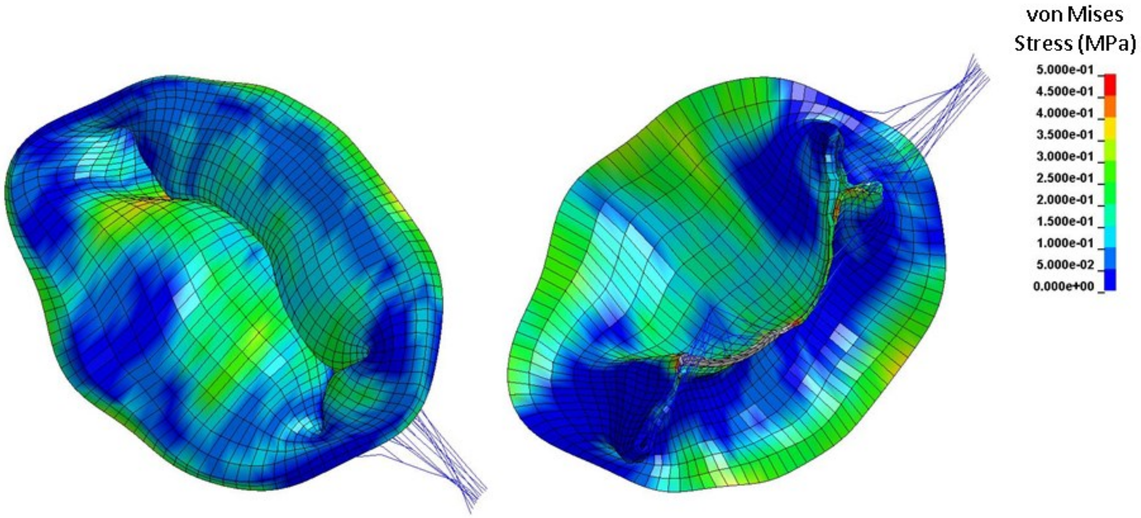

Figure C.18: von Mises stress contour plot of the healthy mitral valve dataset MV14 viewed from the atrial (left) and ventricular (right) sides.

C.3. Chordae Tendineae Forces

Table 6: Mean chordae tendineae forces

Mitral Model		**Time (s)**										
		0	**0.005**	**0.01**	**0.015**	**0.02**	**0.025**	**0.03**	**0.035**	**0.04**	**0.045**	**0.05**
Mean Axial Force (N)	MV1	0	0.011	0.026	0.038	0.055	0.062	0.071	0.033	0.001	0.002	0.002
	MV3	0	0.019	0.203	0.211	0.244	0.242	0.243	0.104	0.002	0.004	0.004
	MV4	0	0.010	0.113	0.145	0.172	0.176	0.174	0.089	0.003	0.003	0.003
	MV7	0	0.024	0.207	0.242	0.277	0.271	0.269	0.103	0.003	0.004	0.004
	MV8	0	0.015	0.164	0.186	0.210	0.210	0.205	0.084	0.005	0.005	0.004
	MV9	0	0.015	0.135	0.150	0.191	0.196	0.197	0.093	0.012	0.012	0.013
	MV12	0	0.008	0.172	0.194	0.228	0.230	0.233	0.110	0.004	0.003	0.004
	MV13	0	0.009	0.135	0.128	0.139	0.142	0.145	0.067	0.007	0.007	0.007
	MV14	0	0.016	0.114	0.119	0.135	0.135	0.134	0.059	0.003	0.003	0.004
	Mean	0	0.014	0.141	0.157	0.183	0.185	0.186	0.083	0.005	0.005	0.005
	SD	0	0.005	0.052	0.057	0.063	0.061	0.058	0.024	0.003	0.003	0.003
	Max	0	0.024	0.207	0.242	0.277	0.271	0.269	0.110	0.012	0.012	0.013
	Min	0	0.008	0.026	0.038	0.055	0.062	0.071	0.033	0.001	0.002	0.002

Table 7: Maximum chordae tendineae forces.

Mitral Model		Time (s)										
		0	**0.005**	**0.01**	**0.015**	**0.02**	**0.025**	**0.03**	**0.035**	**0.04**	**0.045**	**0.05**
Maximum Axial Force (N)	MV1	0	0.067	0.176	0.249	0.330	0.320	0.316	0.144	0.011	0.012	0.009
	MV3	0	0.098	1.342	1.211	1.258	1.243	1.198	0.603	0.019	0.020	0.023
	MV4	0	0.072	0.794	0.798	0.816	0.725	0.686	0.392	0.020	0.021	0.016
	MV7	0	0.117	0.959	1.204	1.314	1.166	1.061	0.410	0.029	0.032	0.039
	MV8	0	0.125	0.854	0.982	1.060	1.046	1.019	0.435	0.055	0.059	0.049
	MV9	0	0.066	1.027	1.279	1.415	1.320	1.212	0.530	0.064	0.070	0.054
	MV12	0	0.128	1.154	1.123	1.116	1.136	1.104	0.463	0.028	0.020	0.018
	MV13	0	0.085	1.414	1.417	1.445	1.439	1.339	0.571	0.062	0.047	0.060
	MV14	0	0.080	0.495	0.521	0.539	0.579	0.593	0.367	0.038	0.048	0.048
	Mean	0	0.093	0.913	0.976	1.033	0.997	0.947	0.435	0.036	0.037	0.035
	SD	0	0.023	0.372	0.362	0.371	0.352	0.320	0.129	0.019	0.019	0.018
	Max	0	0.128	1.414	1.417	1.445	1.439	1.339	0.603	0.064	0.070	0.060
	Min	0	0.066	0.176	0.249	0.330	0.320	0.316	0.144	0.011	0.012	0.009

C.4. Leaflet Bulging and Leaflet Angles Data

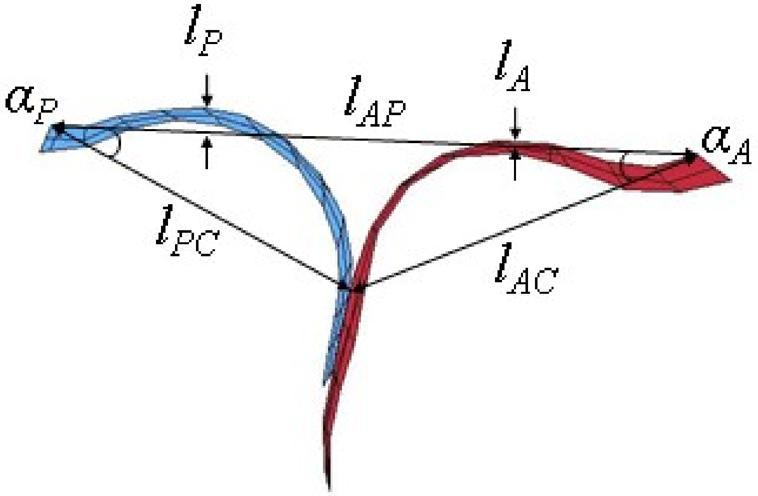

Figure C.19: Relevant measurements required to determine leaflet bulging (l_A and l_P) and leaflet angles (α_A and α_P).

Table 8: Leaflet bulging data.

Mitral Model	$l_{AP,LS\text{-}DYNA}$ (mm)	$l_{AP,ImageJ}$ (pixels)	$\frac{l_{AP,LS-DYNA}}{l_{AP,ImageJ}}$	l_P (pixels)	l_P (mm)	l_A (pixels)	l_A (mm)
MV1	24.817	632.723	0.039223	N/A	N/A	N/A	N/A
MV3	35.148	529.544	0.066374	19.059	1.265	4.000	0.265
MV4	28.936	711.254	0.040683	N/A	N/A	N/A	N/A
MV7	34.332	764.529	0.044906	10.022	0.450	N/A	N/A
MV8	35.017	918.323	0.038131	50.090	1.910	33.000	1.258
MV9	30.523	663.762	0.045985	14.621	0.672	N/A	N/A
MV12	34.411	747.98	0.046005	N/A	N/A	N/A	N/A
MV13	28.722	617.109	0.046543	N/A	N/A	41.767	1.944
MV14	24.622	594.757	0.041398	N/A	N/A	N/A	N/A

Table 9: Leaflet angles data.

Mitral Model	l_{AP} (pixels)	l_{AC} (pixels)	l_{PC} (pixels)	α_A (degrees)	α_P (degrees)
MV1	632.723	453.382	318.083	28.39	42.67
MV3	529.544	305.569	278.572	23.76	26.23
MV4	711.254	428.969	403.110	30.20	32.36
MV7	764.529	491.261	387.238	25.87	33.61
MV8	918.323	580.451	456.075	24.22	31.48
MV9	663.762	454.821	313.391	24.54	37.07
MV12	747.98	508.368	351.811	24.11	36.18
MV13	617.109	610.300	99.206	9.25	81.45
MV14	594.757	421.979	286.447	26.36	40.85

Appendix D: Ethics Approval

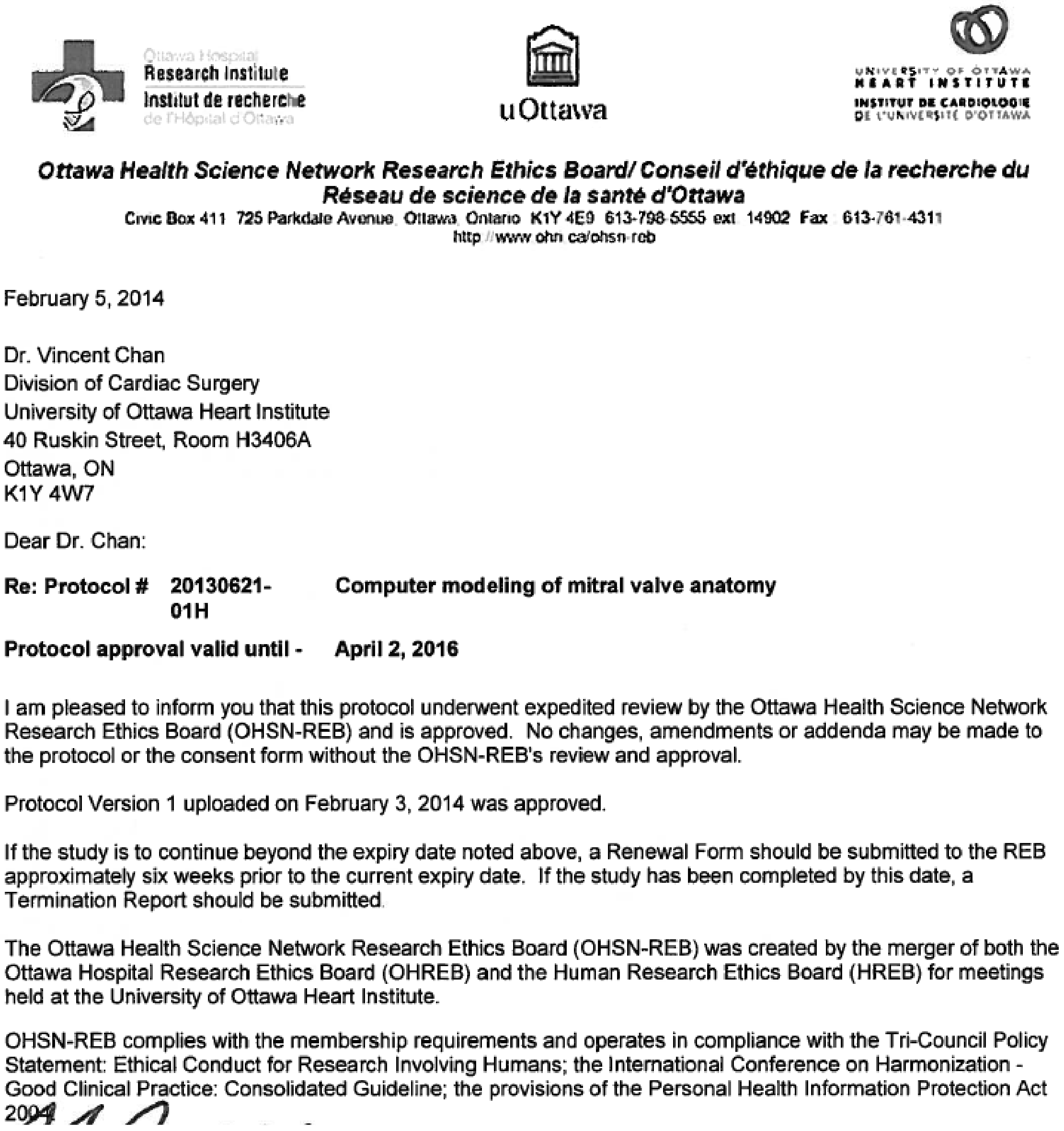

Ottawa Hospital
Research Institute
Institut de recherche
de l'Hôpital d'Ottawa

uOttawa

University of Ottawa
Heart Institute
Institut de cardiologie
de l'Université d'Ottawa

Ottawa Health Science Network Research Ethics Board/ Conseil d'éthique de la recherche du Réseau de science de la santé d'Ottawa
Civic Box 411 725 Parkdale Avenue, Ottawa, Ontario K1Y 4E9 613-798-5555 ext 14902 **Fax** 613-761-4311
http://www.ohri.ca/ohsn-reb

February 5, 2014

Dr. Vincent Chan
Division of Cardiac Surgery
University of Ottawa Heart Institute
40 Ruskin Street, Room H3406A
Ottawa, ON
K1Y 4W7

Dear Dr. Chan:

Re: Protocol # 20130621-01H Computer modeling of mitral valve anatomy

Protocol approval valid until - April 2, 2016

I am pleased to inform you that this protocol underwent expedited review by the Ottawa Health Science Network Research Ethics Board (OHSN-REB) and is approved. No changes, amendments or addenda may be made to the protocol or the consent form without the OHSN-REB's review and approval.

Protocol Version 1 uploaded on February 3, 2014 was approved.

If the study is to continue beyond the expiry date noted above, a Renewal Form should be submitted to the REB approximately six weeks prior to the current expiry date. If the study has been completed by this date, a Termination Report should be submitted.

The Ottawa Health Science Network Research Ethics Board (OHSN-REB) was created by the merger of both the Ottawa Hospital Research Ethics Board (OHREB) and the Human Research Ethics Board (HREB) for meetings held at the University of Ottawa Heart Institute.

OHSN-REB complies with the membership requirements and operates in compliance with the Tri-Council Policy Statement: Ethical Conduct for Research Involving Humans; the International Conference on Harmonization - Good Clinical Practice: Consolidated Guideline; the provisions of the Personal Health Information Protection Act 2004